LONDON'S GLOBAL UNIVERSITY

Guided wave propagation and scattering in anisotropic composite structures

Flora Louise Hervin

Department of Mechanical Engineering

University College London (UCL)

A thesis submitted for the degree of

Doctor of Philosophy

February 2023

Declaration

‘I, Flora Hervin confirm that the work presented in this thesis is my own. Where information has been derived from other sources, I confirm that this has been indicated in the thesis.'

Flora Hervin

February 2023

Abstract

Carbon fibre reinforced polymer (CFRP) laminates are widely used for aerospace applications as they reduce the weight of structures whilst maintaining mechanical strength. Composites have highly anisotropic material properties and high in-plane strength but poor interlaminar strength, making them vulnerable to barely visible impact damage (BVID) caused by low velocity impacts. Composite damage is multi-modal, consisting of fibre breakage, matrix cracking, and delaminations, with delaminations causing the most significant strength reduction. Guided ultrasonic waves, often generated using a sparse network of sensors bonded to a structure, provide a promising structural health monitoring (SHM) technique for composites. Guided waves propagate along a structure, with energy throughout the entire thickness, making them ideal for rapid, long-range inspection of large areas. In anisotropic materials wave energy is focused along the high stiffness (fibre) directions, resulting in higher amplitude and wave speed in these directions. Waves launched away from the fibre direction are steered towards the fibres. These anisotropic effects could lead to inaccuracies in damage localization if not accounted for.

Propagation of the fundamental, flexural (A_0) guided wave mode was investigated in an undamaged unidirectional CFRP panel. Anisotropic effects including the directionality of wave velocities, skew angles, and beam spreading were quantified through both finite element simulations and experiments, achieving good agreement with predictions obtained from dispersion curves. Scattering of the A_0 mode at an artificial delamination was studied for a quasi-isotropic CFRP plate layup. Wave-trapping on top of the delamination, and strong forward scattering at the delamination exit was found. Significantly different scattering behaviour was observed to that of a magnet target, often used to develop SHM systems. Scattering around both damage targets was found to be directionally dependent, with higher amplitudes in the fibre directions of the outermost laminae. Implications for the SHM of composites were discussed.

Impact Statement

This thesis investigates the influence of material anisotropy on the propagation and scattering of ultrasonic guided waves at damage in carbon fibre reinforced polymer (CFRP) laminates. CFRP laminates, consisting of highly anisotropic fibre-matrix ply layers, are strong but lightweight materials making them ideally suited to aerospace applications such as aircraft fuselage, wing spars, and stiffeners. Composite laminates are prone to damage from low velocity impacts such as a bird strike or dropped tools. This results in subsurface damage consisting of delaminations (separation of ply layers), matrix cracking, and fibre breakage that cannot be detected from visual inspection and can significantly reduce the structural integrity of aircraft components. Therefore, rapid and reliable non-destructive evaluation (NDE) and structural health monitoring (SHM) techniques are required to accurately locate and characterize the extent of damage. Accurate damage detection leads to improved safety of aircraft components and allows for thinner and lighter parts containing less material to be manufactured and operated safely. This will result in lower fuel consumption by reducing aircraft weight, and less material being required, contributing towards the government net zero and decarbonization strategies.

Ultrasonic guided waves are particularly advantageous for SHM of aircraft structures as they can be generated at a single location and propagate over large areas, with wave energy distributed through the full thickness of the part. This allows for the inspection of inaccessible regions of a structure and in-situ testing using permanently installed lightweight sensors. Sparse networks of sensors can be used to map damage locations in composite structures. However, imaging algorithms used to reconstruct acquired signals require prior knowledge of the scattering behaviour at a particular damage type. Guided waves are influenced by the material properties and anisotropy of a structure. In fibre reinforced laminates wave energy tends to be focused towards the high stiffness fibre directions, resulting in directional dependency of velocity and the guided wave pulse being steered away from the original launching direction. If unaccounted for, this will reduce the accuracy of damage detection and localization. Anisotropic wave propagation effects, coupled with the complex damage mechanisms in composite laminates means that guided wave

interaction with damage in CFRP is not fully understood. This study aims to improve the understanding of the guided wave propagation and scattering effects at damage in anisotropic composites, which will contribute to better damage detection localization and characterisation in composite aircraft structures. Composite aircraft structures are currently built with additional material as a safety margin. By improving damage detection, the probability of detection (POD) can be increased, which could allow for safe reduction of these safety margins enabling the advantages of CFRP to be fully exploited for lightweight aerospace design which will lead to reduced fuel consumption over the aircraft lifetime.

List of Publications

Journal Articles – First Author

F. Hervin, L. Maio, P. Fromme, “Guided wave scattering at a delamination in a quasi-isotropic composite laminate: Experiment and simulation”. Composite Structures, Volume 275 (2021) 114406. https://doi.org/10.1016/j.compstruct.2021.114406

F. Hervin, P. Fromme, “Anisotropy influence on guided wave scattering for composite structure monitoring”, Structural Health Monitoring. (Available Online 2022). https://doi.org/10.1177/14759217221133284

F. Hervin, P. Fromme, “Guided wave propagation and skew effects in anisotropic CFRP laminates”. Journal of the Acoustical Society of America, Volume 153(4) (2023) 2049. https://doi.org/10.1121/10.0017784

F. Hervin, P. Fromme, “Guided wave skew velocity correction in anisotropic laminates”. Ultrasonics, Volume 133, 107047. https://doi.org/10.1016/j.ultras.2023.107047

Oral Presentations at Conferences – First Author

F. Hervin, P. Fromme, “Guided wave propagation and scattering at composite delaminations”. Health monitoring of structural and biological systems XV, SPIE Smart Structures and NDE 2021 (Online).

F. Hervin, P. Fromme, “Modelling Anisotropy Influence on Guided Wave Scattering at Composite Delaminations”, 48th Annual Review of Progress in Quantitative Nondestructive Evaluation 2021, (Online)

F. Hervin, P. Fromme, “Effect of material Anisotropy on guided wave propagation and scattering in CFRP laminates”. Health monitoring of structural and biological systems XVI, SPIE Smart Structures and NDE 2022, Long Beach, California (USA).

F. Hervin, P. Fromme, “Directionally Dependent Guided Wave Scattering for the Monitoring of Anisotropic Composite Structures”, 49th Annual Review of Progress in Quantitative Nondestructive Evaluation 2022, San Diego, California (USA).

F. Hervin, P. Fromme, “Anisotropy influence on guided wave propagation and steering in unidirectional CFRP”, 49th Annual Review of Progress in Quantitative Nondestructive Evaluation 2022, San Diego, California (USA).

Conference Proceedings

L. Maio, F. Hervin, P. Fromme, “Guided wave scattering analysis around a circular delamination in a quasi-isotropic fiber-composite laminate”. Proc SPIE 113810Q (2020). https://doi.org/10.1117/12.2559125

F. Hervin, P. Fromme, Guided wave propagation and scattering at composite delaminations, Proc SPIE 115930Q (2021). https://doi.org/10.1117/12.2582363

F. Hervin, P. Fromme Modelling Anisotropy Influence on Guided Wave Scattering at Composite Delaminations, Proceedings of the ASME 2021, 48th Annual Review of Progress in Quantitative Nondestructive Evaluation (2021) https://doi.org/10.1115/QNDE2021-74591

F. Hervin, P. Fromme, Effect of material Anisotropy on guided wave propagation and scattering in CFRP laminates, Proc SPIE 120480G (2022) https://doi.org/10.1117/12.2612788

F. Hervin, P. Fromme, Directionally Dependent Guided Wave Scattering for the Monitoring of Anisotropic Composite Structures, Proceedings of the ASME 2022, 49th Annual Review of Progress in Quantitative Nondestructive Evaluation (2023) https://doi.org/10.1115/QNDE2022-98367

F. Hervin, P. Fromme, Anisotropy influence on guided wave propagation and steering in unidirectional CFRP, Proceedings of the ASME 2022, 49th Annual Review of Progress in Quantitative Nondestructive Evaluation (2023) https://doi.org/10.1115/QNDE2022-98375

F. Hervin, P. Fromme, Guided wave energy focusing and steering in composite laminates, Proc SPIE 1248804 (2023) https://doi.org/10.1117/12.2657435

Acknowledgements

First and foremost, I would like to express my deepest gratitude to my supervisor Prof. Paul Fromme for your unwavering patience, support and kindness on both academic and personal matters. Thanks for allowing space for all of the ‘stupid questions’, for knowing just how to build my confidence, and for believing I could do it when I wasn’t really sure myself. Above all thank you for your knowledge and mentorship and being an excellent person to talk about guided waves with.

I’d also like to extend my sincerest thanks to Prof. Nader Saffari for his advice, encouragement and support throughout my time at UCL. Many thanks to Dr. Leandro Maio at the University of Naples for loaning the composite specimen.

A PhD is not possible without the support from family and friends, and it is impossible to thank each and every one of you here individually. Thank you to my family for your support throughout my studies. Special mentions go to my colleagues Enze, Erin and Fred for all of the conversations over coffee. To my dear friends Hannah, James, Emma and Tim for sticking with me even when I went quiet for a while, and for reminding me what the real world looks like. To Rupert the cat for interrupting almost every online meeting and my flatmate Daniel for doing the exact opposite.

Finally, this thesis would not have been possible without the love and support from my fiancée, Emily. Thank you for your faith in me every step of the way, this would not have been possible without you by my side.

Table of Contents

Table of Figures

Nomenclature

A	Anisotropy factor
A_0	Fundamental antisymmetric guided wave mode
a_n	Amplitude coefficient for Gaussian function
b_n	Peak centroid of Gaussian function
C	Damping matrix
C_{ij}	Complex stiffness coefficient
c_{av}	Averaged peak width coefficient of Gaussian function
c_g	Group velocity
c_{max}	Maximum wave speed
c_n	Peak width coefficient of Gaussian function
c_p	Phase velocity
D	Divergence
d	Propagation distance
E_i	Young's modulus
f	Frequency
$\hat{f}$	Force
G_{ij}	Shear modulus
K	Stiffness matrix
l_{min}	Shortest element length
N_{cyc}	Number of cycles
R^2	Coefficient of determination
S_0	Fundamental symmetric guided wave mode
SH_0	Fundamental shear horizontal guided wave mode
T_{MAX}	Time of maximum Hilbert ampltiude
t	Time
Δt_c	Critical time increment
Δt_{inc}	Time increment
u	Displacement
$\dot{u}$	Velocity
$\ddot{u}$	Acceleration
U	Wave amplitude
U_0	Initial wave amplitude

U_b	Wave amplitude from baseline simulation
U_d	Wave amplitude from damage simulation
U_i	Incident wave amplitude
U_s	Scattered wave amplitude
Δx	Distance between measurement points (horizontal)
Δy	Distance between measurement points (vertical)
α	Mass proportional Rayleigh damping coefficient
β	Stiffness proportional Rayleigh damping coefficient
η	Attenuation coefficient
θ_{group}	Group direction
θ_{phase}	Phase direction
θ_{skew}	Wave skew angle
λ	Wavelength
ν_{ij}	Poisson ratio
ρ	Density
ϕ	Phase angle

Abbreviations

ABT	Angle beam transducer
BVID	Barely visible impact damage
CFRP	Carbon fibre reinforced polymer
EFIT	Elastodynamic finite integration technique
EMAT	Electromagnetic acoustic transducer
FE	Finite element
FEA	Finite element analysis
FEM	Finite element modelling
LDV	Laser Doppler vibrometer
NDE	Non-destructive evaluation
PZT	Lead zirconate titanate
SAFE	Semi analytical finite element
SHM	Structural health monitoring

1 Introduction

Carbon fibre reinforced polymer (CFRP) composite laminates are often selected for aerospace applications as they are lightweight but have good mechanical strength compared to their metallic counterparts. They consist of ply layers, or laminae, with stiff fibres set into a polymer matrix, resulting in highly anisotropic material properties. Whilst composites have high in-plane strength due to the high stiffness fibres, they have poor interlaminar strength leaving laminates vulnerable to damage from low velocity impacts. Such impacts can produce barely visible subsurface damage, consisting of fibre breakage, matrix cracks, and delaminations, dramatically reducing the strength of the laminate. Subsequent application of loads can cause damage to further propagate, potentially resulting in catastrophic component failure. Therefore, accurate and reliable non-destructive evaluation (NDE) and structural health monitoring (SHM) techniques are required to locate and characterise damage and improve the safety of aircraft components.

Ultrasonic guided waves provide a promising in-situ SHM solution for composites as they can be generated at a single location of a structure but propagate over large areas with relatively low attenuation. This allows for large areas to be rapidly monitored, and inaccessible regions of a structure to be inspected. A number of wave modes can be supported by a structure; however, it is generally desirable to generate a single wave mode to simplify signal processing. The fundamental antisymmetric A_0 Lamb wave mode is a flexural (bending) mode and is often selected for the monitoring of composites as reflections occur from delaminations at all depths. Due to the high anisotropy of composite laminates a number of anisotropic wave propagation effects can occur. Wave energy tends to be focused along the high-stiffness fibre directions resulting in directionally dependent wave velocities and amplitudes, in addition to wave skewing (also known as beam steering) and beam spreading effects. If left unaccounted for, anisotropic wave propagation effects could reduce the accuracy of damage detection. By fully understanding guided wave interaction with damage in anisotropic composites, the accuracy of SHM techniques can be improved.

The outline of this thesis is as follows: Chapter 2 presents an overview of the relevant literature. Properties of composite materials and their damage mechanisms are introduced before outlining a range of NDE and SHM techniques used for composites. Ultrasonic guided waves are introduced, guided wave dispersion and choice of wave mode are discussed, and specific wave propagation effects due to anisotropy of composites are described. Guided wave interaction with various damage types in composite laminates is discussed, in addition to guided wave propagation in more complex composite structures such as T-joints and curved panels. Finally, the motivation and objectives of the PhD study are given.

Chapters 3 and 4 present general aspects of the experimental laser Doppler vibrometer (LDV) measurements and Finite Element (FE) modelling, respectively. Specific details are given at the start of the relevant results chapters. Details of composite specimens, experimental apparatus, and transducers are given in Chapter 3. Details of the FE model generation, stability criteria, and the procedure for modelling damage is described in Chapter 4.

Guided wave propagation in an undamaged unidirectional composite plate is described in Chapter 5. Guided wave velocities in different wave launching directions are investigated for point and line sources of various lengths through FE modelling. Models are validated by velocity measurements from a disc (point) transducer and compared to theoretical values from dispersion curves. Wave skewing behaviour is visualised through modelled wavefields and a line transducer is developed to validate the models experimentally. Simulated and measured wave skew angles are calculated and compared with theoretical results obtained from the phase slowness curve. An estimation of the beam spreading is obtained from the propagating wavefields and is compared with theoretical predictions. The influence of these anisotropic wave propagation effects on guided wave based SHM is discussed.

Building on the guided wave propagation studied in Chapter 5, Chapter 6 investigates the scattering of guided waves at damage, specifically a circular insert delamination in a quasi-isotropic laminate. Experimental wavefield measurements of guided wave interaction on top of the delamination and the

undamaged regions surrounding it are compared with FE models. Parameter studies of delamination size shape and depth are then performed numerically, the results of which are presented in Chapter 7. Guided wave scattering at a delamination is compared with that of a permanent magnet, which are often used to simulate damage experimentally. The influence of anisotropy on the scattering of the A_0 mode at both a delamination and a magnet target is investigated by varying the incident wave launching direction. The 2D scattering matrices are calculated for each damage type in order to describe the full scattering characteristics of each damage. Implications for structural health monitoring, in particular sparse array imaging, are discussed.

A summary of the results presented in this thesis is given in Chapter 8. Conclusions are drawn and recommendations for future research on this topic are stated.

2 Literature review

This chapter presents an overview of the relevant literature for this PhD study. Properties and damage mechanisms of composite laminates are introduced before the various non-destructive evaluation (NDE) and structural health monitoring (SHM) techniques suitable for inspecting composites are discussed. Ultrasonic guided waves are introduced, along with the wave propagation effects that occur in anisotropic materials such as composites. Details of guided wave interaction with impact damage, delaminations, and simulated damage targets are discussed. Guided wave propagation in complex composite structures is introduced. Implications for the SHM of composites are presented throughout. The motivation and aims and objectives for this study are discussed in section 2.4.

2.1 Composite Laminates

2.1.1 Properties of Composite Laminates

Composite materials are increasingly being used in aerospace applications due to their good strength to weight ratio [1]. Their material properties are highly anisotropic, which can be advantageous as these properties can be tailored in the directions where high structural loads are expected. Composites have low thermal conductivity [2] and are also resistant to corrosion, which makes them well suited to applications in harsh environments such as aircraft components or wind turbine blades [3]. Composite laminates consist of carbon or glass fibres set into a polymer matrix such as epoxy resin. The fibres are approximately a few micrometres in diameter and generally occupy 30-70% of the matrix volume [4]. A pre-preg composite laminate has numerous fibre-matrix layers called plies that are typically around 0.2mm in thickness. The pattern of fibre orientation between plies is called the lay-up or fibre stacking sequence. The strength and impact resistance of a composite laminate is highly dependent on the layup [5]. A unidirectional laminate has plies with fibres oriented in a single direction and has poor resistance to impact damage. A cross-ply laminate has plies with fibres oriented in the 0° and 90° directions, whereas quasi-isotropic laminates can have plies oriented at 0°, 90°, 45°, and −45° relative to the 0° direction. The

stacking sequence can be described using shorthand notation. For example, the notation $[0/45/-45/90]_s$ describes an 8-ply quasi-isotropic laminate that is symmetric about the mid-plane.

2.1.2 Damage in Composite Laminates

The complex structure of composite materials means that their fatigue and fracture are very different to their metallic counterparts. Damage to composites can occur during manufacturing or when in service through a variety of damage modes. Fibre breaking, matrix cracking, delamination, debonding, ply wrinkling and fibre waviness can all occur, with potentially severe effects on the integrity of the composite structure [6]. During manufacturing, uneven distribution of fibres can create resin rich pockets, which causes non-uniformity in the mechanical properties. Composites need to be heated at constant elevated temperature, or 'cured' during the manufacturing process so that the plies harden and adhere. In thicker composites it is more difficult to achieve a constant temperature, producing regions of under-cured and over-cured matrix, which in turn affects the mechanical properties. Errors in the layup such as missing plies can also affect these properties. Fibre waviness [7] and ply wrinkling [8] have been shown to significantly reduce the strength of a composite sample. Composites that have been toughened with thermoplastic particles in the resin can have improved resistance to delamination, but less so to matrix cracks, when impacted [9].

Aircraft parts in service are often subjected to low velocity impact damage caused by incidents such as a bird strike or a dropped tool. Even a small impact can cause barely visible impact damage (BVID) that extends through the thickness of the laminate, whilst the uppermost ply remains undamaged. Multilayer defects, consisting of delaminations (separation of the ply layers), fibre breakage, and matrix cracking, occur throughout the thickness of the laminate, below the visible surface. The extent of damage relates to the impact velocity and energy, the bending stiffness mismatch between adjacent ply layers due to different fibre orientations [6], as well as the thickness of the laminate [10,11]**.** In thick laminates, impact damage has been demonstrated to propagate as a cone away from the impact location creating a 'pine tree' pattern

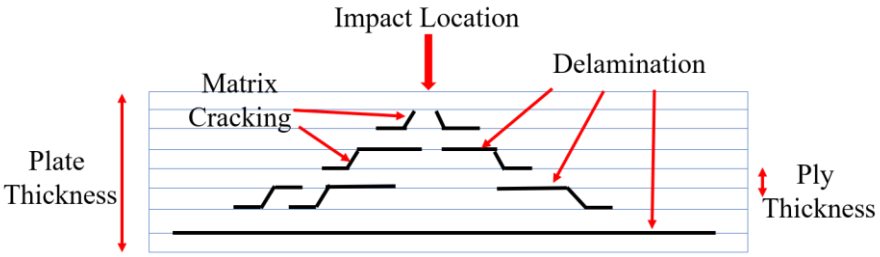

Figure 2-1 Schematic of impact damage in the cross section of a composite laminate. Adapted from [11].

[12], as shown schematically in Figure 2-1. In thin laminates, matrix cracking typically starts in the lowest ply layer due to bending stresses, and intra-ply cracks and interface delaminations propagate from the lowest surface up towards the impacted surface, resulting in a reverse pine-tree pattern [13]. A 'butterfly' pattern of (approximately) circular and ellipse shaped delaminations of varying size is often observed in the in-plane direction [14–16]. Whilst impact damage is complex and consists of multiple and interacting failure modes, delamination is considered the most dominant and critical failure mechanism in composites [17]. A relatively small impact load can cause extensive delamination damage below the laminate surface, resulting in BVID that is difficult to detect [18]. Subsequent application of external loads may induce fracture growth, leading to degradation of material properties (e.g., compressive strength reduction), and eventually catastrophic failure.

2.1.3 NDE of Composite Laminates

Reliable NDE techniques are required to ensure the safety of load bearing structures by detecting and characterising manufacturing and in-service damage. An ideal NDE technique should not only be able to locate defects, but also characterise the size, shape, and severity of damage [19]. Radiography (X-rays) and ultrasound are the most widely employed NDE techniques for composite laminates. There are, however, numerous other techniques that have been used to inspect composites [3]. Coin tapping involves tapping each point of a structure with either a coin or an instrumented hammer, providing a practical method for inspecting aircraft structures [20]. Damaged regions of the component (e.g., delaminations) sound duller than healthy regions, enabling

sufficiently large near-surface internal damage to be detected in thin structures. This technique is effective for the inspection of disbonds between the skins of honeycomb composites, however, is not recommended for laminated structures as this can cause additional damage [21]. Thermography measures infra-red radiation released by a structure under fatigue loading or from an externally applied heat source [22]. As composites have low thermal conductivity, they are well suited to thermography, however material inhomogeneity (due to the fibres) can affect the distribution of applied heat and variations in surface emissivity can reduce the accuracy of damage detection. Holography, also known as optical interferometry, involves measuring the speckle interference pattern from a monochromatic source which is affected by the surface structure and motion [23]. This technique has been demonstrated to detect surface and shallow delamination damage in CFRP, however is less suitable for detecting deeper BVID. Acoustic emission (AE) measures the acoustic waves emitted when a material undergoes irreversible changes, e.g., matrix or fibre cracking. It is suitable for in dynamic in-situ monitoring, as AE signals are produced as damage occurs [24]. Waves are emitted directly from the damage location, allowing for accurate damage localization, but damage cannot be accurately characterized from these signals. Eddy currents are magnetic fields generated in a structure through electromagnetic induction and have limited application in composites due to poor electrical conductivity of the matrix, and poor sensitivity to subsurface damage [25]. However, the carbon fibres have good electrical conductivity, and so the fibre directions and fibre waviness have been determined in CFRP using eddy currents. Electrical resistance measurements of composite plates have been shown to be sensitive to impact damage, providing a lightweight in-situ SHM technique, however, damage characterization is not possible with this method [26]. Terahertz spectroscopy involves electromagnetic radiation with frequencies of the order of 10^{12}Hz. High resolution images of fibres, voids and inclusions can be achieved in composites. However, this technique is expensive and specimen size is limited by the size of the scanner [27].

Radiography or X-rays are electromagnetic waves with frequencies of the order of 10^{16}Hz. Low energy X-rays are attenuated as they pass through a composite

sample. The extent of attenuation depends on the atomic number of the material present. Exposures are usually taken from multiple directions in order to fully characterise damage. The contrast of conventional radiography techniques is usually not sufficient to resolve individual fibres, but matrix cracks can be detected [3]. The contrast of these techniques can be improved by brushing the sample with liquid penetrant such as zinc iodide [12]. The penetrant should eventually evaporate, leaving no trace in the material, however most of these chemicals are toxic, and will only penetrate damage if it originates at the edge of a sample [3]. Planar X-ray techniques have been shown to have poor sensitivity to in-plane damage such (e.g. delamination) and so need to be used in conjunction with other methods to ensure critical damage is not missed. X-ray computed tomography (CT) can produce high resolution 3D images of porosity, cracks, and delaminations which are not visible in 2D planar images. However, X ray CT can be time consuming and requires the sample to be placed in the scanner, limiting the sample size that can be tested and its suitability for in-situ monitoring [28]. X- ray phase contrast imaging (XPCi) relies on the phase shift of the X-ray due to inhomogeneities of the specimen, resulting in high resolution and detection of small defects (~10μm) [29,30]. These high-resolution imaging methods are ideal for detailed damage and material characterisation, however they can be less suited to in-situ monitoring than ultrasonic methods.

Ultrasonic pulses propagating through a sample reflect off interfaces with different acoustic impedance, resulting in scattered waves from defects and the surfaces of the sample. The amplitude and arrival time of the reflective signal can yield information about the position of defects. The resolution of detection is dependent on the wavelength of ultrasound. Under ideal conditions defects with size approximately 1/10 of the wavelength can be detected [31]. Composite materials are usually inspected by ultrasonic C-scan, where the sample is scanned point by point and the signal amplitude is recorded to build up a reflection pattern. Immersion ultrasonic C-scans, allow constant, repeatable coupling to be obtained and can be automated. It has been demonstrated that delaminations and bond failures are clearly indicated in C-scan images, and voids and inclusions are also visible. It is possible to quantitatively estimate the

size of defects using C-scans, but care needs to be taken as damage size can be overestimated [32]. Delaminations could easily be detected using normal incidence ultrasonic backscattering [33]. The same study showed that matrix cracks can also be detected in tension loaded coupons with the beam at oblique incidence. Oblique incidence backscattering has also been used to detect cracks in individual ply layers, even when there was significant damage in all plies [34]. Conventional C-scans have some disadvantages, as they can be time consuming and require the sample to be placed in an immersion tank, limiting the size of the sample and making the C-scan impractical for in-situ monitoring. Jet probes, which transmit ultrasound along jets of water directed at the component, can be an alternative method to immersion C-scans [35]. Larger aircraft components can be scanned as the size of the immersion tank is no longer a limitation. However, water jet probes may be less sensitive than immersion scans [36] and are only practical at the manufacturing stage. Wheel or roller probes provide another alternative to immersion C-scans. They have the advantage of being dry coupled and are a practical solution for scanning composite aircraft components that are in service [37].

Typically, bulk ultrasound measurements are performed in the MHz frequency range. For composites, chosen frequencies are usually lower than for metallic structures as composites are highly attenuating. Unlike bulk ultrasonic techniques, ultrasonic guided waves are generated from a single location and propagate along structure. Low frequency guided waves can propagate over long distances with low attenuation within structures such as plates, pipes and rods [38,39]. This allows for rapid inspection of large areas. Guided waves propagate with energy distributed through the full thickness of the structure, and inspection frequencies are much lower than for bulk ultrasound (hundreds of kHz vs. MHz). They can be generated and detected from a single side of the sample, allowing inaccessible sections to be monitored. Guided waves are therefore ideal for in-situ structural health monitoring (SHM) of composite components. The next sections discuss guided waves propagation in composites in more detail.

2.2 Ultrasonic Guided Waves

2.2.1 Introduction to Guided Waves

Guided ultrasonic waves are elastic waves that require structural boundaries to propagate. Bulk ultrasonic waves reflect back and forth between the boundaries of a waveguide, and constructive interference occurs. After some distance, superposition causes the formation of wave packets, generating guided wave modes that propagate along the structure [38]. This enables a large area to be inspected whilst access to the structures is limited [19]. A waveguide is a structure that confines and directs the propagation of waves. Some examples of natural waveguides include plates, rods, and hollow cylinders [38]. The waveguide imposes boundary conditions on the governing wave equation of the structure, and each solution to this equation corresponds to a guided wave mode. A waveguide can support an infinite number of guided wave modes, each dependent on the material properties of the waveguide and the frequency and angle of excitation. In order to deal with this complexity, the mode and frequency used for inspection must be chosen carefully [40]. When a guided wave mode encounters a change in the thickness of a structure, for example at damage, it may convert to another guided wave mode [41]. This can result in added complexity in detected signals and should be considered when designing a SHM system [42].

The theory of elastic waves propagating in homogenous isotropic plate-like structures was developed by Horace Lamb [43]. Lamb modes can interrogate the full thickness of a sample, making them ideal for detecting internal defects within a structure. Whilst plate modes propagating in anisotropic plates, such as composites, are not strictly ‘Lamb’ modes, they display similar behaviour and so the same mode notation is widely used. Lamb wave modes are classified as symmetric or antisymmetric, dependent on the stress distribution within the waveguide. Symmetric modes have in-plane stress that is symmetric through the thickness, whereas antisymmetric modes have in-plane stress that is antisymmetric. The modes are labelled S_n or A_n, where the index n = 0, 1, 2… denotes the order of the mode. The fundamental symmetric and antisymmetric modes are labelled as S_0 and A_0 respectively. At low frequency, the S_0 mode is

dominated by in-plane displacements, resulting in a compressional wave propagating along the structure. Conversely, the A_0 mode at low frequency is dominated by out-of-plane displacements resulting in a flexural or 'bending' wave. At higher frequencies the A_0 and S_0 modes converge to form Rayleigh, or surface, waves. The modes shapes at 100kHz for the S_0 and A_0 modes along the 0° (fibre) direction in a 3.6mm thick unidirectional composite laminate were calculated using Disperse software [44] and are presented in Figure 2-2. At 100kHz (low frequency) the in-plane displacement of the S_0 mode is almost uniform throughout plate thickness, whereas the A_0 mode displays almost uniform out-of-plane displacement throughout the plate thickness.

A third mode type can also be generated in plate structures: the shear horizontal mode, characterised by in-plane displacement perpendicular to the propagation direction. The fundamental shear horizontal, SH_0, mode is non-dispersive, meaning that it has constant phase and group velocity, regardless of excitation frequency. This makes the SH_0 desirable for many SHM applications. However, in composites the SH_0 mode is coupled to the S_0 mode in the non-principal wave propagation directions, making it difficult to selectively generate and measure. Additionally, in metallic structures the SH_0 mode is often generated using an electromagnetic acoustic transducer (EMAT), however this is not appropriate for

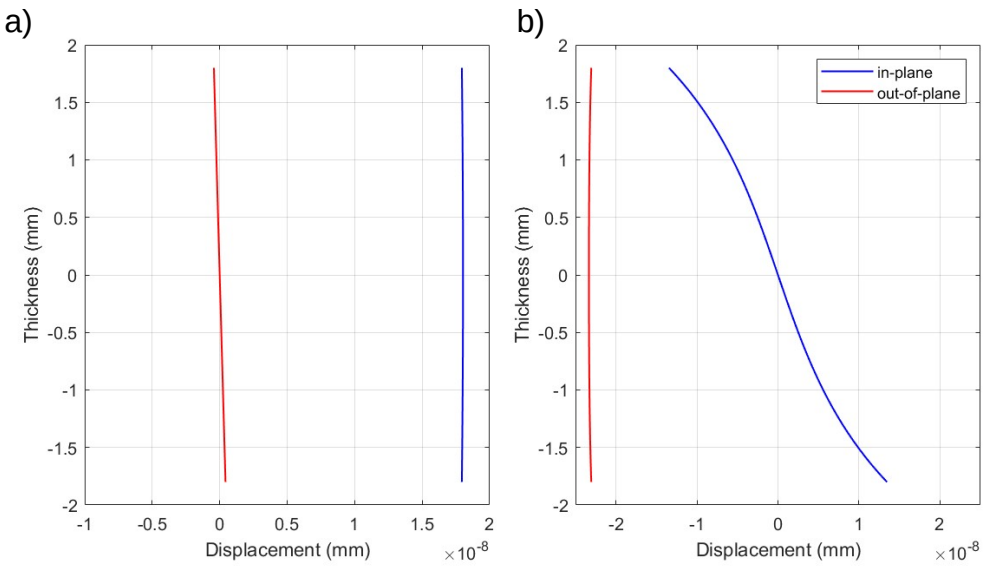

Figure 2-2 Mode shapes of the a) S_0 and b) A_0 guided wave modes at 100kHz in a unidirectional CFRP plate with 3.6mm thickness, calculated using Disperse [44].

composites due to their poor electrical conductivity. Whilst recent work has demonstrated that pure SH_0 mode excitation is possible in composites using angle beam transducers (ABT) [45], the majority of studies focus on the S_0 and A_0 modes as they are generally easier to generate and detect in composites.

2.2.2 Guided Wave Dispersion and Mode Selection

A major difference between guided waves and bulk ultrasonic waves is that the velocities of the majority of guided wave modes are frequency dependent, or in other words are dispersive. In order to understand guided wave dispersion, three wave propagation velocities need to be introduced: the phase, group, and energy velocities. The phase velocity is the speed of propagation of an individual crest of a waveform, whereas the group velocity is the speed at which the envelope of the wavepacket travels [38]. The speed at which energy travels through a medium is known as the energy velocity, and for isotropic, non-attenuating materials is equivalent to the group velocity [46]. Neau et al. [47] demonstrated that the group and energy velocities in anisotropic non-absorbing laminates were equivalent. When a material is highly attenuating, this assumption breaks down. Whilst composites do experience wave attenuation due to wave scattering at the fibres and damping from the matrix, at low frequencies the attenuation is low enough that the approximation of group velocity as equal to energy velocity holds in general [48].

All Lamb wave modes that occur in plates are dispersive. A guided wave pulse is a superposition of many different frequency components. If the group velocity of a mode is frequency dependent, the different frequency components will travel at different speeds. As the pulse propagates over long distances the pulse will become distorted and its apparent velocity will change, which could lead to damage being located incorrectly [49]. Wilcox et al. [50] proposed a technique to predict the spreading of a wave packet propagating over long distances and demonstrated that dispersion can be minimised by optimising the excitation signal.

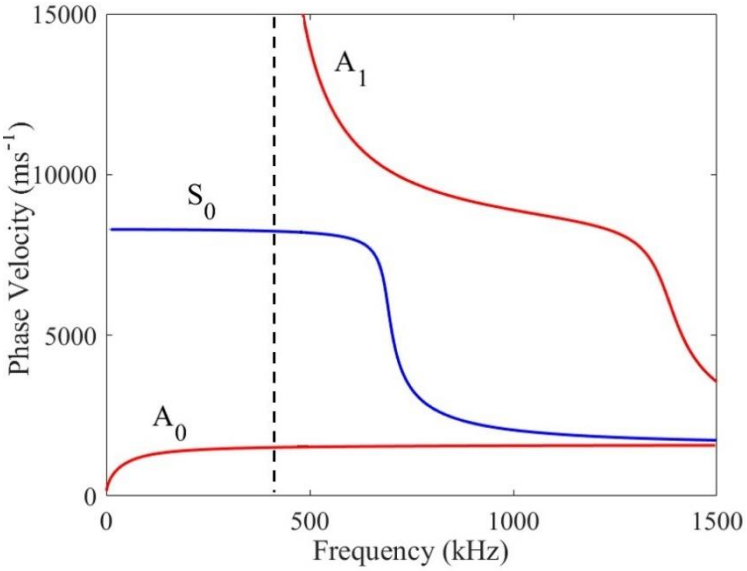

Figure 2-3 Phase velocity dispersion curves for the first three guided wave modes in a 3.6mm thick unidirectional CFRP plate, along the 0° (fibre) direction. Curves were generated using Disperse [44]. The dotted line indicates the cut-off frequency for higher order wave modes.

Disperse [44] is a program developed at Imperial College London that can be used to calculate phase and group velocity dispersion curves for guided wave modes for a range of structures. Attenuation dispersion curves and mode shapes can also be calculated. The program takes a partial wave approach to solving the governing wave equation of a structure. A brief overview of how dispersion curves are calculated in Disperse is presented here, however a full derivation can be found in the Disperse user's manual [51]. Firstly, the partial bulk wave amplitudes which can exist in each layer are determined. Then boundary conditions of the system are applied so that the stresses and displacements in each layer can be determined. This enables the system to be described in a large global matrix relating bulk wave amplitudes to the physical constraints imposed by the boundary conditions. At certain frequency/wavenumber combinations the partial waves combine to form guided wave modes. The global matrix equation can be iteratively solved by sweeping through these parameters to find the frequency/wavenumber combinations that cause the determinant of the global matrix to be zero. Once an initial root is found roots that lie on the same dispersion curve are then traced.

An example of phase velocity dispersion curves for a 3.6mm thick unidirectional composite plate is presented in Figure 2.3. The material properties used can be found in section 3.1. Only the first three guided wave modes are shown. The

dashed line shows the cut-off frequency, below which higher order modes cannot be generated. At low frequencies the S_0 dispersion curve is reasonably flat, indicating that it is almost nondispersive. The A_0 mode is dispersive at low frequencies, but the curve quickly flattens, displaying similar dispersion behaviour to the S_0 mode at low frequency. The frequency at which the curve flattens depends on the plate thickness. At high frequencies the A_0 and S_0 modes converge to Rayleigh waves, which are surface waves whose amplitude decay with depth [38]. For isotropic materials, the material properties and subsequently the dispersion characteristics of Lamb modes are the same in all directions. Crespo et al. [52] obtained dispersion curves experimentally in an isotropic plate by measuring phase and group velocity using three transducers. In order to determine the dispersion curves for an anisotropic plate, this procedure would have to be repeated in multiple directions [48], as the material properties of anisotropic materials are directionally dependent. Knowledge of the dispersion characteristics of guided wave modes are required in order to select the most appropriate guided wave mode and frequency to inspect a structure.

Several factors affect the choice of guided wave mode and excitation frequency. These include dispersion, the cut-off frequency of higher order modes, and intersections between dispersion curves so that the velocities, and therefore arrival times, of different modes are distinct, simplifying signal processing. The choice of excitation frequency is also influenced by the available operating frequency range of the employed transducer and equipment. There are some additional considerations when choosing a mode and frequency to inspect composite laminates, namely attenuation and material anisotropy. The S_0 mode is damped as a result of in-plane motion causing strain in the fibres, whereas the A_0 mode is damped due to shear motion in the matrix, resulting in greater attenuation of the A_0 mode. This means longer propagation distances can be achieved for the S_0 mode than the A_0 mode [53]. Attenuation in composites also increases with excitation frequency, which reduces propagation distances. Therefore, a low frequency is required for inspection of large composite structures in order to minimise the effects of attenuation and achieve a reasonable propagation distance. Ideally it should be possible to selectively

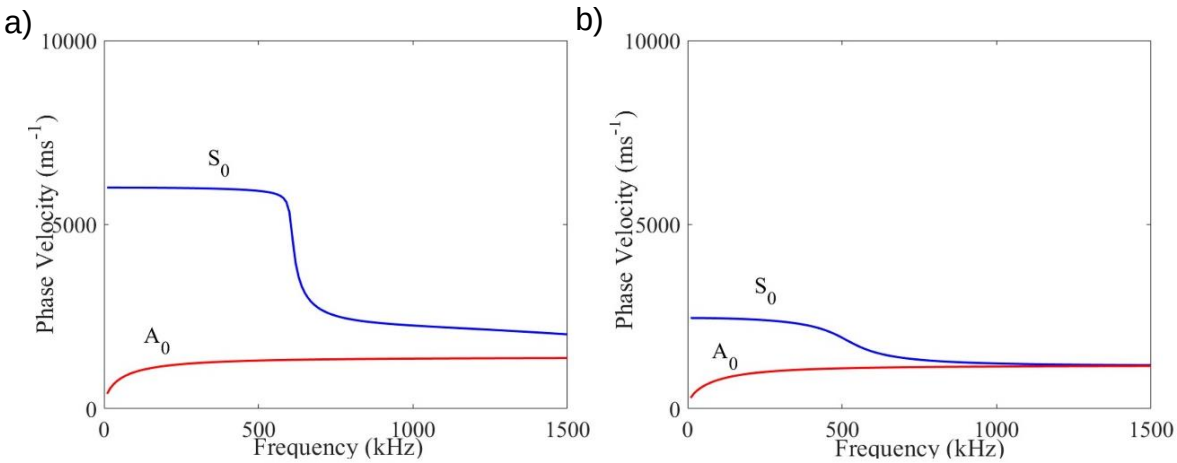

Figure 2-4 Phase velocity dispersion curves for a 3.6mm unidirectional composite plate with wave propagation oriented along a) 45° (fibre direction); b) 90° (perpendicular to fibres).

generate the chosen wave mode. For the A_0 and S_0 modes this usually involves choosing a frequency well below the cut-off frequency of higher modes. Work has been done to selectively generate higher order modes [54], however as these modes require higher excitation frequencies, the effects of attenuation limit the use of these modes in composites. Hence the majority of guided wave studies in composite plates have selected the A_0 and the S_0 mode at relatively low frequencies.

Anisotropy significantly affects the dispersion characteristics of guided wave modes in different propagation directions [48]. Figure 2-4 shows the phase velocity dispersion curves for a unidirectional CFRP laminate in the 45° and 90° directions respectively. Comparing Figure 2-3 and Figure 2-4, it can be seen that the phase velocity of the S_0 mode varies significantly with propagation direction, whereas the A_0 mode velocity varies more gradually. Choosing the S_0 mode could be advantageous in a SHM system where rapid, long-range inspection is required. As demonstrated by the dispersion curves, however, it experiences significant variation of velocity due to anisotropy. This makes damage localization more difficult as this variation needs to be considered. On the other hand, the velocity variation of the A_0 mode results in a more uniform wave propagation than the S_0 mode. Many studies have selected the A_0 mode for use in composite laminates as the effect of anisotropy, whilst still present, is not as significant as for the S_0 mode.

The reflection of the S_0 mode at damage in composites is highly dependent on the through thickness location of the delamination. For disbonds located at interfaces with zero shear stress no S_0 mode reflection was observed. On the other hand, the A_0 mode is sensitive to defects at any depth [53]. Whilst it can be argued that damage in composites often spans several ply layers and could still be detected by the S_0 mode, it cannot fully characterise damage at all depths. Additionally, the A_0 mode has a shorter wavelength than the S_0 mode at the same frequency, giving better resolution for smaller damages.

2.2.3 Anisotropic Wave Propagation Effects

Unlike isotropic structures, wave propagation in anisotropic material such as composites results in directional dependency of velocity, wave skewing, and beam spreading behaviour, caused by the material anisotropy [55]. These anisotropic effects need to be considered as they could lead to errors in locating damage, and in the worst case, result in regions of the laminate where waves do not penetrate [48]. Therefore, understanding guided wave propagation in the presence of anisotropy is required to develop accurate SHM systems for composite structures.

As discussed in section 2.2.2**,** guided wave velocities in anisotropic materials are directionally dependent, with the material anisotropy leading to higher velocities in the high stiffness (fibre) directions. Energy focusing towards the fibres also occurs, resulting in higher wave amplitudes in certain directions as illustrated in Figure 2-5. As individual mode velocities are both frequency and direction dependent, this results in three-dimensional dispersion curves [48], making damage detection more complex than for isotropic structures. With many SHM techniques dependent on time-of-flight methods [56], accurate measurement or prediction of guided wave velocities is required. In unidirectional carbon fibre reinforced plastics (CFRP), the velocity of the S_0 mode is highly directionally dependent as observed in the dispersion curves shown in Figure 2-4.

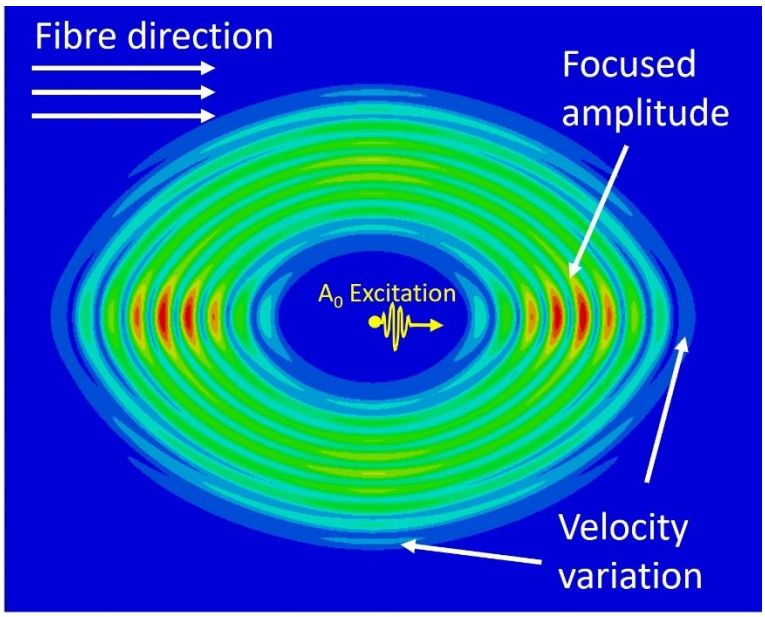

Figure 2-5 FE time snapshot of the A_0 mode excited at 100kHz in unidirectional CFRP.

The A_0 mode has lower directional variation, although still significant enough to impact damage detection [57] . The directional dependency of wave velocities in anisotropic materials has been well established. Putkis et al. measured strong directional dependency of velocity of for the S_0, SH_0, and A_0 modes in a unidirectional CFRP plate [55]. Measured A_0 and S_0 mode phase velocities in silicon wafers, an orthotropic material with similar anisotropy and steering behaviour to CFRP, were lower than predicted by theory in the non-principal directions [58]. Prosser et al. demonstrated that the propagation directions of phase and group velocity do not align in anisotropic plates and so the phase velocity should be transformed into the group direction based on the skew angle [59]. Rhee et al. proposed a magnitude and direction correction for the theoretical S_0 mode group velocities in composite plates [60].

In anisotropic materials wave energy tends to be focused away from the wave launching direction towards the fibre directions, i.e., phase and group directions are no longer equal [61]. The energy of the wave packet is steered along the group direction, but the wavefronts remain perpendicular to the wave launching (phase) direction as illustrated for a line source in Figure 2-6 [62]. The extent of the wave steering can be defined using the wave skew angle, which is the angular difference between the group and phase directions. The group direction is defined as the normal to the phase slowness curve, which is in turn defined as the inverse of the phase velocity and is illustrated in Figure 2-7 [48].

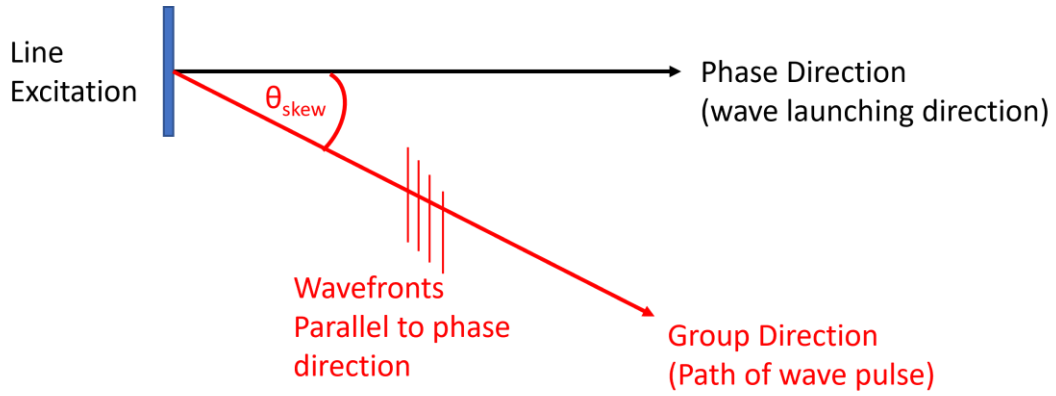

Figure 2-6 Illustration of wave skewing behaviour from a line source in an anisotropic material.

Accurate knowledge of the phase slowness curve is essential for the prediction of anisotropic effects. The extent of directional dependence of velocity and wave skewing is layup dependent. Severe skew angles up to 40° have been observed in fibre reinforced composites [54]. In addition to wave skewing, beam spreading can also occur. The ultrasonic beam widens as it propagates, with the degree of widening being directionally dependent. Increased widening is observed if the beam is launched away from the fibre directions (directions with lower stiffness) and is more pronounced for the S_0 mode than the A_0 mode [58].

Anisotropic effects can impact a variety of guided wave SHM techniques. For phased array imaging, delay-and-sum beamforming was modified with phase delays calculated to account for the skew angle and directionally dependent wave velocity [63,64]. In nonlinear ultrasound, which involves simultaneous generation of two guided wave modes, a mismatch in the skew angle can cause propagating modes to diverge. Wave skew effects can sometimes be avoided by using wave launching directions that exploit material symmetry or quasi-isotropic mode points [65]. Quasi-isotropic mode points are particular modes and frequencies with almost circular slowness curves, and therefore minimal wave skew, however such mode points may not exist in every composite structure [66]. Anisotropy has been shown to strongly influence amplitudes of scattered waves around a delamination in CFRP [57], with focusing along the fibre orientation of the outer ply layers.

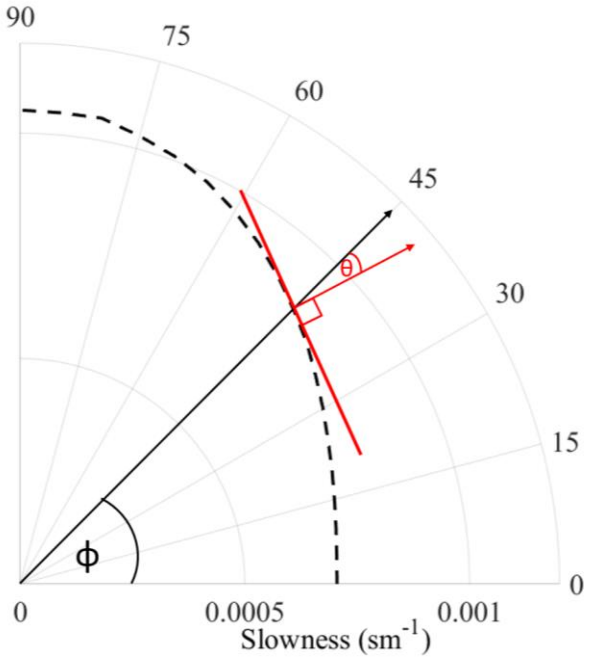

Figure 2-7 Phase slowness curve for the A_0 mode in 3.6mm thick unidirectional CFRP at 100kHz calculated using Disperse [44]. The phase angle ϕ and skew angle θ are marked. Phase direction is denoted by the black arrow, group direction is denoted in red.

The theoretical basis for wave propagation in anisotropic materials has been well established. Ogilvy [67] introduced the divergence D , a dimensionless quantity describing the rate of widening of an acoustic beam due to anisotropy, defined as the change in group direction θ_{group} , with respect to phase direction θ_{phase}:

$$D = \left|\frac{d\theta_{group}}{d\theta_{phase}}\right| \tag{2.1}$$

An isotropic material would have no additional beam divergence due to anisotropy (D=1, phase and group direction aligned), while D>1 indicates an increased rate of beam widening and D<1 a reduced rate of beam widening due to anisotropy. Newberry and Thompson represented a bulk ultrasonic beam propagating in an anisotropic medium using a series of Gauss-Hermite solutions in the far field [68]. They introduced the anisotropy factor, which was shown to be related to the divergence as:

$$A = (\cos(\theta_{skew}))^{-2} \cdot D \tag{2.2}$$

where θ_{skew} is the wave skew angle.

Karmazin developed an asymptotic solution in the far field for Lamb waves excited in composite plates [69]. Wave energy focusing in anisotropic materials has been shown to be analogue to the phonon focusing effect that occurs in crystalline structures [70] and the “walk off” or “deviation” angle terminology in the field of crystal acoustics is equivalent to the wave skew angle [71,72]. Chapuis et al. derived an analytical expression of the Green’s function for Lamb waves in the far field and showed that the anisotropy of the propagation direction induced strong focusing of Lamb modes in CFRP plates. They found that focusing directions correspond to the minima of the slowness curves [73]. Potel et al. used plane wave decomposition of the incident wave beam to determine the wave skew angle. Experimental and numerical results illustrated the strong deviation of a beam towards fibres in a unidirectional plate predicted by the theoretical results [74]. Chronopoulos expressed the wave skew angle as a function of material properties of an anisotropic structure and proposed an efficient Finite Element Analysis (FEA) method that matched the theoretical predictions [75]. Biot’s energy approach was extended to derive the Lamb wave group velocity and subsequently skew angle in a composite plate [76]and showed good agreement with FE predictions [77].

Relatively few studies have considered anisotropic wave propagation effects experimentally. Several studies have considered the directionality of the group/energy velocity in anisotropic materials [47,55,62,78,79], but relatively few have experimentally measured phase velocities in multiple wave propagation directions [80]. Lamb wave propagation in monocrystalline silicon wafers, which like CFRP is an orthotropic material, was investigated experimentally and numerically. Measured wave skew angles were well matched for the A_0 mode but a systematic offset was observed for the S_0 mode [58]. Beam spreading was also shown to increase as the orientation of the incident guided wave beam moved away from the high stiffness directions, but this was not compared with theoretical predictions. Putkis et al. measured strong directional dependency of velocity for the S_0, SH_0, and A_0 modes in a unidirectional CFRP plate [55]. Chapuis et al. demonstrated energy focusing of the A_0 and S_0 modes generated by a PZT disc in cross-ply CFRP through wavefield measurements and demonstrated that the energy focusing effect can

be described by the Maris factor [81]. Salas and Cesnik used a ring-shaped transducer with multiple elements to launch waves in different directions and used wavefield imaging to qualitatively demonstrate the wave steering behaviour in unidirectional, cross-ply, and quasi-isotropic laminates, but comparison was not quantified or compared to theoretical predictions [82]. Potel et al. measured the wave skew angle of the S_0 mode in a single wave propagation direction, showing good agreement with predicted angles [74]. Lowe et al. used a linear source consisting of multiple PZT discs to launch waves at 20° to the fibre direction in unidirectional CFRP and measured a steering angle consistent with theoretical predictions [48].

2.3 Damage Detection in Composites

2.3.1 Guided Wave Measurements in Composites

Several methods are used to generate and detect ultrasonic guided waves, including piezoelectric transducers, air-coupled transducers, laser-based ultrasound, EMATs, and laser Doppler vibrometry. Piezoceramic transducers are one of the most common transduction devices used for both generating and detecting Lamb waves. They are able to generate in-plane and out-of-plane strains in a sample and are cheap and lightweight. Networks of piezoelectric sensors can be embedded into composite laminates [83,84], providing a potential in-situ SHM system. However, complex data acquisition and processing is required to monitor samples in real time.

Electromagnetic Acoustic Transducers (EMATs) are devices consisting of a coil and a permanent magnet [85]. When an alternating current is passed through the coil an alternating current is induced in the sample. This produces a Lorentz force, generating particle vibration in the sample. EMATs are non-contact but generate much smaller amplitudes than piezoceramic transducers. They require a conductive sample, which limits their application to composites. Putkis et al. [55] successfully used an EMAT to detect the S_0 mode in a carbon fibre composite plate. As composite laminates have poor electrical conductivity, aluminium tape was applied to the specimen surface to enable coupling of the EMAT to the specimen.

Air coupled transducers generate and detect changes in the pressure field of air above a sample. They are non-contact, which is advantageous for in-situ monitoring on a single side of the specimen [86]. They have been successfully used to detect damage in composite laminates and are particularly useful for monitoring composite structures that cannot be immersed, such as honeycomb composites [87].

Laser Doppler vibrometers (LDV) are often used to detect ultrasonic waves. When the laser beam is reflected from a vibrating source the frequency of the reflected beam is shifted. This shift is measured and related to typically the out-of-plane velocity using the Doppler effect. The accuracy of the amplitudes detected depends on the quality of the reflected laser beam (speckle), so reflective tape is often applied to the sample in order to improve reflection. More recently a non-permanent reflective spray has been used to achieve good reflection [88]. Usually, the LDV is attached to a scanning rig which can provide accurate spatial positioning of the recorded signal [2]. LDV is a non-contact method with very high spatial resolution, however it is an expensive technique, and a high level of resolution is not required for all applications. Additionally, LDV typically has a poorer signal-to-noise ratio (SNR) than piezoelectric transducers. In contrast, piezoelectric transducers have lower spatial resolution, but are significantly cheaper and more practical to implement for SHM.

2.3.2 Modelling Techniques for Composite Damage

Systematically studying guided wave propagation and scattering experimentally requires a large number of samples, making experimental investigations costly for both time and resources. Additionally, due to the unique nature of impact damage, it can be difficult to make experiments repeatable. Numerical modelling can be used to efficiently investigate guided wave propagation and scattering in composite laminates. The majority of work has been carried out using Finite Element Modelling (FEM), but other techniques such as the Semi-analytical Finite Element (SAFE) method [89] and the Elastodynamic Finite Integration Technique (EFIT) [90] have been used to simulate guided wave propagation.

Early investigations [53,91] carried out 2D simulations of pristine and delaminated composite laminates. The models could only represent laminates with defects across the full width of the plate, which does not capture the full characteristics of real delaminations. As computational resources have improved in recent years, many studies have been carried out using 3D finite element techniques. A full 3D representation of damage provides a more realistic model of a damaged sample.

Several methods have been used to model damage numerically, particularly delaminations. Locally reducing the stiffness of elements to create a ‘soft region’ can be used to model damage [92]. Impact damage and delamination causes the strength of a composite laminate to reduce dramatically. The extent of strength reduction, however, is variable [93] and so it can be difficult to decide the required extent of change in the material properties. Another method is to create a ‘zero-volume’ delamination, by detaching elements across the delaminated region. This can be achieved either by modelling the two sub-laminates as separate plates and applying a tie constraint over the whole face of the plate except for the delamination region. Alternatively, this can be achieved by overwriting elements in the damage region. Tian et al. [94] modelled damage as a zero-volume square delamination and carried out experimental measurements on a sample with an artificial square delamination. Whilst good agreement was found between the model and experiment, a square delamination is not representative of real damage. Murat et al. [95] modelled both square and circular delaminations in a composite plate and found that the scattering pattern was similar for both shapes, suggesting that the size of the delamination affected scattering more than the exact shape of the defect. The ratio of the wavelength of propagating waves to the dimensions of damage have a significant effect on the scattering patterns detected. Therefore, when the characteristic length of a square and circular delamination is equal this will result in similar scattering patterns. This effect is further discussed in section 2.3.4.

Mixed mode delamination, containing both a zero-volume defect and a region of reduced stiffness, was used to model material degradation, and was found to be a good approximation of impact damage [95]. Models for low velocity impact damage have been taken a step further, by incorporating real damage data into FE simulations. Smith et al. [96] incorporated ultrasonic C-scan data of a wrinkled ply layer into a model to successfully model this type of defect, whereas Leckey et al. [14] incorporated X-ray CT scan data of impact damage into the simulation. Zhang et al. [97] and De Luca et al. [98] used a similar method but acquired damage data from a separate model of a drop impact. These methods provide a more realistic representation of damage than a circular delamination, or a soft region. However, they require prior data which is not always available from a physical sample.

2.3.3 Detection of Low Velocity Impact Damage

In order for a reliable NDE or SHM system to be developed, the interaction of guided waves with realistic damage, such as low velocity impact damage, needs to be understood. Kudela et al. [99] compared scattering from an artificial insert delamination with low velocity impact damage through both experiment and simulation. They found that the delamination was much easier to detect than the impact damage, suggesting that damage detection methods that are sensitive to inserts may not be suitable for more realistic damage.

Impact energy has a significant effect on the damage pattern. When subjected to low velocity impact, a structure absorbs incident energy over a larger area than that of a high velocity impact, resulting in BVID [93]. The nature and extent of low velocity impact damage was also found to depend on geometrical properties of the laminate such as fibre stacking sequence and thickness [1]. Experimental measurements of the A_0 mode interaction with low velocity impact were carried out [100]. An increase in received energy was detected in certain directions, indicating that damage acts as a scattering centre. Murat et al. [101] investigated the A_0 mode propagation in two identical impact damaged plates. A significant change in signal shape and increased amplitude observed was in the damaged region, indicating multiple reflections. While each impact damage is unique, similar scattering patterns were seen between the two plates. Networks

of piezoelectric patches have been used to locate and size impact damage. For example, Diamanti et al. [102] performed guided wave measurements and simulations on a repeatedly impacted composite plate. The reflection coefficients of the A_0 mode were calculated and provided a means of sizing damage. This method, however, overestimated damage size. Wang and Chang [83] also used a network of piezoelectric sensors in impacted and pristine CFRP plates. Whilst they could accurately locate damage, the size of damage was again overestimated, particularly when the damage was large, and damage mechanisms more complex. Techniques such as this could be used for an initial global detection method and followed up with a more accurate characterization technique.

Some studies of impact damage interaction have focused on the major delamination, which has the largest area and is usually located in the lower lamina of an impacted plate. The reason for this is that delaminations are a critical damage mode responsible for the majority of strength reduction and have been shown to scatter guided waves more strongly than matrix cracks [97]. Experimental [103] and numerical [11] studies considered scattering of the S_0 from the major delamination. The size and location of the defect was found to be in good agreement with the experimental results; however, baseline data of the undamaged laminate was required. Analysis of the wave structure indicated the presence of standing waves trapped within the delamination.

2.3.4 Guided Wave Interaction with Delaminations

Whilst numerical and experimental studies have demonstrated that guided waves can be used to detect delaminations, scattering at a delamination remains a complex problem. The anisotropy of a multi-layered plate influences the direction of scattered waves [104,105]. Mode conversion and scattering occur when guided waves interact with a delamination. These effects can be used to detect and characterise damage [103]. Waves propagate in each of the sub-laminates above and below the delamination, typically with different velocities depending on the ply layup [106]. Numerous studies have reported that the amplitude of guided waves increased significantly over the delamination area, which could be exploited for damage detection [91,107]. This effect is

particularly pronounced for the A_0 mode, as the bending stiffness of thinner laminates is lower. The increase in amplitude is also caused by multiple reflections within the sub-laminates constructively interfering and generating standing waves, ‘trapping’ energy around the delamination area [108]. This increase in amplitude can be exploited for damage localization, and the difference in arrival times between multiple reflections can be used to estimate delamination size [109].

Wave trapping has been observed in both numerical simulations and laser doppler vibrometer measurements [94]. Several image processing techniques have been developed to take advantage of this behaviour and to highlight delaminations. Sohn et al. [108] proposed a standing wave filter in order to emphasise standing waves surrounding a delamination, whereas Testoni et al. [110] used a warped curvelet transform to remove the incident wave to isolate the reflected waves from the delamination. Kudela et al. [111] developed a selective weighted root mean square algorithm to generate clear damage maps for delaminations in cross ply panels with uniform thickness. The wave trapping phenomena has been used to distinguish between different sized delaminations at several depths for multilayer damage [112].

Scattered amplitudes and scattering directivity patterns depend on the ratio of delamination size to wavelength and the through thickness location of the defect [113]. Both backscattered and forward scattered amplitudes can be observed, the amplitude of the latter being dependent on the phase difference between waves propagating in each of the sub-laminates [114]. When a delamination is located at an asymmetric depth, a high trapped amplitude can be observed on top of the thinner sub-laminate [107,115]. Delaminations located towards the mid-plane experience less wave trapping but have a higher scattered wave amplitude [116]. The scattering directivity pattern has been shown to be influenced by the fibre orientation of the outer plies of the laminate, due to fibre steering effects [105]. Scattering patterns depend on the layup sequence, even for laminates with the same number of ply layers [104]. Mei et al. found that the number of delaminations at the same location with different depths has an influence on the scattering pattern and the amplitude of trapped waves [117].

Mode velocity, wavelength, and deflection angle at a square delamination were found to vary with delamination depth [118,119].

Several studies have investigated the scattering directivity of the A_0 mode at a delamination numerically [95,113,120]. However, relatively few have validated the numerical simulations experimentally on the studied damage cases. Murat et al. performed a systematic study on the influence of interlaminar damage depth and size through 3D Finite Element (FE) simulations with a zero-volume square delamination, compared with experimental results for BVID [95]. Strong forward scattering was observed for both square and circular delaminations. Ng and Veidt [113] used 3D FE simulations to investigate the A_0 mode scattering at circular delaminations of various depths and sizes. The numerical model was verified experimentally for an artificial delamination created by an insert embedded at the laminate mid-plane. Pudipeddi et al. [120] performed a numerical investigation of mode conversion and scattering in a quasi-isotropic laminate containing circular delaminations of various depths and sizes. The discrete model was validated experimentally for the case of an undamaged laminate. Both Pudipeddi et al. and Ng et al. found delamination depth had a significant effect on the amplitude and directivity of scattered waves. The influence of directionality (incident wave direction) on scattering directivity of the A_0 mode around delaminations in composite laminates is yet to be ascertained.

2.3.5 Simulated Delamination Damage with Magnet Targets

Specimens containing artificial delaminations, created by placing a film between the ply layers during manufacturing, are often used to study guided wave scattering in composites. This enables the size, location, and depth of damage to be controlled. To avoid the requirement for multiple specimens with permanent damage for the development and testing of SHM algorithms (e.g., for sparse array imaging as described in the following section), magnets, placed on opposite sides of a structure, are easily removed from a specimen and have been used in several studies to simulate damage [121–124]. For example, Williams et al. [122] experimentally investigated the scattering directivity around magnets mounted on a quasi-isotropic composite panel using sparse array and noncontact laser measurements. Magnets provide a simple and cost-effective

method to experimentally simulate damage in composites. The influence of anisotropy on scattering directivity around a magnet, however, has not been studied numerically for composites.

2.3.6 Sparse Array Imaging

Sparse array imaging, using a distributed sensor network, provides a cost efficient in-situ SHM solution. Various imaging algorithms for sparse arrays of distributed sensors have been developed to localize damage, the majority of which require baseline subtraction data. Clarke et al. demonstrated that environmental conditions could have a significant effect on baseline signals, and the subsequent performance of imaging algorithms [125]. Wang et al. [126] developed delay and sum (DAS) imaging for isotropic structures, for which the group velocity is the same in all directions. Hall et al. developed minimum variance (MV) [127] and multipath imaging [128]. These algorithms adaptively weigh signals based on prior knowledge of the defect. This results in improved imaging compared to DAS with fewer artefacts. However, MV imaging requires prior knowledge of the scattering behavior of a particular defect in all directions. Scattering information for a defect can be summarized using 2D scattering matrices, where the respective wave amplitude at each combination of incident and scattered direction is recorded [122,129]. The performance of sparse array imaging algorithms is impacted by material anisotropy [130]. Williams et al. demonstrated the robustness of minimum variance distortionless response (MVDR) imaging in a quasi-isotropic composite plate by using directional velocity distribution to weigh the damage probability index [131]. Bao et al. developed the model based modified MUSIC algorithm to account for material anisotropy [124]. Ostiguy et al. [130] compared the performance of several imaging methods for detecting damage in a unidirectional composite laminate and found that whilst some methods are robust for mild anisotropy, severe anisotropy needs to be considered in the imaging algorithms. In order to do this, the influence of anisotropy on the full scattering characteristics of damage in composites needs to be understood.

2.3.7 Complex Geometry Composites

Guided wave propagation and scattering in flat composite plates has been discussed in detail so far. However, understanding guided wave interaction with more realistic geometries such as curved panels, spars, and stiffeners will be required for SHM of such structures. This section discusses the influence of geometry on guided wave propagation behaviour, before presenting examples of damage detection in composite specimens with complex geometries.

The curvature of a plate has been demonstrated to influence the dispersion characteristics of propagating modes. Variations in mode shapes and phase and group velocities occur in comparison to a flat plate, with the degree of variation being dependent on the radius of curvature. At low curvature it has been shown that dispersion curves of a curved plate converge to those of a flat plate [132], which indicates that the SHM techniques developed for flat plates discussed in previous sections are appropriate for realistic structures such as aircraft fuselage. For plates with higher curvature, the dispersion curve of the A_0 mode at low frequency matches that of a flat plate, however the S_0 mode shows significant variation [132,133]. Due to the geometry of the waveguide, modes propagating in a curved plate no longer have strictly symmetric or antisymmetric mode shapes, and so the A_0 and S_0 modes in a curved plate are referred to as “quasi-plate” modes. When guided waves interact with more severe curvature, reflection and mode conversion can occur [134,135]. Guided waves at low frequency have been demonstrated to propagate around sharp bends in thin composite structures [136] and U-shaped bends in thicker laminates [137]. Mode conversion was observed across the bend.

As briefly discussed in section 2.2.1, the thickness of a structure influences guided wave propagation. For slow variation in the thickness, it can be assumed that Lamb wave modes at constant frequency have the phase and group velocities associated with the local thickness [138]. Thus, variations in phase and group velocity can be used to map the thickness of a structure. Mode conversion can also occur as the result of a thickness change [41]. The frequency and thickness of guided wave modes are intrinsically linked. As such, for modes propagating at constant frequency but with varying thickness, there

exists a cut-off thickness below which higher modes cannot propagate [139]. If a cut-off thickness is approached either the mode is reflected as if it was approaching a discontinuity, or wave energy is transmitted as a lower order mode. Nurmalia et al. studied the mode conversion behaviour of fundamental and first order guided wave modes at both slow and abrupt changes in thickness [139]. For the SH_1 mode propagating in a tapered region, total reflection occurred. The A_1 mode displayed similar behaviour; however, some energy was transmitted as the A_0 mode.

Damage detection in flat composite plates is complex due to the material anisotropy and multi-modal damage mechanisms. In more realistic composite structures these effects compound with the influence of the geometry on wave propagation, making interpretation of guided wave signals more difficult. Additionally, composite parts in service can include regions which have been repaired. These regions have been shown to significantly reduce the amplitude of propagating guided waves, adding additional complexity to SHM [140]. For typical curved composite structures such as T-joints or L-stiffeners, damage is more likely to occur in the bends, with the first failure initiation as a delamination perpendicular to the bend radius [141]. The web flange junction of a T-stiffener is also prone to cracking and delaminations, which is partly due to twisted fibres and non-uniform fibre distribution in the curved zones. Disbonds between the interface of a stiffener and the panel it is attached to can commonly occur [142]. Ramadas et al. were able to characterise the length and width of an interface delamination in a composite T-joint by exploiting multiple reflections of turning modes that propagated around the web flange junction [143]. However, this method required guided waves to be excited at the web of the stiffener, which is not always accessible. Geetha et al. observed mode conversion at an artificial rectangular delamination in the web flange interface and reconstructed the damage from a sparse array of grid points [144]. They noted several shadow regions in the specimen where waves could not propagate. Philibert et al. mounted pairs of transducers on a composite T-joint and used them to generate dispersion and tuning curves for a baseline and impact damage case [145]. The presence of impact damage influences the dispersion and tuning curves; however, this method was unable to characterise damage. Chang observed

changes in wavenumber due to impact damage and via a Reisz transform was able to isolate these changes from material/geometrical discontinuities in order to image damage [146]. Spytek used wavefield imaging of Lamb waves to detect artificial delaminations in a scale model of a realistic aircraft component, then followed up with high resolution laser ultrasound inspection to fully characterise damage [147].

Several studies have also exploited feature guided waves, which are guided waves confined to a local structural variation, to inspect composite bends. Yu et al. were able to confine a SH_0-like “bend guided” mode along a 90° bend in a quasi-isotropic composite laminate, such as those found in rectangular and C-shaped wing spars [148]. Wave trapping behaviour was observed at delamination, and reflections from transverse cracks were detected. Manogharan et al. studied feature guided waves propagating in the “noodle” regions of composite T-joints [149]. More energy confinement was observed when waves were focused along the fibre orientation of the noodle. Whilst it has been demonstrated that guided waves are able to propagate in complex structures, further work is required to fully understand guided wave propagation and interaction around damage in order to develop SHM systems for such components.

2.4 Literature Gap and Motivation

CFRP composite laminates are increasingly being selected for the manufacture of aerospace components as they reduce the weight of structures whilst maintaining mechanical strength. Reliable SHM techniques are required for safe aircraft operation. Low frequency ultrasonic guided waves provide a promising in-situ monitoring solution for composites as they are able to propagate long distances with low attenuation and are able to rapidly inspect large areas and inaccessible regions of a structure. However due to the complex material structure and damage mechanisms of composites, the interaction of guided waves with damage in anisotropic composite laminates is not yet fully understood. This study investigates the propagation and scattering of the fundamental symmetric A_0 Lamb wave mode with delaminations in anisotropic CFRP composite laminates. It is hoped that by understanding the fundamental

wave propagation effects in composites studied in this thesis, more accurate SHM systems for composite structures can be developed.

Based on the discussion throughout this chapter, the overarching aims of this PhD study are as follows:

- Improve the understanding of anisotropic wave propagation effects on guided waves (A_0 Lamb mode) in composite laminates.
- Improve the understanding of guided wave scattering at circular delaminations.
- Compare guided wave scattering at a delamination and magnet target and determine the suitability of using magnets to simulate damage in composites.
- Investigate the influence of material anisotropy on scattering at damage.

Building on the literature presented in section 2.2.2, the A_0 mode has been selected due to its ability to detect delamination damage at all depths, and shorter wavelength than the S_0 mode at the same frequency, offering improved resolution of damage. It has been demonstrated that anisotropic wave propagation effects of the A_0 mode, such as the directionality of wave velocity, wave skew, and beam spreading can significantly impact SHM. The theory of guided wave propagation in anisotropic materials has been long established, however experimental demonstration of these effects, and comparison to theoretical predictions, has been limited. The directionality of group velocity in composites has been measured by several authors, but equivalent studies of phase velocity are rather limited, and thorough comparison with theoretical values from dispersion curves has not been demonstrated. The general concept of wave skewing and its prediction from the phase slowness curve is well known, but again experimental studies are limited. Previous studies have observed steering effects in experimentally measured wavefields but have not quantified them. Others have quantified the wave skew angle in a single wave propagation direction. Beam spreading effects have been observed in other anisotropic materials such as silicon, but the extent of the spreading was not quantified or compared to theoretical predictions. Quantitative measurement of

beam spreading effects in CFRP and comparison to theory has not yet been demonstrated. Chapter 5 aims to address these points, by providing a full systematic study of anisotropic guided wave behaviour in a unidirectional composite laminate through both FE simulation and experimental measurements.

Delamination damage causes significant strength reduction of composite structures, making it one of the most critical damage types to detect reliably. Due to this, several studies on guided wave interaction with impact damage have focused on the major (largest) delamination. Interaction of guided waves with composite delaminations has been shown to be a complex problem, partly due to the anisotropic wave propagation effects discussed above, but additionally due to the numerous parameters that affect guided wave scattering such as damage size, shape, depth, and orientation. Several studies have looked at the influence of these parameters on scattered waves through FE modelling, however there are few examples of experimentally measured guided wave scattering at a delamination to validate the numerical studies. Permanent magnets are a practical method to simulate damage whilst developing SHM techniques, as they can easily be repositioned without damaging the structure, reducing the number of physical specimens required. The suitability of magnets as a model for delamination damage has not yet been fully ascertained.

Previous work has shown that material anisotropy can significantly influence guided wave propagation in composites, however the effect of anisotropy on the scattering at damage has not yet been considered. Chapters 6 and 7 aim to address these points. The development of a FE model of circular and ellipse shaped delaminations is presented in Chapter 6 and is validated against experimental measurements around an artificial insert delamination in a quasi-isotropic laminate. Chapter 7 aims to understand guided wave scattering in more detail by presenting parameter studies of delamination size, shape, and depth. Anisotropic effects on scattering at a delamination are considered by varying the incident wave propagation direction in both the simulation and the experiments. Scattering directivity around permanent magnets is also studied numerically and experimentally. The implications of these effects on the SHM of composites is addressed.

3 Composite Specimens and Experimental Setup

This chapter presents the description of composite specimens and general information about experimental equipment and guided wave measurements. Details of each of the composite specimens are presented, followed by description of the non-contact laser measurements. Details of the piezoelectric transducers used to generate guided waves, permanent magnets used to simulate damage, and choice of couplant are discussed. Specific experimental details such as excitation frequencies and scanning geometries are presented in the relevant results chapters.

3.1 Undamaged Unidirectional Specimen

The undamaged, unidirectional plate photographed in Figure 3-1 was manufactured at Imperial College London and was used for the wave propagation measurements described in Chapter 5. The plate consists of 24 plies with fibres oriented along a single direction and the ply thickness is 0.15mm, giving a plate thickness of 3.6mm. The in-plane dimensions of the plate are 1.14m × 0.94m as shown in Figure 3-2. The corners of the rectangular plate were removed prior to this investigation. The material properties of the plate were characterized using a 2MHz air-coupled transducer at the University of Bordeaux [61].

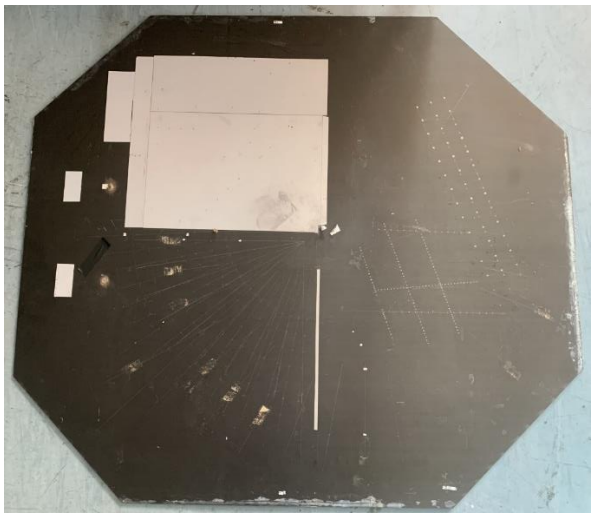

Figure 3-1 Photograph of the unidirectional composite specimen.

Material properties of a composite specimen can either be described by a set of engineering constants, consisting of Young's moduli and Poisson ratios, or a set of nine orthotropic stiffness coefficients C_{ij}. To fully describe the material the density ρ is also required. For the unidirectional specimen the complex orthotropic stiffness coefficients are listed in Table 3.1. Both the real (stiffness) and imaginary (attenuation) parts of the coefficients are shown. The orientation of the material properties is shown in Figure 3-2b.

Table 3-1 Orthotropic stiffness constants for the undamaged unidirectional specimen. All values in GPa unless otherwise stated [61].

C_{11}	12.56+i0.34
C_{12}	6.84+i0.25
C_{13}	6.47+i0.65
C_{22}	13.15+i0.65
C_{23}	5.6+i0.60
C_{33}	109.9+i8.23
C_{44}	4.7+i0.28
C_{55}	4.0+i0.25
C_{66}	2.27+i0.25
ρ	1550 kgm^{-3}

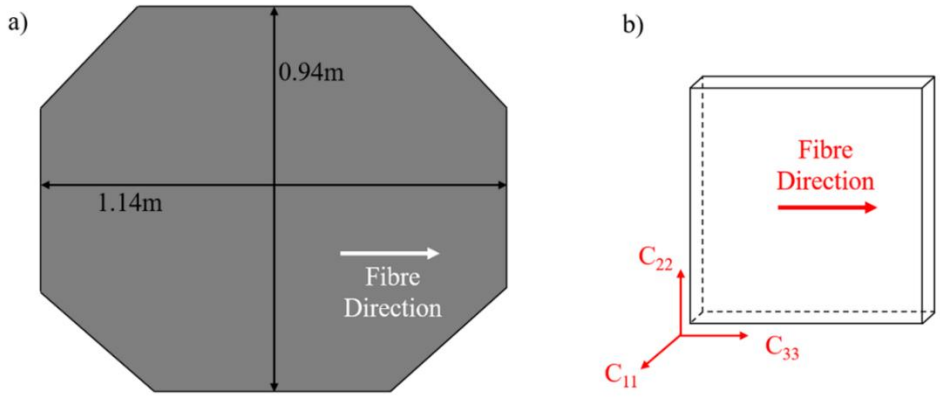

Figure 3-2 a) Schematic and dimensions of unidirectional plate. b) Orientation of material properties.

3.2 Quasi-isotropic Laminate With Artificial Delamination

An 8-ply quasi-isotropic graphite/epoxy laminate with layup $[-45/45/90/0]_s$ and dimensions 600mm x 600mm x 1.6mm was loaned by Dr Leandro Maio at the University of Naples and used for scattering measurements presented in Chapter 6 [150]. The panel was manufactured using unidirectional pre-preg plies and manual lay-up. The material properties of a single ply layer are given in Table 3-2. An artificial insert delamination was manufactured at the centre of the panel by inserting a circular polytetrafluoroethylene (PTFE) film, 15mm in diameter and 0.02mm thickness. The film was placed between the second and third plies during the layup process to produce a delamination at depth 0.4mm as shown schematically in Figure 3-3b. The resulting CFRP laminate was then cured in an autoclave. The cure cycle consisted of raising the temperature from 30°C to 175°C at 2.5°C/min and was held at 175°C for 120 minutes at 3.5atm. The position of the delamination was verified through an ultrasonic C-scan (Olympus OmniScan SX, 5MHz phased array probe). The ultrasonic C-scan is shown in Figure 3-3c. An oval shaped crown was identified indicating detached plies, giving an actual flaw size of approximately 20mm x 16mm [151].

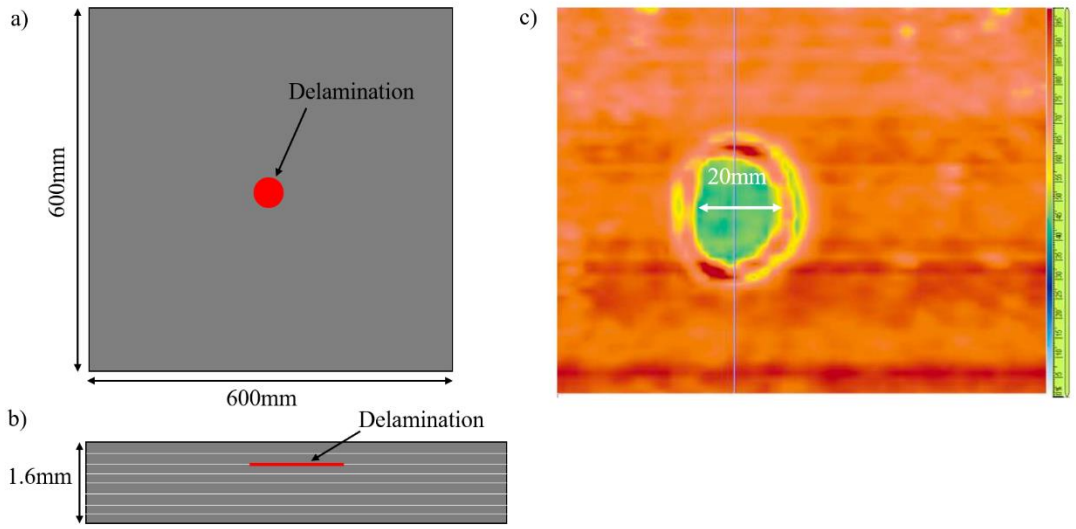

Figure 3-3 Schematic of a) delamination position, b) delamination depth for the quasi-isotropic laminate; c) Ultrasonic C-scan of delaminated region, reproduced from [151].

Table 3-2 Material Properties (engineering constants) of single ply layer of quasi-isotropic laminate, as given in [150]. All values in GPa unless otherwise stated.

E_1	175
E_2	6.90
E_3	6.90
G_{12}	4.18
G_{13}	4.18
G_{23}	2.35
V_{12}	0.25
V_{13}	0.25
V_{23}	0.46
ρ	1520 kgm^{-3}

3.3 Non-contact Laser Measurements

Guided wave measurements were performed on each of the composite specimens described above using a laser Doppler vibrometer. A diagram for the general setup of guided wave measurements is presented in Figure 3-4. A piezoelectric transducer is bonded to the surface of the composite specimen and used to excite the A_0 guided wave mode. Further details of the transducers used are given in section 3.4. A 5-cycle sine wave modulated by a Hanning window was chosen as the excitation signal and generated in a frequency range of 50-100kHz (specific frequencies are discussed in relevant results chapters). The amplitude of the excitation signal, A is given by

$$A = 0.5\sin(2\pi ft)\left(1-\cos\left(\frac{2\pi ft}{N_{cyc}}\right)\right) \tag{3.1}$$

where f is the centre frequency of excitation and N_{cyc} is the number of cycles present in the signal and the amplitude factor of 0.5 was chosen so that the peak-to-peak amplitude was equal to 1. The narrowband excitation signal was generated using a programmable function generator (Agilent 33220A) connected to a PC and controlled using LabVIEW. Signals were

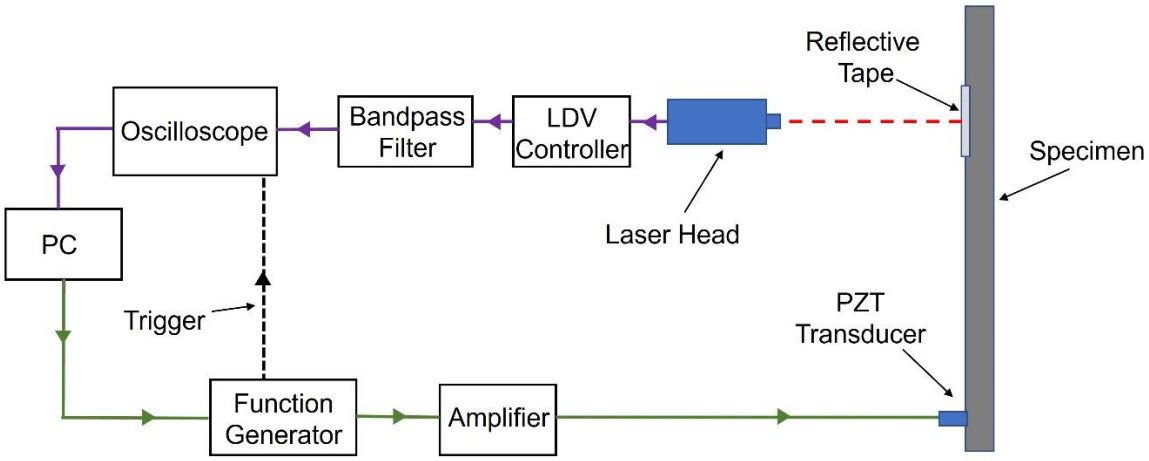

Figure 3-4 Schematic of experimental setup for LDV guided wave measurements.

then amplified (Krohn-Hite 7062M wideband amplifier) before being applied to the transducer. A laser Doppler vibrometer (LDV) (Polytec sensor head OFV-505, OFV-5000 vibrometer controller) was used to measure the velocity of the out-of-plane displacement of the plate surface. The laser head was attached to a scanning rig that can move parallel to the plate. The scanning rig was connected to the PC controlled by LabVIEW. This enabled the position of the laser head to be defined and horizontal and vertical line scans, circular line scans and grid (raster) scans to be performed. Reflective tape was applied to the sample surface to improve laser beam reflection and, consequently, the SNR. The signals were filtered using a Butterworth band pass filter (Krohn-Hite 3945 programmable filter), set to 25kHz above and below the centre frequency of the excitation signal, and averaged 20 times before being recorded using a digital storage oscilloscope (LeCroy 9304). The signals were saved to a PC to be further analysed in MATLAB.

3.4 Transducers

Three different types of PZT transducer were used to generate the A_0 mode: a PZT disc with brass backing mass, a PZT disc with wraparound electrode and a line transducer. Details of each transducer are presented here.

The brass backed PZT disc, photographed in Figure 3-5a, was used for point source excitation of the A_0 mode in the unidirectional composite plate, the

results of which are presented in Chapter 5. The transducer consists of a Ferroperm Pz27 disc (diameter 5mm, thickness 2mm) and a brass backing mass (diameter 5mm thickness 6mm) which were bonded together using Loctite 2-part epoxy glue. A thin layer of silver conductive paint (Electrolube SCP03B) was applied to the plate at the desired transducer location. The transducer was then bonded to the painted region using epoxy glue. A BNC cable was attached to the transducer as shown in Figure 3-5a using aluminium conductive tape. The conductive tape has the advantage that the cable can easily be removed and repositioned. This transducer was previously designed for use at 100kHz attached to an aluminium plate. The highest signal amplitude in the composite plate was achieved at an excitation frequency of 100kHz, but good repeatable signal amplitudes can be generated at frequencies in the 50-100kHz range.

A PZT disc (PIC-255) with wraparound electrode, as photographed in Figure 3-5b, was used for guided wave measurements on the quasi-isotropic panel described in section 3.2, the results of which are presented in Chapter 6. The disc had a diameter of 10mm and a thickness of 0.25mm and was bonded to the plate surface using cyanoacrylate glue. Wires were soldered to the electrodes. The highest signal amplitude with good, repeatable signals was generated at an excitation frequency of 50kHz, although reasonably good signal amplitude can be obtained in the region of 40-80kHz.

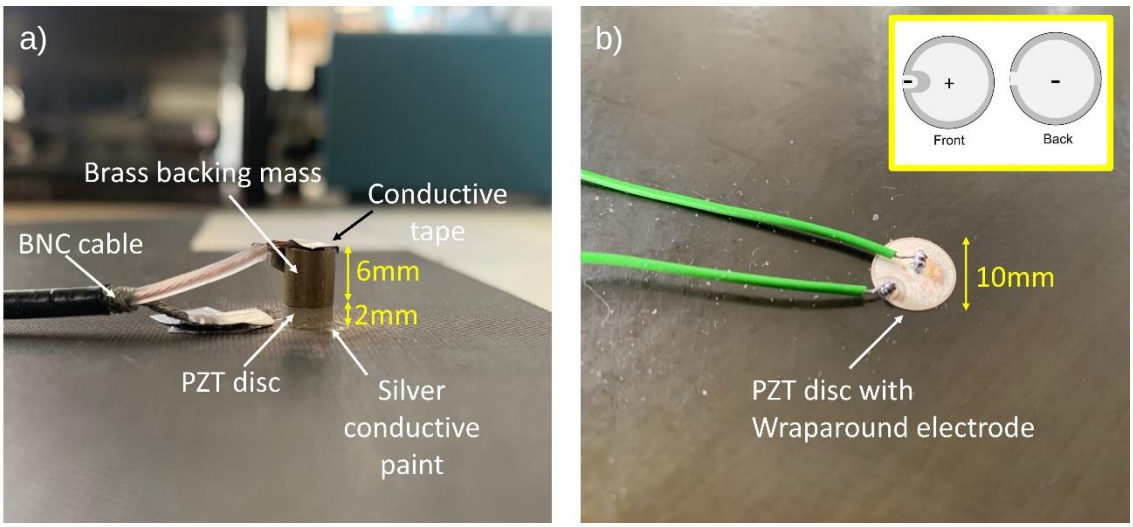

Figure 3-5 a) PZT disc transducer with brass backing mass; b) photograph of PZT disc with wraparound electrode. Inset: schematic of front and rear view of PZT disc with positive and negative electrodes denoted.

A line transducer was developed in order to produce a linear excitation of the A_0 mode, as used for the wave skew measurements on the unidirectional plate in Chapter 5. The line transducer, photographed in the inset of Figure 3-6a, consisting of a piezoceramic strip (PZT PIC-255, dimensions 40mm x 5mm x 1mm) and a steel backing mass (40mm x 5mm x 5mm) was constructed. Aluminium conductive tape was applied to both faces of the PZT strip so that the electrodes could be attached. The PZT strip and electrodes were then attached to the backing mass using double sided adhesive tape. Blu-tack was used as filling material at each end of the transducer to prevent short circuiting. The diagram in Figure 3-6b shows the transducer construction. As the line transducer needed to be repositioned to achieve different wave launching angles, it could not be bonded to the plate as described for the disc transducers. Instead, the transducer was mounted on the rear side of the plate and pushed onto the plate using a screw as shown in Figure 3-6a to obtain repeatable clamping pressure. The outer face of the transducer was wrapped in electrical tape to protect the PZT strip as a thin layer of set honey was used to improve coupling, increasing signal amplitude. The choice of set honey as a couplant is discussed further in section 3.5.

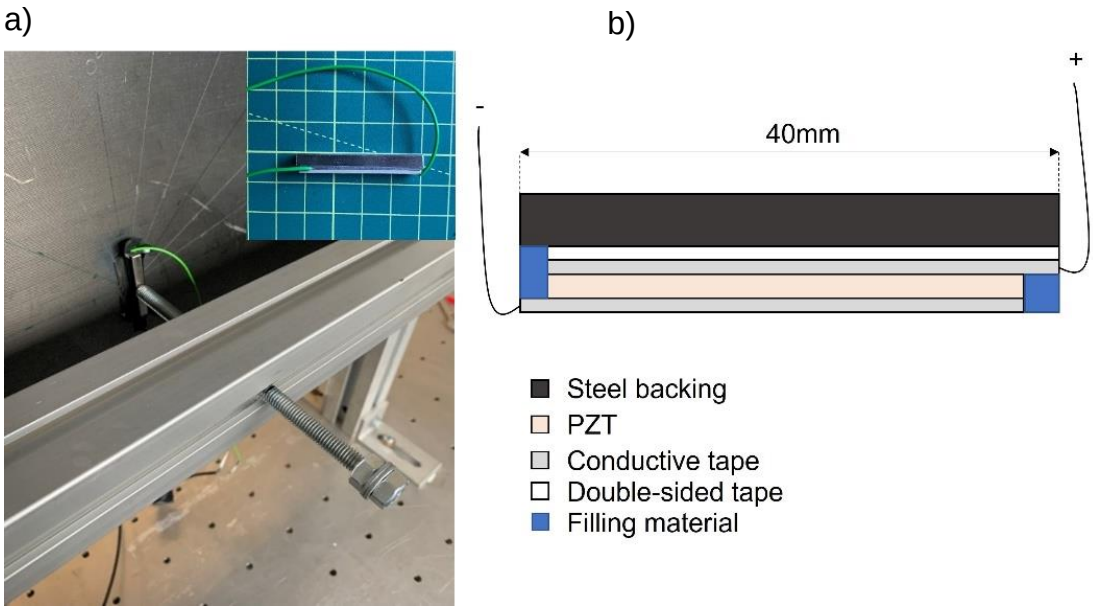

Figure 3-6 a) Photograph of line transducer (inset) and clamping mechanism on rear of plate; b) schematic of transducer construction.

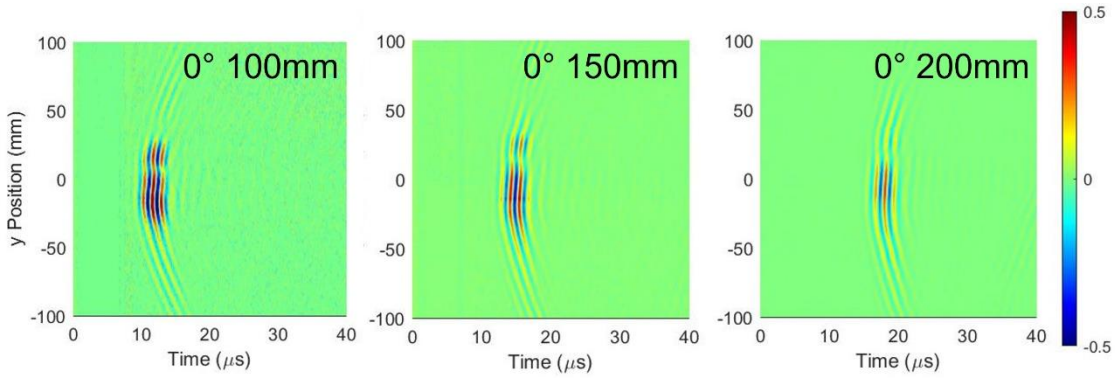

Figure 3-7 Wavefield produced by line transducer at 75kHz, directed along the 0° direction (fibre orientation) at 100mm, 150mm, and 200mm from the transducer location.

The wavefield produced by the line transducer propagating along the 0° direction is shown in Figure 3-7. An excitation frequency of 75kHz produced the most consistent wavefield, with the highest amplitude. In certain wave propagation directions at 75kHz, a region of destructive interference was observed at the centre of the line pulse. This is due to the wavelength of the A_0 mode at 75kHz being approximately half of the length of the transducer. Choosing a different excitation frequency such as 100kHz could mitigate this effect, however this resulted in a significant drop in amplitude, which made the A_0 mode difficult to detect in certain propagation directions. Hence a frequency of 75kHz was selected for measurements using the line transducer.

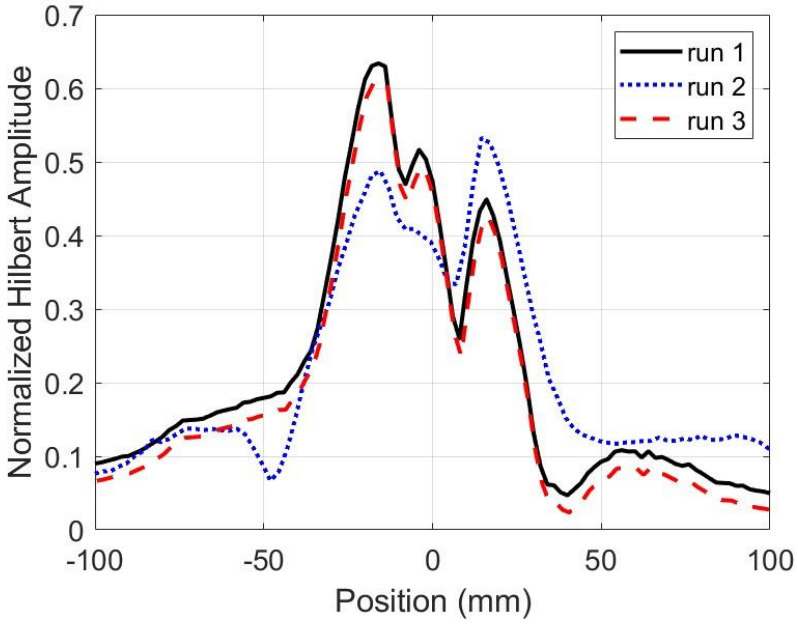

Figure 3-8 Hilbert amplitude along a line of points parallel to line, 100mm from source 75kHz excitation frequency.

The repeatability of the coupling of the line transducer was investigated by measuring along a line of points 100mm from the transducer (as for Figure 3-7a). The transducer was removed and repositioned before repeating the measurement. The normalized Hilbert amplitude at each measurement point was calculated and is presented in Figure 3-8, in order to visualise the energy distribution of the excitation. Each measurement shows a region of increased amplitude approximately -40mm to +40mm with a main peak between approximately -40mm to +5mm. A sharp drop in amplitude can be observed at approximately +5mm, where an additional peak occurs. After considering the wavefield directly on top of the transducer, it was found that this peak is likely due to waves being excited from the end of the transducer. The overall shape of the excitation is reasonably repeatable, although there is some variation in amplitude, particularly for run 2. This is likely due to slight variations in the thickness of honey couplant and variations in the clamping position and pressure which could not be fully eliminated.

There is in principle a possibility that higher (nonlinear) harmonics are generated. It has been demonstrated that only odd numbered higher harmonics (i.e., 3ω, 5ω) are typically generated for antisymmetric Lamb modes in isotropic plates [173]. For an excitation frequency of 75kHz a nonlinear harmonic could be generated at 225kHz (3ω). This is below the 250kHz cut-off frequency of the laser vibrometer, so in principle could be measured. However, the amplitude of this harmonic would typically be at least a factor of 10 times smaller than the fundamental harmonic [172]. The signal from the laser vibrometer is filtered with a 4^{th} order band-pass Butterworth filter with cut-off frequencies 50kHz-100kHz. This would reduce the amplitude of the third harmonic by an additional 20dB. Additionally, wave attenuation increases with frequency, further reducing the amplitude of the higher harmonic. Overall, this would result in the amplitude of the nonlinear component of the signal being 2-3 orders of magnitude lower than the fundamental harmonic wave signal, similar to the amplitude of the digitisation noise of the employed oscilloscope with 8-bit resolution. Finally, during analysis the FFT of the signal at the centre frequency of excitation (75kHz) was considered, further ensuring only the fundamental A_0 Lamb mode is being considered.

3.5 Permanent Magnet Target

Permanent magnets, mounted on both sides of a plate, provide a simple and practical way to simulate damage, as they are easy to remove and reposition on a structure [131]. In order to provide comparison to scattering measurements around the delamination in the quasi-isotropic plate, circular neodymium magnets (NeFeB type N42) with diameter 20mm and thickness 2mm were mounted on an undamaged region of the plate.

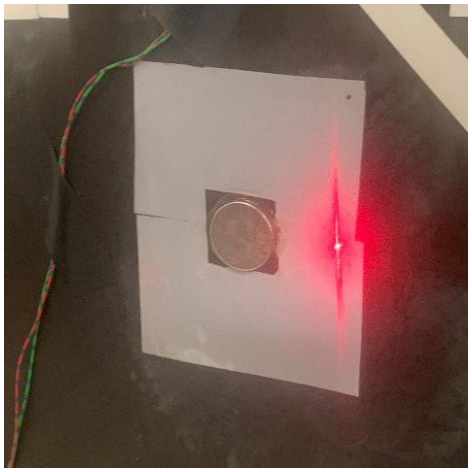

Figure 3-9 Photograph of permanent magnets mounted on CFRP panel.

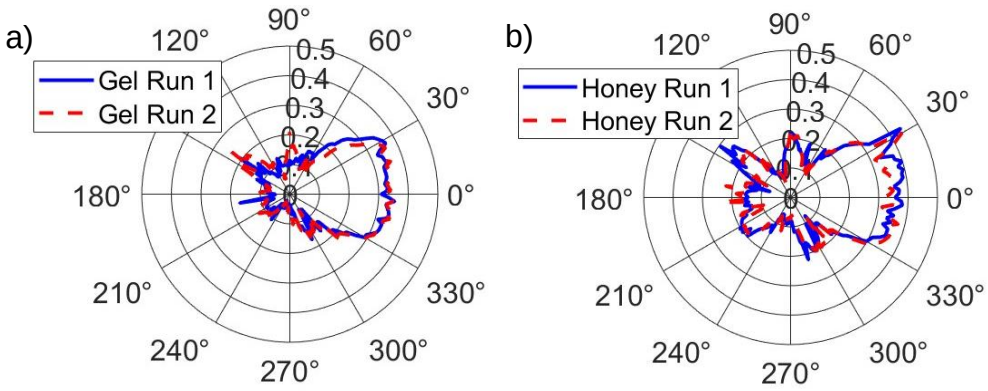

Figure 3-10 Isolated scattered wavefield at 50kHz (baseline subtraction) around circle of points (30mm radius) centred on permanent magnet using: a) gel couplant; b) set honey.

The magnet dimensions were chosen to approximately match the size of the delamination and are photographed in Figure 3-9. As seen in the photograph, reflective tape was removed from beneath the magnet to improve contact of magnet and plate surface. Initially the magnets were dry coupled to the plate, however limited scattering of the A_0 mode was observed. In order to improve the scattered signal amplitude two couplant types were investigated; ultrasonic

gel couplant and set honey. Set honey has been demonstrated to transmit both shear and longitudinal components of an ultrasonic pulse [152].

The A_0 mode signal was measured around a 30mm circle of points centred on the magnet location. A baseline measurement was performed with the magnets removed. A thin layer of couplant was applied to the magnet face before mounting and scanning. The magnets were removed, couplant reapplied and magnets were repositioned before re-scanning in order to determine the repeatability of the coupling. A Fast Fourier transform (FFT) was performed on the time signals from each measurement point and a baseline subtraction analysis was performed. More details of the baseline subtraction analysis are discussed in section 6.3. The scattered wave around the permanent magnet for each couplant type is shown in Figure 3-10. Measurements were repeatable for each couplant type. The honey produced a slightly higher scattered amplitude in both the forward and back-scattered directions. The structure of back and sideways scattered lobes is visible for the honey couplant, whereas they are not observed for the gel couplant. Therefore, set honey couplant was selected to couple magnets and the line transducer described in section 3.4 to the plate.

3.6 Summary and Conclusions

This chapter introduced the experimental techniques used in this thesis. The investigated composite specimens have been described in addition to the scanning laser Doppler vibrometer setup. Disc transducers used to generate a point excitation of the A_0 mode were described. A line transducer has been developed to perform the wave skew measurements and found to operate best at an excitation frequency of 75kHz. Repeatable measurements could be obtained from the line transducer. Permanent magnets can be used to simulate damage. The use of gel and set honey couplant on scattered A_0 mode amplitudes were investigated. Repeatable measurements could be obtained from each couplant, however set honey yielded the highest scattered amplitude. Hence set honey was chosen for subsequent measurements in this thesis. The details and results of the measurements described in this chapter are presented in Chapters 5 and 6.

4 Finite Element Modelling

This chapter describes the 3D Finite Element (FE) modelling techniques used to simulate propagation and scattering of the A_0 guided wave mode in CFRP plates. A method for generating Abaqus input files is presented and the computational stability criteria for FE modelling are discussed. Details of the homogenised plate model, used to simulate wave propagation in the undamaged unidirectional CFRP laminate, are given. Then a layered plate model, used for the quasi-isotropic laminate, is presented. Details of how delamination and bonded mass damage are incorporated into the layered model are explained. Specific measurement and excitation geometries will be discussed in the relevant results chapters.

4.1 Explicit Finite Element Analysis

Guided wave propagation problems can be modelled using the Finite Element (FE) method. This involves discretizing a structure into small elements with fixed time integration points known as nodes. Wave propagation occurs as a result of applying a load to the nodes, disturbing the initial equilibrium, and displacing the elements [153]. Integrating the acceleration of the elements twice, the displacements can then be calculated. There are two main schemes which can be used to solve time domain FE problems: implicit and explicit. Both schemes are available in the commercial finite element package Abaqus, which was used to model wave propagation in this thesis. The implicit scheme establishes global equilibrium at each time increment. Then the solver calculates local variables (e.g., stress, displacement) on each of the elements for that time increment. This scheme allows for the use of large time increments, however each increment computes slowly due to the multiple iterations required to converge on a global equilibrium. On the other hand, the explicit scheme calculates all of the local variables for a given time increment, then moves onto the next increment using the values acquired at the previous time step. This allows for faster calculation of each time increment but requires a small increment size [154]. This makes the explicit scheme well suited for frequency domain simulations which occur over short time scales.

The aim of finite element analysis is to solve the equation of motion for each of the nodes and elements. The equation of motion can be defined as:

$$\hat{f}(t) = M\ddot{u} + C\,\dot{u} + Ku, \tag{4.1}$$

where $\hat{f}(t)$ is force, M is the mass matrix, C is the damping matrix and K is the stiffness matrix. Displacements, velocity and acceleration are represented by $u, \dot{u}$ and $\ddot{u}$ respectively.

In the explicit time integration method, the acceleration on each node $\ddot{u}$ must first be calculated at the current time increment i. The equation of motion can be written in the following way:

$$\ddot{u}^{(i)} = \frac{F^{(i)} - I^{(i)}}{M}\ , \tag{4.2}$$

where M is now the diagonal or "lumped" mass matrix. The sum of external nodal forces F are calculated from the boundary conditions, loadings, and constraints of the problem. The sum of internal nodal forces, I, are calculated from the strain rates, strains and stresses, which can be obtained from the material properties and initial conditions of the mesh. Equation 4.2 is then integrated twice using a central finite difference scheme to obtain displacements at the next time increment $(i + 1)$ as follows:

$$\dot{u}^{(i+1/2)} = \dot{\mathrm{u}}^{(i-1/2)} + \frac{\Delta t^{(i+1)} + \Delta t^{(i)}}{2}\ddot{u}^{(i)}\ , \tag{4.3}$$

$$u^{(i+1)} = u^{(i)} + \Delta t^{(i+1)}\dot{u}^{(i+1/2)}, \tag{4.4}$$

where Δt is the time increment and the indices $(i + 1/2)$ and $(i - 1/2)$ represent midincrement values. Once the displacements (Equation 4.4) have been calculated the strains can be calculated at time increment $(i + 1)$. Subsequently, stresses at time increment $(i + 1)$ are calculated and transformed back to nodal forces. Acceleration at the next time increment can then be obtained and the algorithm repeats [154].

4.2 Generating Model Input Files

A FE model can be created in Abaqus using the graphical user interface (Abaqus\CAE), however this can be time consuming when many, minor parameter changes are required. In addition, obtaining exact locations for node output and generating a regular mesh can also be difficult using the CAE. Instead, a programmable input file can be generated from MATLAB, and can then be imported into Abaqus\Explicit so that the analysis can be performed. The input file defines all of the parameters required to generate the FE model, such as the plate geometry, mesh, material properties, monitoring points, excitation signal, and anisotropy orientation of ply layers in addition to the time increment used for explicit analysis. The MATLAB program is based on a script originally written by Robert Watson [155] for wave propagation in isotropic plates and was modified for composite plates by Bibi Murat [156]. The program has been further modified for the present study to model the specimens introduced in Chapter 3.

A regular mesh is particularly advantageous for wave propagation simulations as it has been shown to reduce numerical dispersion [157] and is easier to implement than an adaptive mesh [153]. Identical meshes for both damage and baseline simulations were also required for baseline subtraction analysis (further discussed in section 6.3). A regular structured mesh has the advantage that numerical dispersion is uniform across the whole model. Irregular, adaptive meshes can be more computationally efficient, as the mesh can be refined in the necessary regions and can more accurately represent the edges of damage. However, this has the disadvantage of variable numerical dispersion, which can result in unwanted wave scattering from the mesh itself. To mitigate unwanted scattering effects when modelling wave propagation using an irregular mesh, it has been shown that for modelling wave propagation, a finer mesh is required than if a regular mesh was selected [158].

In order to generate a regular, Cartesian mesh, the program requires the dimensions of the plate and the element dimensions to be defined. These parameters are used to calculate the number of elements and nodes in the model. The borders of the plate are defined first using corner nodes cn_i. These

nodes are connected to form plate edges and node numbers are assigned. The nodes and node numbers along the top and bottom faces of the plate are then defined as a part. The nodes have a regular numbering scheme, so it is easy to automatically calculate the node numbers for excitation and monitoring locations from Cartesian coordinates. A master element is created by connecting eight nodes at the corner of the plate and assigning node numbers, which also requires a regular numbering scheme. In the case of the layered plate model described in section 4.4, each layer is defined as a separate part with its own master element. The parts are then meshed by connecting the rest of the nodes to form elements. Material properties are then assigned to each part of the model. An illustration of the model geometry is presented in Figure 4-1. The A_0 mode is generated by applying an out-of-plane concentrated force in the centre of the thickness of the plate (with symmetrical layup) as shown in Figure 4-1. This is to avoid generating the in-plane S_0 mode, whose mode shape has no out-of-plane component at the mid-plane. The excitation signal was a 5-cycle sine wave modulated by a Hanning window, as defined for the experimental measurements in section 3.3. Monitoring points were defined on the surface of the plate and history

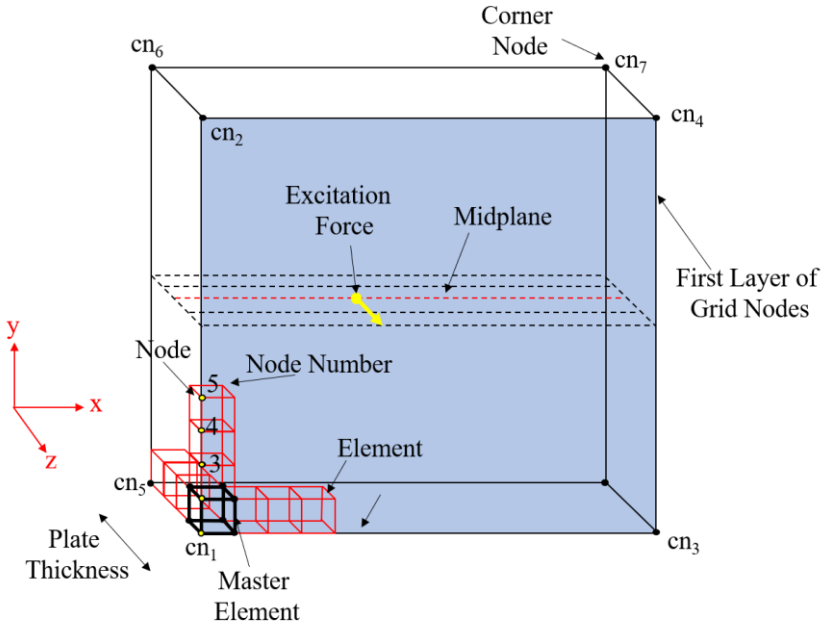

Figure 4-1 Illustration of the plate geometry of the FE model. Corner nodes are indicated, in addition to the first few grid nodes numbered 1-5. The master element is indicated as the black cube, and the first few elements are represented by red cubes. Excitation and monitoring nodes can be positioned as required.

outputs for the out-of-plane displacement were requested for each point. Model parameters specific to individual simulations such as the time increment, element size, excitation frequency, and simulation run time will be described in the relevant sections.

4.3 Stability Criteria

The commercial software Abaqus/Explicit was used to model guided wave problems using the Finite Element method. As discussed in section 4.2, the explicit method involves integrating the equations of motion explicitly through time, using the kinematic conditions at one time increment to calculate the kinematic conditions at the next [154]. The size of the time increment Δt_{inc} must be chosen carefully to avoid numerical instability and unbounded solutions. In order to meet the computational stability criteria, Δt_{inc} must be smaller than the critical time increment, Δt_c. When modelling wave propagation, Δt_c is defined as the transit time at the fastest wave speed, c_{max} through the length of the smallest element in the model, l_{min}. This is described by equation 4.5.

$$\Delta t_{inc} \leq \Delta t_c = \frac{l_{min}}{c_{max}} \tag{4.5}$$

$$l_{min} \leq \frac{\lambda_{min}}{10} \tag{4.6}$$

To generate an accurate solution, a general rule of thumb is that the smallest element size must allow for at least 10 elements per the shortest wavelength propagating in a plate [159]. For explicit finite element analysis it has been demonstrated that at least 20 elements per wavelength is required to achieve a dispersive error less than 1% [160]. Several studies have employed much finer meshes up to 50 elements per wavelength [98], which has been shown to reduce numerical dispersion [157]. Equation 4.6 describes this criterion. A sufficient number of elements through the thickness of the plate are required to capture the mode shapes of propagating wave modes at low frequencies as illustrated schematically in Figure 4-2. The greater the number of elements through the thickness, the better the approximation of the mode shape, however this can significantly increase the number of elements in the model and hence increase computation time.

The element type chosen for the FE mesh is also an important consideration. An 8-node linear brick element with reduced integration (C3D8R) was initially selected as it provides a regular Cartesian mesh throughout a plate structure and has been widely used to model guided wave propagation in composite laminates [107,113,120]. For bending problems of thin structures, such as wave propagation of the A_0 mode in a thin composite laminate, C3D8 elements can be prone to "locking", which results in an unphysically stiff mesh, reducing the accuracy of simulations. This is because the element may not be able to accurately approximate strain distributions associated with bending in thin structures [161]. A reduced integration element such as C3D8R can be used instead to prevent locking and model bending more accurately. C3D8R elements have fewer integration points than C3D8, resulting in faster computation time. These two element types are compared in section 6.5.

The stability criteria discussed so far can lead to a plate model with a large number of elements which could take a long time to solve. One way to deal with this would be to model a 2D structure, this would not provide a solution representative of a real specimen. Another solution would be to reduce the size of the model by modelling a plate section. The model would still need to be large enough to separate unwanted signals such as edge reflections. Alternatively, absorbing boundary conditions could be imposed on the plate edges [90]. The dimensions of the unidirectional plate model, and delaminated plate model will be discussed in the following sections.

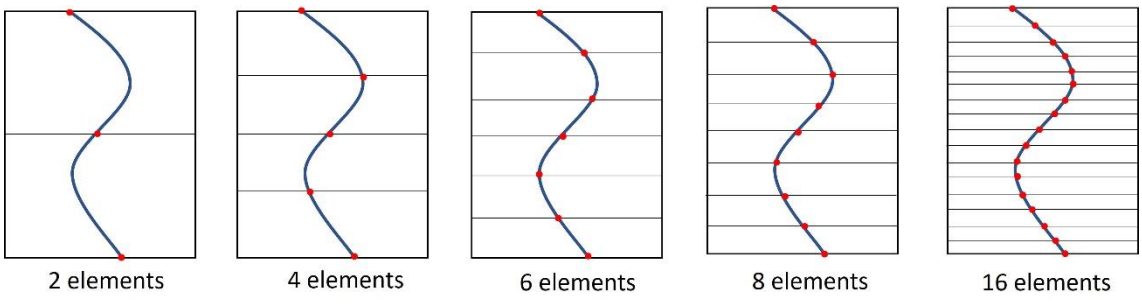

Figure 4-2 Schematic demonstrating interpolation of guided wave mode shapes with increasing number of elements through the plate thickness. Mode shape is exaggerated.

4.4 Homogenised Plate Model

The undamaged unidirectional plate (section 3.1) was modelled as a single layered solid homogenous structure. The fibres of all ply layers are aligned along the same orientation and so modelling of individual ply layers is not required. A 600mm x 400mm plate section with 3.6mm thickness was modelled with elements size 0.5mm x 0.5mm x 0.45mm to give eight elements through the plate thickness. This model size was chosen as it was large enough to time separate unwanted edge reflections, without requiring the whole large plate to be modelled. Homogenised orthotropic material properties (Table 3-1) were assigned to the plate assembly. Abaqus also requires the orientation of anisotropic material properties to be defined. Initially this was set so that the measurement points were oriented along the 0° (fibre) direction. The definition of the material properties was then altered to rotate the material orientation and achieve wave propagation along different directions. Stiffness proportional Rayleigh damping was incorporated into the model to simulate the wave attenuation typically present in composites. The stiffness proportional damping coefficient was set to 70ns. The rationale for this choice is discussed in detail in section 5.2. The stable time increment was Δt_{inc}=5ns and the simulation time was 0.3ms. The homogenised model took approximately 40 minutes to run on 32 CPUs of a shared memory Linux computer.

The model parameters (element size, no. of elements through thickness, stable time increment) were determined by performing mesh refinement studies, where each parameter was varied in turn and the phase velocity of the A_0 mode was calculated for each case. The method of phase velocity calculation is described in section 5.4.1. A time increment of 5ns was selected based on the results presented in Table 4-1. Smaller time increments gave phase velocity values within 0.1% of each other. Table 4-2 shows phase velocities when the in-plane element size is varied. For elements 1mm or smaller the phase velocities agree within 0.1%. The number of elements through the thickness of the plate was also varied and the corresponding phase velocity values are shown in table Table 4-3 . It can be seen that at least 4 elements through the thickness are required for the phase velocity values to converge. As discussed above an element size of 0.5mm x 0.5mm x 0.45mm was selected to model the

undamaged unidirectional plate. 8 elements were modelled through the thickness as the mode shapes of propagating waves are captured more accurately than for the minimum 4 elements (Figure 4-2). An in-plane element size of 0.5mm is sufficiently small for convergence and is similar to the through thickness element size. The chosen parameters ensure the numerical accuracy of the model is within 1%.

Table 4-1 Phase velocity sensitivity with changing time increment.

In-plane element size (mm)	Element thickness (mm)	No. elements through plate thickness	Time increment (ns)	Phase velocity in fibre direction (ms^{-1})
0.5	0.45	8	50	n/a (unstable)
0.5	0.45	8	10	1327
0.5	0.45	8	5	1338
0.5	0.45	8	1	1337

Table 4-2 Phase velocity sensitivity with in-plane mesh density.

In-plane element size (mm)	Element thickness (mm)	No. elements through plate thickness	Time increment (ns)	Phase velocity in fibre direction (ms^{-1})
2	0.45	8	5	1327
1	0.45	8	5	1336
0.75	0.45	8	5	1337
0.5	0.45	8	5	1337
0.4	0.45	8	5	1338
0.3	0.45	8	5	1338

Table 4-3 Phase velocity sensitivity with through thickness mesh density.

In-plane element size (mm)	Element thickness (mm)	No. elements through plate thickness	Time increment (ns)	Phase velocity in fibre direction (ms^{-1})
0.5	1.8	2	5	1358
0.5	0.9	4	5	1337
0.5	0.6	6	5	1338
0.5	0.45	8	5	1337
0.5	0.36	10	5	1338
0.5	0.3	12	5	1339

4.5 Layered Plate Model

For the 8-ply quasi-isotropic laminate a different modelling strategy is required. Each ply layer was modelled as a single unidirectional layer of elements, initially with one element through the thickness (0.2mm). Two elements through the thickness of a single ply layer were also investigated, as this would enable the mode shape through a single ply layer to be captured more effectively (e.g., for shallow delaminations), but increases the computational time of the model significantly. This is discussed further in section 6.5. The homogeneous material properties given in Table 3-2 were assigned to each layer individually and the orientation of each layer was defined to produce the stacking sequence ($[-45/45/0/90]_s$) to match the physical specimen described in section 3.2. The in-plane element dimensions were initially set to 0.5mm x 0.5mm, which gave 20 elements per wavelength in an undamaged plate at 50kHz. The stable time increment was Δt_{inc}=5ns and the simulation time was 0.3ms. The (Rayleigh) damping coefficient was set to β=30ns. The rationale for this choice is described in section 6.4. Two damage types were modelled, a zero-volume delamination and a bonded mass. Simulations for both an undamaged and damaged full size (600mm x 600mm x 1.6mm) plate took approximately 4 hours to run on 32 CPUs of a shared memory Linux computer.

A zero-volume delamination was incorporated into the model by overwriting existing elements at the delamination location, as shown schematically in Figure 4-3. New nodes and elements, connected to one side of the plate, were defined over a square area with the approximate dimensions of the desired

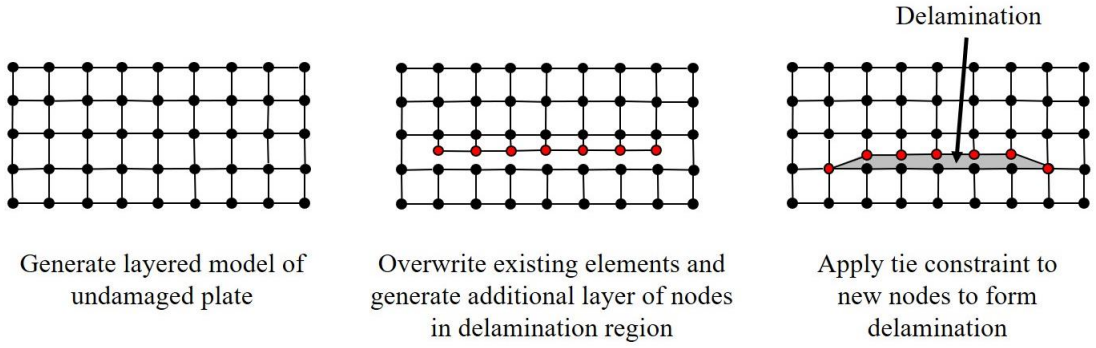

Figure 4-3 Schematic of procedure to model zero volume delamination. Through thickness view of mesh surrounding delamination region at different steps. Red nodes represent new nodes generated in the delamination area. Volume of delamination is exaggerated.

delamination size. The element and node numbers of the overwritten elements remain the same, and new nodes share the same coordinate values as the existing nodes they are connected to. A node set was defined in the region opposite the new nodes to form the shape to the delamination. A circular shape was defined on the grid using a bilinear interpolation. A node-to-node tie constraint was applied to the circular node set and the square area of new nodes as shown in Figure 4-4. In Abaqus\explicit, tie constraints can be used to fuse two surfaces together. A node-to-node tie constraint connects two node sets together resulting in each pair of tied nodes essentially acting as a single node.

This procedure was also used to discretize an ellipse shaped delamination by defining a rectangular area of new nodes with dimensions of the major and minor axis of the ellipse. This approach provides an identical geometry to the more standard approach of two distinct regions with tie constraints [162], while allowing for straightforward automated generation of circular or ellipse shaped delaminations using the MATLAB code. It should be noted that there is no mesh refinement at the delamination edges and so localized stress concentrations may not be captured in this region. However, as the length scale these stress concentrations occur over is significantly shorter than the wavelength at this frequency this is less likely to impact the accuracy of the model. Additionally, as seen from the C-scan of the delaminated specimen, the exact delamination

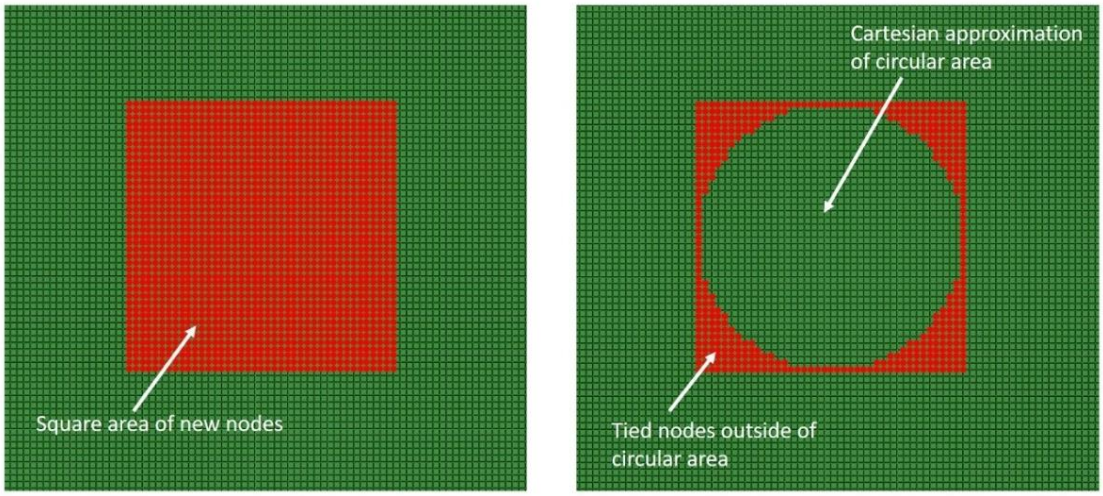

Figure 4-4 Close up top view of delamination region in Abaqus: a) new nodes created in delamination region; b) tied nodes to form circular delamination area.

shape is unknown, which may affect the accuracy of the model. For SHM, the propagation of scattered waves in the regions surrounding the damage is of more interest than wave propagation in the near field of the damage region. It will be demonstrated in Chapter 6 that this mesh is sufficient to accurately model wave propagation of the scattered waves propagating away from the damaged region. A 20mm x 20mm circular delamination was initially modelled and used as the standard case throughout this thesis.

The baseline plate model (no delamination) was modified to incorporate permanent magnets and is illustrated in Figure 4-5. Initially, an additional set of nodes was defined in a circular region (diameter 20mm) on the front and rear faces of the plate. The model was then imported into Abaqus CAE to model magnets mounted on the plate. Two cylindrical parts (diameter 20mm, thickness 2mm) were defined. A node-to-surface tie constraint was defined between the circular node sets on the plate and the magnet surface, as illustrated in Figure 4-5a, ensuring no relative motion between the plate and the magnet. In Abaqus tie constraints require rotational degrees of freedom at the nodes as a default. However this is incompatible with the C3D8R element type that only has translational degrees of freedom. Therefore, the rotational degrees of freedom at the tie constraint had to be restricted for the analysis to run correctly. Nominal material properties of NeFeB were assigned to the magnet parts as given in Table 4-4. History outputs were defined on the plate surface over a 60mm x 60mm grid of measurement points in 1mm steps, centered on the delamination damage and magnet respectively. A 40mm x 40mm grid, bilinear interpolation onto a 30mm circle, and horizontal and vertical lines can be selected from this data during analysis for comparison to the experiments.

Table 4-4 Material properties of NeFeB magnets, type N42.

Property	Value
ρ	7500 kgm^{-3}
E	160 GPa
v	0.24

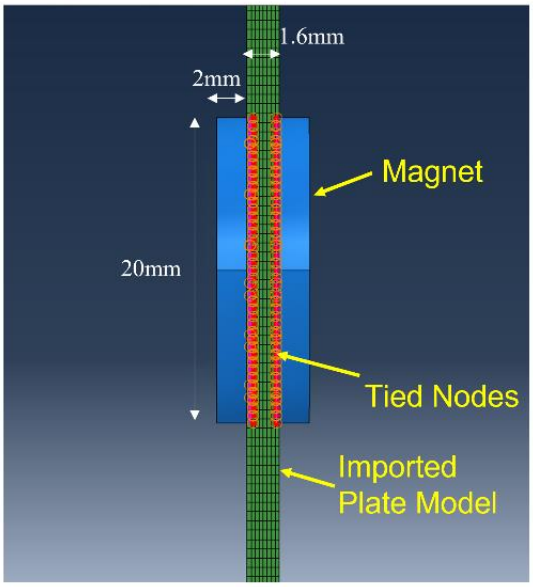

Figure 4-5 a) cross section view of the plate with magnets and tied nodes highlighted.

4.6 Summary

The FE modelling techniques used throughout this thesis have been described in this chapter. The procedure for generating model input files has been introduced. Model stability criteria were discussed, and details of the homogenised and layered plate models were presented. A zero-volume delamination, and a bonded mass (permanent magnet) damage were incorporated into the layered model. The results of the numerical simulations are described in Chapters 5 and 6.

5 Anisotropic Guided Wave Propagation Effects in a Unidirectional Composite Laminate

Wave propagation of the A_0 guided wave mode in an undamaged unidirectional CFRP laminate (section 3.1) is investigated in this Chapter. Anisotropic wave propagation effects such as directionally dependent wave velocities, wave skewing, and beam spreading due to the high material anisotropy of the unidirectional laminate are measured and quantified. Firstly, experimental and FE model geometries specific to this investigation are presented, building on the general information discussed in Chapters 3 and 4. Determination of the Rayleigh damping coefficient is discussed before looking at the anisotropic wave propagation effects in turn. Phase and group velocities are investigated in multiple directions for a range of point and line sources. The effect of source type on wave velocity is investigated. Wave skew angles are investigated experimentally for multiple incident wave directions using a repositionable line transducer, in contrast to previous studies that have used a fixed transducer in a single wave propagation direction [48,74]. Unlike in previous studies of wave skew angles in CFRP, FE simulation of wave skew and beam spreading behaviour is performed. Beam spreading is quantitatively investigated and compared to the theoretical anisotropy factor. This chapter incorporates work from two publications [147, 148].

5.1 Experimental and FE Model Geometry

Guided wave measurements were performed on the undamaged unidirectional specimen (1.14m x 0.94m x 3.6mm, corners removed) described in section 3.1 and shown in Figure 5-1. A point source excitation was produced by a disc transducer with brass backing mass (section 3.4) at an excitation frequency of 75kHz. This frequency was selected to match the best operating frequency of the line transducer. The excitation signal was amplified to 200Vpp before being applied to the transducer. This gave the most stable wave pulse at the highest amplitude for this excitation frequency. To measure the directionality of phase and group velocity, radial line scans were performed every 15° as shown

schematically in Figure 5-1b. Each scan line was 100mm long, originated 100mm from the transducer and was scanned in 1mm steps.

Guided wave skew angles were measured using the 40mm line transducer. The same excitation signal and frequency was used as for the disc transducer, however the signal was amplified to 75Vpp before being applied to the line transducer. A lower amplification value was required in order to avoid the signal clipping at this frequency. The line transducer was oriented in 15° increments and 5 line scans, parallel to the line transducer, perpendicular to the wave launching direction were scanned using the LDV as shown schematically in Figure 5-1b. The line scans were located 100mm, 125mm, 150mm, 175mm and 200mm from the transducer and scanned in 2mm steps.

The FE model geometry of a plate section with dimensions 600mm x 400mm x 3.6mm are shown schematically in Figure 5-2. Excitation and monitoring locations to match the velocity measurements on the physical specimen are shown in Figure 5-2a. A point excitation was modelled by applying an out-of-plane force to a single node, whereas line excitations 40mm and 80mm in length were excited by applying the force simultaneously to a line of nodes.

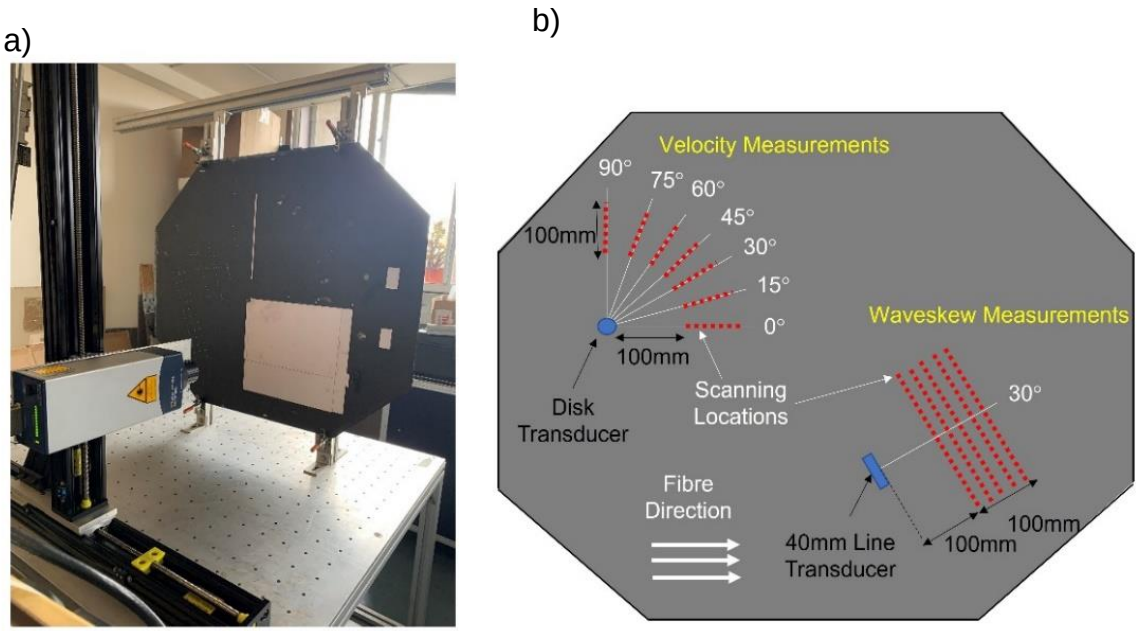

Figure 5-1 a) Photograph of CFRP specimen and experimental setup; b) schematic of scanning patterns for velocity measurements and wavefield measurements on CFRP specimen.

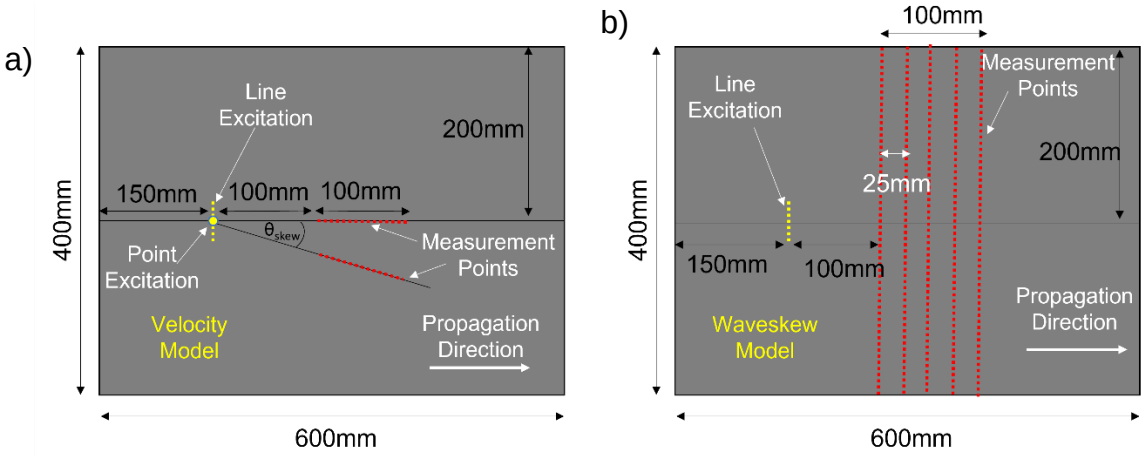

Figure 5-2 Geometry of FE model. Schematic shows excitation and measurement locations for a) velocity simulations; b) wave skew simulations.

As the distance between nodes (0.5mm) was significantly shorter than the A_0 mode wavelength ($\lambda \approx 16 - 22$mm), the line of points formed a reasonably uniform line source. The results from the line of nodes were compared to the excitation produced when forces were applied to all nodes withing a rectangular area with the approximate dimensions of the PZT strip from the line transducer (40mm x 5mm), however velocity values from each source matched within 1% so the line of nodes excitation was selected for subsequent simulations. The line source lengths 40mm and 80mm were chosen to be significantly longer than the wavelength of the A_0 mode in all propagation directions.

To achieve different wave launching directions, the definition of the orientation of the material properties was varied in 5° increments between 0° and 90°, whilst keeping the model geometry the same. A separate simulation was performed for each excitation type in each wave launching direction. Additionally, a diagonal line of measurement points, oriented along the skew angle of the corresponding wave launching direction was defined for the wave skew velocity correction which is discussed further in section 5.4.4. A 40mm line source was selected for the wave skew angle simulations, shown schematically in Figure 5-2b to match the length of the PZT strip used for the line transducer. Five parallel lines of measurement points spanning the full width of the plate were defined between 100mm and 200mm from the source to match experimental measurements. A separate simulation was again performed for each wave launching direction.

5.2 Modelling Guided Wave Attenuation

As discussed in section 3.1, the material properties of a composite laminate can be described by the stiffness matrix, which for an orthotropic material contains nine complex stiffness coefficients, C_{ij}. The imaginary part of each coefficient is related to the attenuation of the material and can be used to predict the attenuation in different directions across a range of frequencies [163]. Although the complex coefficients had been measured previously at a frequency of 2MHz for the unidirectional plate [61], it is not possible to define imaginary stiffness properties in Abaqus/Explicit. Rayleigh damping, on the other hand, is available in Abaqus/Explicit and has been used in several studies to model guided wave attenuation in composite laminates [95,113,164]. This section details the procedure for determining attenuation coefficients in the unidirectional plate.

The amplitude $U(x)$ of Lamb waves generated from a point source in a viscoelastic medium decay with propagation distance x according to the following equation [164]:

$$U(x) = \frac{U_0}{\sqrt{x}} e^{-\eta x} \ , \tag{5.1}$$

where A_0 is the initial amplitude at the excitation location and η is the attenuation coefficient. The factor $1/\sqrt{x}$ accounts for the geometric spreading of the wave pulse with distance, whereas the exponential term represents the decay in amplitude due to wave attenuation. The attenuation coefficient is related to the Rayleigh damping coefficients α (mass proportional), and β (stiffness proportional) as follows [164]:

$$\eta = \frac{1}{2c_g}(\alpha + \beta\omega^2), \tag{5.2}$$

where c_g is the group velocity of the A_0 mode and ω is the angular frequency $(\omega = 2\pi f)$. In previous studies only stiffness proportional damping ($\beta \neq 0$, $\alpha = 0$), which is proportional to the strain rate elastic material stiffness is considered. This is because the β term in equation 5.2 is frequency dependent, as is the attenuation of guided waves. In this study only stiffness proportional damping is incorporated into the model. Equation 5.2 then simplifies to

$$\eta = \frac{\beta\omega^2}{2c_g} . \quad (5.3)$$

The factor of $1/\sqrt{x}$ in equation 5.1 has a singularity at x=0. An additional offset *b* was introduced to correct for this as follows:

$$U(x) = \frac{U_0}{\sqrt{x-b}} e^{-\eta(x-b)} . \quad (5.4)$$

A least-squares fit of the equation 5.4 can be performed on the experimental and simulated amplitude data. The amplitude coefficient η can be extracted, and the β value calculated from the following equation:

$$\beta = \frac{2\,\eta\,c_g}{(2\pi f)^2} \quad (5.5)$$

Using a β value calculated from the method above has some limitations. Equation 5.1 technically is used to describe isotropic materials. In materials such as composites higher wave attenuation occurs in certain directions due to anisotropy. To mitigate this effect, when selecting a β value, the amplitude curves for multiple wave propagation directions were considered. When incorporating Rayleigh damping into the FE model, a smaller time step is required in order for the simulation to be stable, which results in increased computation time.

In order to validate the fitting procedure, a FE model containing no damping (β=0ns) and a 200mm line of measurement points originating 10mm from the source was performed for each of the 0°, 45°, 90° directions. The maximum amplitude of the Hilbert envelope was calculated for each measurement point. Equation 5.4 was fitted to the amplitude curves and the coefficient β was extracted. To avoid near field effects only points beyond 50mm (approx. twice the A_0 mode wavelength at 75kHz) from the source were considered in the fitting. The β=0ns amplitude curves are denoted by the black lines in Figure 5-3, and the β coefficients obtained from the fitting are shown in Table 5-1. The coefficient of determination (R^2) was calculated to evaluate the goodness of fit. R^2 can take values between 0-1 with 1 being the best possible fit. A good fit ($R^2 > 0.99$) is observed for each wave propagation direction. The coefficients in

each of the propagation directions are within 2ns of the expected value of indicating that the fitting procedure is appropriate.

To estimate the attenuation in the physical specimen, the point transducer was excited at 75kHz and a 200mm line of measurement points, originating 10mm from the source was scanned in 1mm steps for each of the 0°, 45°, and 90° directions. Equation 5.5 was fitted to each amplitude curve and the coefficient β was extracted. The measured amplitude curves are shown in red in Figure 5-3 and the β values obtained from the fitted curves are shown in Table 5-1. In the 0° direction beyond a propagation distance of 160mm interference effects occurred in this region of the plate, hence these points were omitted when fitting the data. The measured values in Table 5-1 show significant variability between the different incident wave direction and so β cannot directly be determined from the experiments. Therefore, simulations were performed with β values between 60ns-90ns in order to determine a best estimate of the damping in the plate. A value of β=70ns, denoted by the blue curves in Figure 5-3, visually gave the best match with the measured amplitude curves in the different directions. The β values from the fitted β=70ns FE data in Table 5-1 are within 5ns of the expected value. Comparing these values to the experimental results, reasonable agreement (within 5ns) can be seen between the experimental and β=70ns results in the 0° direction. However, there is a much larger variation between the 45° and 90° experimental and FE values. This could potentially be the result of the very low amplitudes measured in these directions, as a result of anisotropy or as a result of the accuracy of the FEM.

Attenuation values as a function of frequency in the 0° direction were calculated using the complex stiffness coefficients (Table 3-1) using Disperse. The attenuation at 75kHz in the 0° direction was calculated to be η=62dB/m in disperse, whereas the estimated attenuation from the experimental and 70ns FE amplitudes were both η=47 dB/m. This discrepancy could be due to the fact that the imaginary components were measured at a different frequency range (2MHz) compared to the frequencies considered here. In principle, attenuation varies linearly with frequency, however the material anisotropy, and the

resulting wave propagation effects may result in different attenuation behavior. Additionally, experimental error of the imaginary stiffness coefficients is large, which may also impact the accuracy of the attenuation values. As a Rayleigh damping coefficient of β=70ns gave reasonable agreement between experimental and FE values, and amplitudes matched visually, this value was selected for the subsequent simulations of the unidirectional plate.

Table 5-1 Beta values obtained from fitting amplitude curves.

Direction	β Experiment	β FEA 0ns	β FEA 70ns
0°	65ns	-2ns	65ns
45°	80ns	0.7ns	75ns
90°	90ns	-1.5ns	70ns

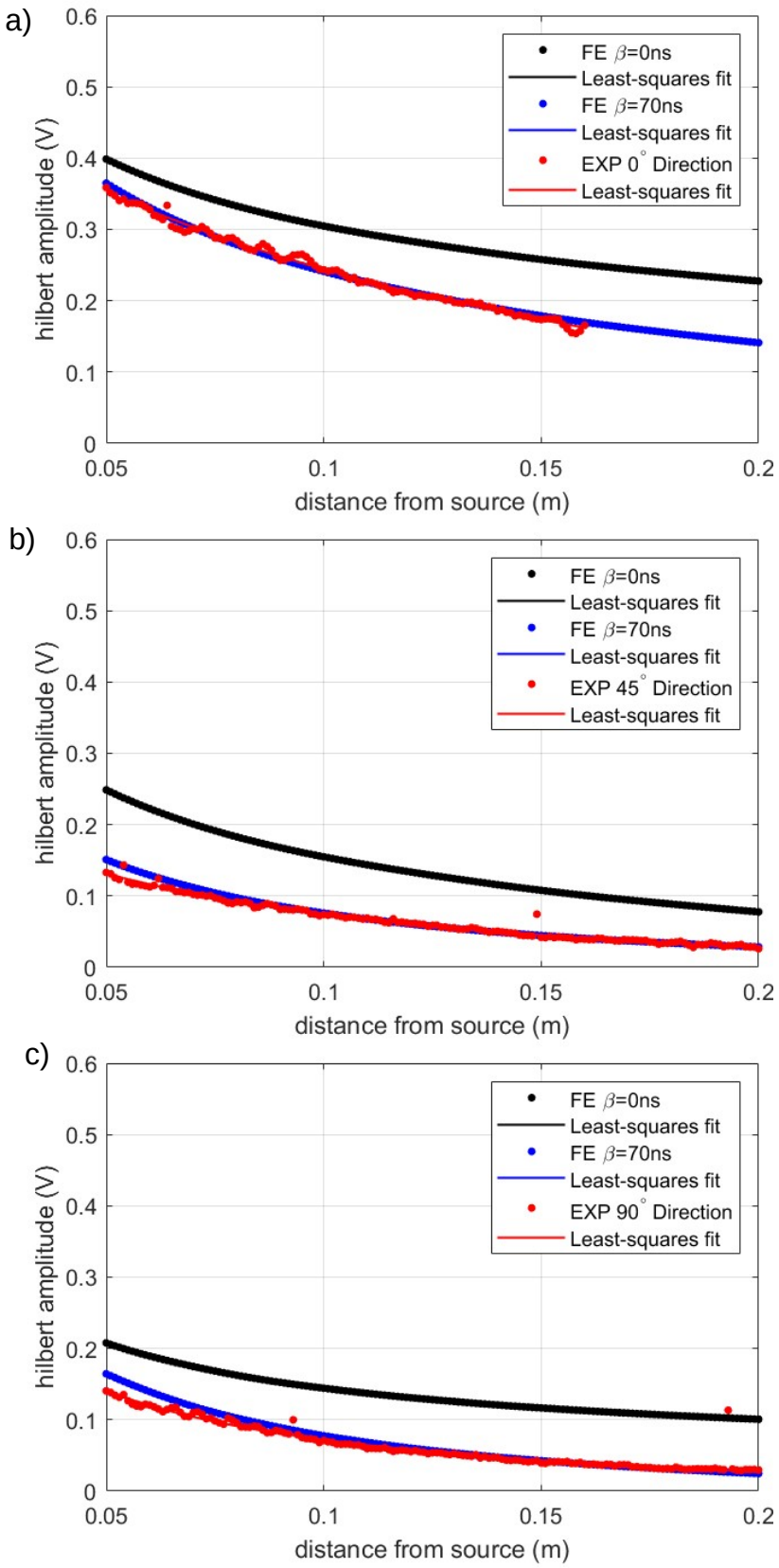

Figure 5-3 Fitted amplitude curves of the A_0 mode at 75kHz in a unidirectional plate for a) 0°; b) 45°; c) 90° directions. Experimental amplitudes (red) are compared to FE amplitudes with stiffness proportional Rayleigh damping of β=0ns (black) and β=70ns (blue)

5.3 Wave Skew Angles from Dispersion Curves

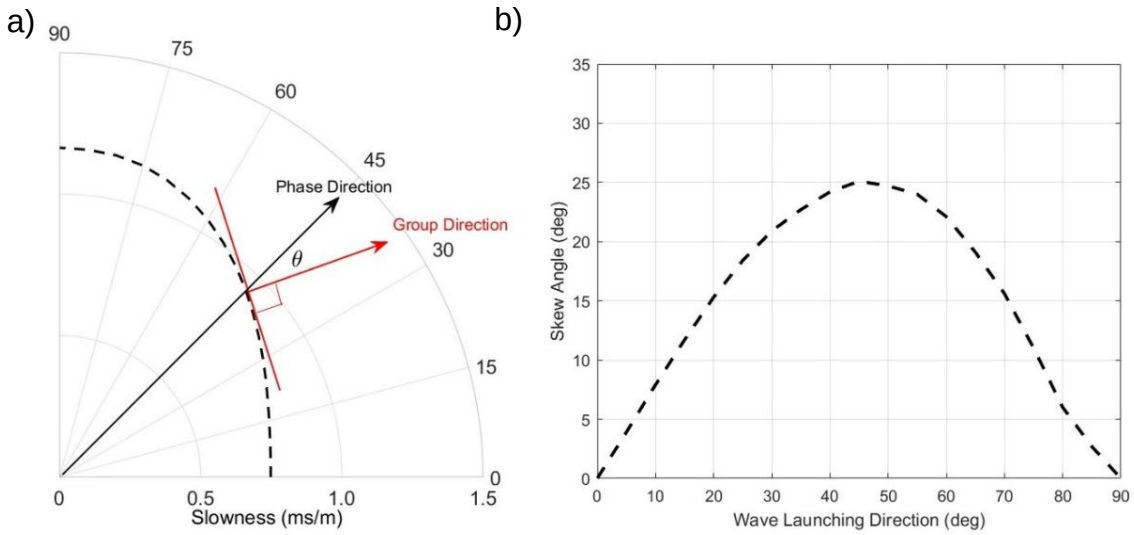

Figure 5-4 a) Phase slowness curve for 3.6mm thick CFRP at 75kHz, calculated from dispersion curves generated in Disperse [44]. Phase direction denoted by black arrow; group direction denoted by red arrow. Skew angle θ is difference between the phase and group direction; b) variation in theoretical skew angle with phase direction.

Phase and group velocity dispersion curves were obtained using the Disperse software [44] for a 3.6mm thick unidirectional CFRP panel with the material properties given in Table 3-1 to provide comparison to the experimental and FE results. A separate set of dispersion curves was calculated for wave propagation directions between 0° and 90° in 5° increments to obtain theoretical values for each angle relative to the fibre orientation. The phase slowness curve for the A_0 mode at 75kHz was then calculated from the dispersion curves, as shown in Figure 5-4a. Wave skew angle values for each incident wave direction were then calculated from the slowness curve by taking the difference between the group and phase directions. The group direction was calculated by taking the normal of the tangent to the slowness curve at a particular phase direction, as shown schematically in the diagram in Figure 5-4a. The Disperse values for the wave skew angle are shown in Figure 5-4b. As expected, zero skew angle is observed in the principal (0° and 90°) directions. The highest skew angle of 25° is predicted in the 45° direction. Knowledge of the wave skew angles, and in particular the directions in which high skewing occurs will be essential to accurately calculate phase and group velocity in section 5.4.

5.4 Directional Dependence of Guided Wave Velocity

In this section the angular dependency of phase and group velocity of the A_0 mode in unidirectional CFRP is investigated for both point and line sources 40mm and 80mm in length. The method for calculating velocities is presented before discussing the influence of source type. The raw, uncorrected guided wave velocities are then presented for each of the sources, however a significant offset from theory is observed for the point and 40mm line excitation. A velocity correction, based on the wave skew angle is applied to the raw values, before the final corrected velocities are presented and discussed.

5.4.1 Calculating Phase and Group Velocity

Phase and group velocities were calculated for each excitation type and each wave launching direction. Signals were time gated using a moving time window to remove any reflected pulses. The phase velocity, c_p, was calculated by taking the FFT of each signal plotting the phase angle at the centre frequency f (75kHz) against distance from the source x, taking care to remove any 2π phase jumps. A linear fit was performed, and the gradient of the line extracted. Multiplying the inverse of this gradient by a factor of $2\pi f$ yields the phase velocity as given in the following equation [165]:

$$c_p = 2\pi f \frac{\Delta x}{\Delta \phi} \tag{5.6}$$

The group velocity, c_g , can be calculated by taking the envelope of the signal as the absolute value of the Hilbert transform, and extracting the arrival time of the envelope maximum, T_{max}. Plotting T_{max} against distance from the transducer x, and performing a least-squares fit, the gradient $\frac{\Delta T_{max}}{\Delta x}$ can be obtained. The group velocity is equal to the inverse of this gradient:

$$c_g = \frac{\Delta x}{\Delta T_{max}} \tag{5.7}$$

It was found that group velocity calculation is sensitive to pulse distortion due to dispersion. A narrowband bandpass 8th order Butterworth filter was applied to the time signals with cut-off frequencies 70kHz and 80kHz, respectively, before

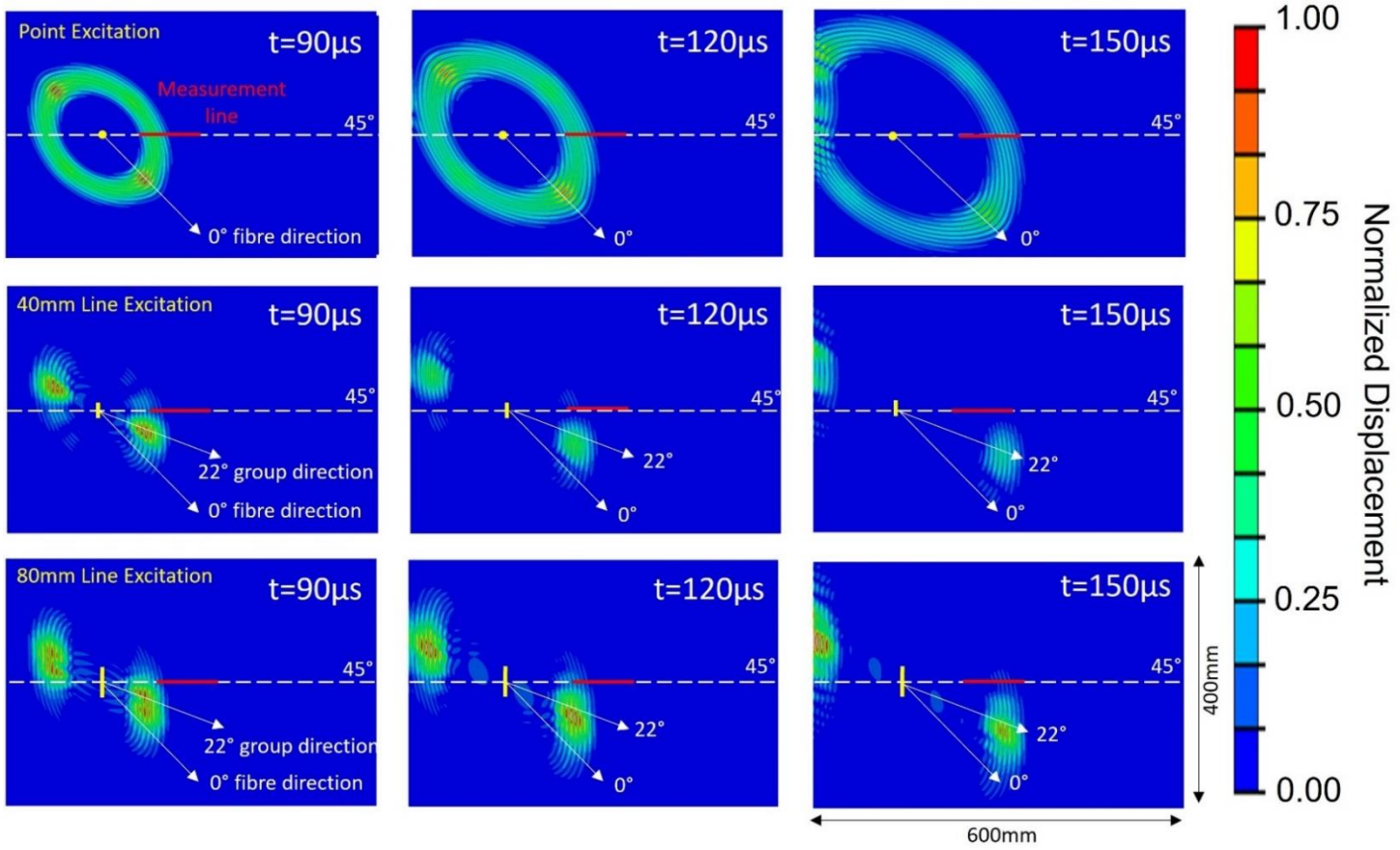

Figure 5-5 Normalized displacement magnitude contour plots for different source types in 45° wave launching direction. Obtained from FE simulations at time snapshots 90ns, 120ns, 150ns, respectively. Top row: point source; middle row: 40mm line source; bottom row: 80mm line source. Point source magnitudes shown at 10x actual values so they are visible compared to line sources.

calculating the Hilbert envelope to account for this. It should be noted that the velocity calculations were repeated at 100kHz, and it was found that the additional narrowband filtering was not required to give accurate results, indicating that pulse distortion is less severe at this frequency. This is likely due to the A_0 mode dispersion curve having a lower gradient at 100kHz than 75kHz. In this chapter only the 75kHz results are reported for clarity, however the 100kHz results can be found in reference [166].

5.4.2 Variation of Guided Wave Source

Time snapshots of the out-of-plane displacement for point, 40mm line, and 80mm line sources were obtained from the FE models and are presented in Figure 5-5 for line sources in the 45° wave launching direction. The 45° direction is aligned along the dashed white lines for each source type. Both line excitations are plotted on the same amplitude scale. However, for the point source, which has a significantly lower excitation amplitude due to the out-of-plane force being applied to a single node, the amplitudes have been amplified so that they are visible in the figure.

For the point source (top row Figure 5-5) an oval shaped wavefield can be observed due to the anisotropy influencing waves directed radially outwards from the source. Higher amplitude and wave velocity along the 0° direction can be observed, indicating that energy focusing is occurring along the fibres as expected. For the 40mm line excitation, the finite width of the excitation can be clearly observed. Despite significant wave steering, the wavefronts remain parallel to the wave launching (phase) direction, consistent with predictions in the literature [62]. However, the wave pulse has been significantly steered away from the wave launching direction (dashed line) towards the group direction. For the 80mm line source the wavefronts also remain parallel to the wave launching direction. Wave steering is again observed, however due to the longer line source length and thus pulse width, a measurement line in the original wave launching direction (along white dashed line) is able to capture some of the energy of the pulse. From the images presented in Figure 5-5 it can be seen that significant wave skewing occurs in unidirectional plates, as expected from the theoretical wave skew angles calculated in section 5.3. Understanding

which part of the propagating wave field is being detected by the measurement points (along white dashed line) will be important when it comes to interpreting the velocity measurements in the following section.

5.4.3 Uncorrected Velocity Values

Figure 5-6 shows the raw experimental and FE phase and group velocity measured for different wave launching directions, compared to values from dispersion curves. Good agreement is observed between the FE point source values and the experimental measurements from a point source (PZT disc), indicating that the FE accurately captures wave propagation behaviour occurring in the physical specimen. The velocities along the principal axes (0° and 90°, zero skew angle) are in good agreement (1%) with the Disperse values. However, a significant offset between Disperse and measurement can be observed in the non-principal directions with the largest discrepancy (8%) observed in the 45° direction (highest predicted wave skew angle of 25°, see Figure 5-4b). As the calculation of Disperse values assumes a planar wavefront and increasing the length of the line source results in a closer agreement with Disperse, it was initially thought that the offset was related to the ratio of the length of the line source to the wavelength of the excitation. This originates form Huygens principle where a planar wavefront can be considered as an infinite line of point sources [167]. Provided that the length of the line source is

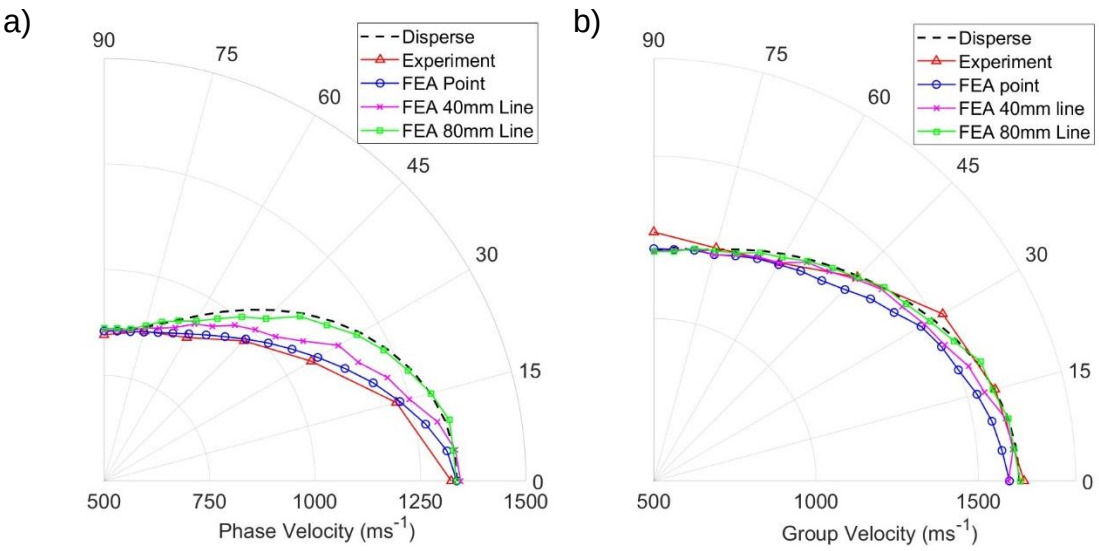

Figure 5-6 Raw, uncorrected measured and simulated a) phase and b) group velocities of the A_0 mode at 75kHz for a point (FE and Experiment), 40mm line (FE), and 80mm (FE) line source respectively, compared to values obtained from Disperse.

sufficiently larger than the wavelength of the excitation, a line source can be used to approximate a planar wavefront. In the case of the A_0 mode at 75kHz, the wavelength is approximately 20mm. It was found that for line excitations approximately the wavelength of the propagating waves, measured phase and group velocities matched the point source values (demonstrated for 100kHz in [168]). However, if the length of line source was solely responsible for the offset, this does not explain why good agreement occurs in the principal wave directions. As the degree of offset is correlated with the magnitude of the skew angle in the corresponding direction the offset is most likely caused by wave steering effects due to anisotropy not being accurately accounted for in the velocity analysis.

The velocities from the 40mm line source are closer to the theoretical values than the point source values, however a significant offset still remains. Despite the line source behaving more like a planar wavefront, as seen in Figure 5-5, the significant steering from the measurement location results in an offset in the velocities calculated from the FE simulations. As seen in time snapshots in Figure 5-5, the planar wavefront of the 80mm line source is long enough for the perpendicular measurement lines to capture more energy of the wave pulse compared to the 40mm source despite the significant steering. This results in the phase and group velocities for the 80mm line source (FE only) matching Disperse predictions within 1%. The results in Figure 5-6 indicate that wave steering effects impact the accuracy of velocity measurements, with significant offsets observed for both the point and 40mm line source. Comparing the degree of offset to the calculated skew angles presented in Figure 5-4b, it can be seen that a larger discrepancy occurs in directions with greater skew angles. A skew angle correction should therefore be applied to the phase velocities to mitigate this offset.

5.4.4 Anisotropic Velocity Wave Skew Correction

To accurately measure velocities from the 40mm FE line source, a diagonal line of measurement points (as shown in Figure 5-2a) was defined along the group direction (obtained from Figure 5-4a) as shown in Figure 5-7. This enables the velocity measurement to be taken in a region where sufficient wave energy is

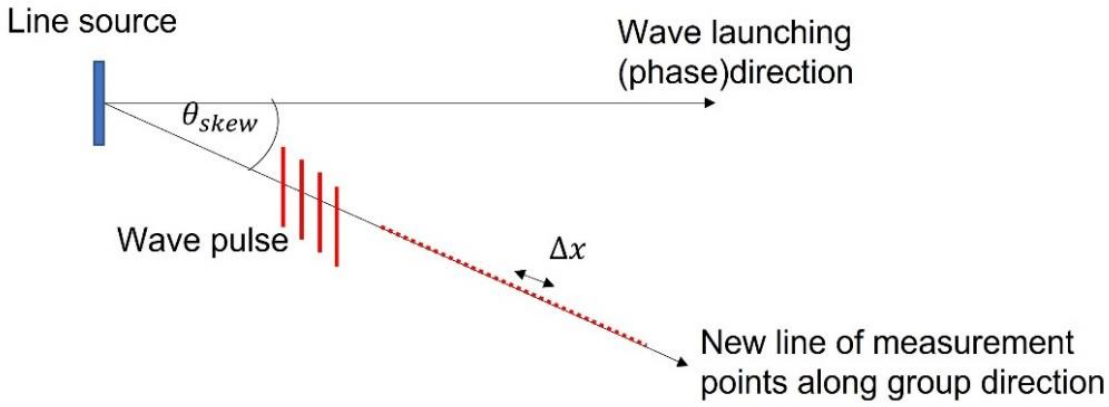

Figure 5-7 Schematic of skew angle corrections for a linear source.

present. As the wave fronts stay parallel to the wave launching direction, a projection of the phase or group velocity can then be calculated along the wave launching (phase) direction by multiplying the uncorrected phase or group velocity (Equations 5.6 or 5.7) by a factor of $\cos(\theta_{skew})$, where θ_{skew} is the wave skew angle.

For the point source, measuring a region of the wavefront with sufficient energy is less of an issue (see Figure 5-5), but wave skewing effects nevertheless occur. In this case the wave pulse measured in a given direction will have actually originated at a different phase direction and steered due to anisotropy. To calculate the corrected velocity, the velocity along the corresponding group direction should be projected into the wave launching (phase) direction by multiplying by a factor of $\cos(\theta_{skew})$.

$$c_p(\theta_{phase}) = c_p(\theta_{group})\cos(\theta_{skew}) \tag{5.8}$$

$$c_g(\theta_{phase}) = c_g(\theta_{group})\cos(\theta_{skew}) \tag{5.9}$$

For example, waves launched in the 45° direction have a skew angle of 25°, so taking the velocity measured in the 20° direction (group direction) and multiplying by $\cos(20°)$ will yield the correct velocity value. The uncorrected velocities shown in Figure 5-6 were obtained in 5° increments, so velocity values were linearly interpolated to obtain uncorrected values in 1° increments.

5.4.5 Corrected Velocity Values

Figure 5-8 a shows the corrected measured and simulated phase velocity values for a point (FE and experiments) and a 40mm (FE only) source at 75kHz compared with the theoretical values obtained from Disperse. Very good agreement of the FE evaluation for a line and point source with the Disperse values can be seen. The maximum difference is less than 1%, indicating that the correction for the wave skew due to anisotropy allows accurate determination of the phase velocity for a point source.

Experimental results in general agree well and show the same angular dependence, but a maximum offset of 2% between dispersion curves and measurement can be observed in the 15° and 30° directions. This could be due to either experimental uncertainties or a slight offset in the assumed material properties. A similar trend can be observed for the group velocity values shown in Figure 5-8b. A small offset of up to 2% can be observed for the point source FEA results, with agreement within 1% along the principal axes. For the 40mm line source, the corrected group velocity values show very good agreement within 1% of the Disperse values. The measured point source velocity values are in reasonable agreement with the FE results.

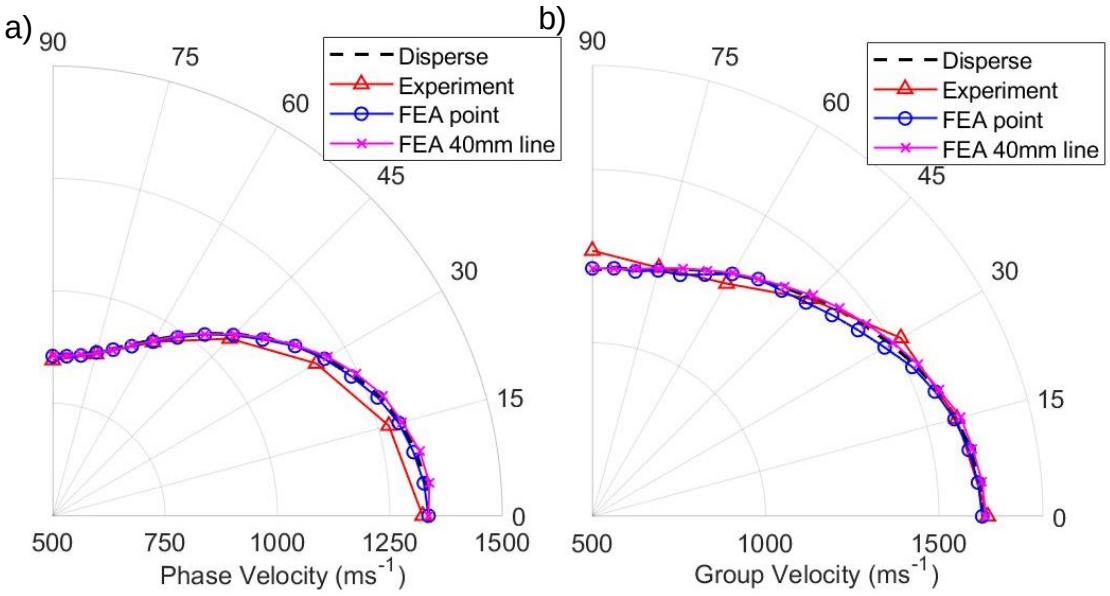

Figure 5-8 Measured, simulated, and theoretical a) phase and b) group velocity variation with propagation angle at 75kHz centre frequency. Experiments were performed for a point source (PZT disc transducer).

Several studies have considered the directionality of group velocity in composites consistent with the results presented here, although not all cases have validated results against predictions from dispersion curves [47,55,78,79]. Whilst the concept of directionally dependent phase velocities has been established in principle, limited experimental or numerical studies of this effect can be found in the literature. Previously, phase velocity dispersion curves have been measured for multiple wave propagation directions; however, these were not compared against theoretical predictions [54]. Zhao et al. [80] and Rhee et al. [60] discuss an offset of group velocity due to the skew angle equivalent to the 'velocity correction' proposed above, however this correction was never illustrated through simulation or experiment.

The results presented in Figure 5-6 and Figure 5-8 indicate that care should be taken when measuring phase and group velocities in an anisotropic material, particularly if using a point source such as a PZT disc, often selected for guided wave measurements. Whilst the skew angle correction for a point source works well, some knowledge of the material anisotropy and expected wave skew angle is required. Whilst the 40mm line source matches the theoretical assumption of a planar wavefront, a correction for the wave skew angle is still required due to the deviation of the pulse from the original measurement location. Using a line source of sufficient length (e.g., 80mm) can mitigate this effect. Overall, the FEA model has been demonstrated to accurately predict wave propagation behaviour, showing good agreement with dispersion curves and experimental measurements.

5.5 Visualising Wave Skew

In order to understand the influence of material anisotropy on wave propagation, the wave steering behaviour in the plate should be determined. The images in Figure 5-9 and Figure 5-10 visualize the time traces obtained along each line of measurement points, equivalent to a B-scan. Figure 5-9 shows the FE simulated out-of-plane displacement time traces from a 40mm line source at each measurement point for lines of points located 100mm, 150mm, 200mm from the source in the 0°, 30°, 60°, and 90° wave launching directions. In the 0° direction (top row, Figure 5-9) the wave pulse does not

deviate from the initial propagation direction and does not show significant widening as it propagates along the plate. In the 30° direction (2nd row, Figure 5-9) significant deviation from the wave launching direction towards the 0° direction can be observed, in addition to slight widening of the beam. In the 60° direction (3rd row, Figure 5-9), the beam is skewed towards the 0° direction to a similar degree as the 30° direction, however the beam widening at 60° is much more significant. In the 90° direction (bottom row, Figure 5-9) no beam steering is observed, however significant beam widening occurs as the wave pulse propagates. This is partly due to the energy focusing along the fibres, which are now perpendicular to the propagation direction. In each of the wave launching directions, the orientation of the wavefronts remain parallel to the wave propagation direction, irrespective of the degree of steering experienced as expected.

Figure 5-10 shows the measured wavefield images 100mm, 150mm, and 200mm from the 40mm line transducer in the 0°, 30°, 60°, and 90° directions. As expected, the measured wavefield is less uniform than for the simulations, however the wave steering and spreading behaviour is similar. In the 0° direction the main wave pulse remains focused along the wave launching direction with limited beam spreading. In the 30° direction the wave pulse consists of two regions of high amplitude, which is not observed in the FEA. Significant wave steering from the initial direction can be observed, consistent with the FEA and wavefield images reported by Salas and Cesnik [66]. Beam spreading can also be observed in the wavefield images in Figure 5-10, particularly at 200mm where the gap between the two wave pulses has significantly increased.

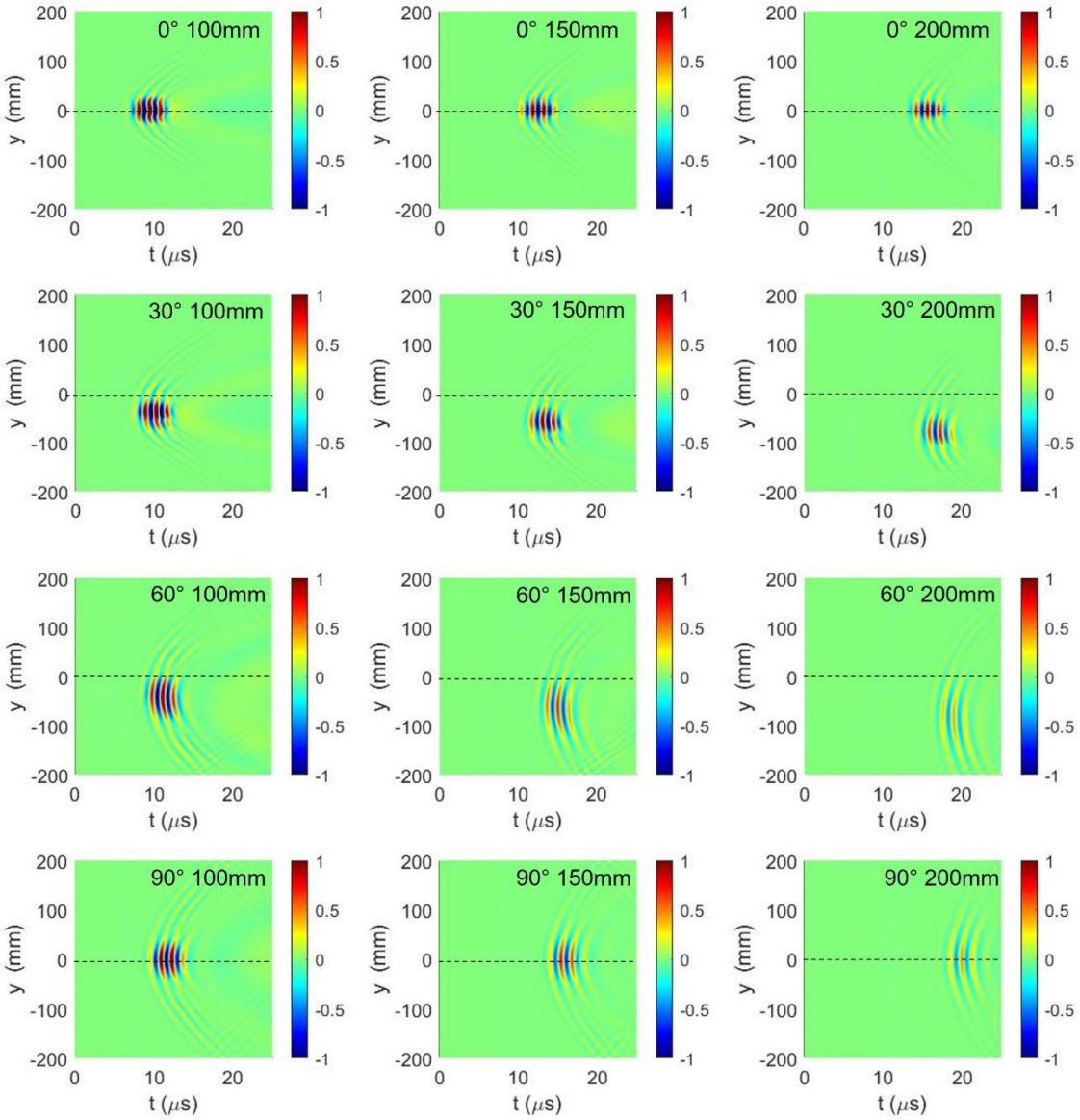

Figure 5-9 Normalized displacement time traces along a single line of measurement points (parallel to excitation line source) for A_0 mode obtained from FEA (equivalent of a B-scan). Wave launching angles of 0°, 30°, 60°, and 90° at three lines of measurement points located 100mm, 150mm, and 200mm from excitation location, respectively. The wave launching direction represented by dashed line at y = 0mm.

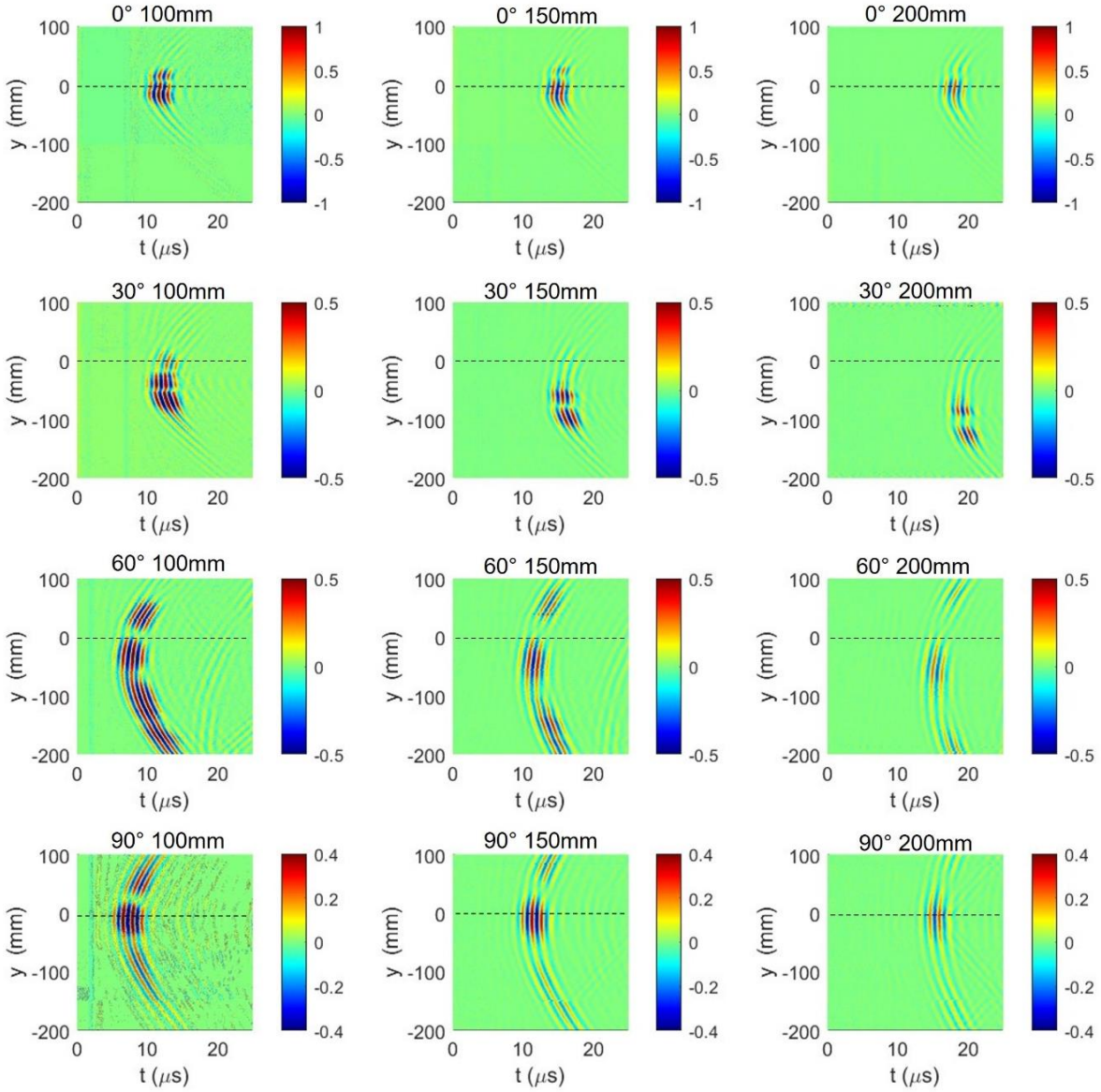

Figure 5-10 Experimentally measured displacement time traces along a single line of measurement points (parallel to excitation line source, equivalent to B-scan) for A_0 mode generated by line transducer (40mm length). Wave launching angles of 0°, 30°, 60°, and 90° at three lines of measurement points located 100mm, 150mm, and 200mm from excitation location, respectively. The wave launching direction is represented by dashed line at y = 0mm.

In the 60° direction the main central pulse shows wave skewing behaviour as expected. The central pulse, which originates from the front of the line source, is more difficult to distinguish in this direction, particularly at 100mm from the source, but also displays beam spreading. No steering is observed in the 90° direction as expected but spreading of the central pulse occurs. The measurements show that beam spreading increases with wave launching angle. As seen in the FE modelling, the wavefronts remain oriented parallel to their initial launching direction. In the experimental measurements the amplitude of guided waves decays more severely as the propagation angle is increased, compared to the FE results. This is likely as a result of the limitations of using stiffness proportional Rayleigh damping to model attenuation, as discussed in section 5.2.

In order to analyse the energy distribution of the line wave excitation in more detail, the maximum amplitude of the wave pulse was calculated at each measurement point along the 5 lines of measurement points parallel to the line source orientation. Figure 5-11a/b shows the simulated and measured amplitudes for the A_0 mode propagating along the 0° wave launching direction. The measurement lines at 125mm and 175mm from the source have been omitted for clarity of the figures. No wave skew is observed for simulated results (Figure 5-11a) as the peaks are aligned. No beam spreading is visible due to energy focusing effects. The main peak of the experimentally measured wave pulse also shows no wave skewing and limited beam spread (Figure 5-11b). The second peak to the right of the main peak is caused by non-uniformity in the experimental line excitation and is due to waves being generated from the ends of the transducer. Figure 5-11c/d shows the simulated and measured amplitudes along the 90° wave launching direction. In both measurement and simulation no wave skew is observed as the peaks are aligned, but significant beam widening, consistent with the wavefield results in Figure 5-9 and Figure 5-10, can be seen.

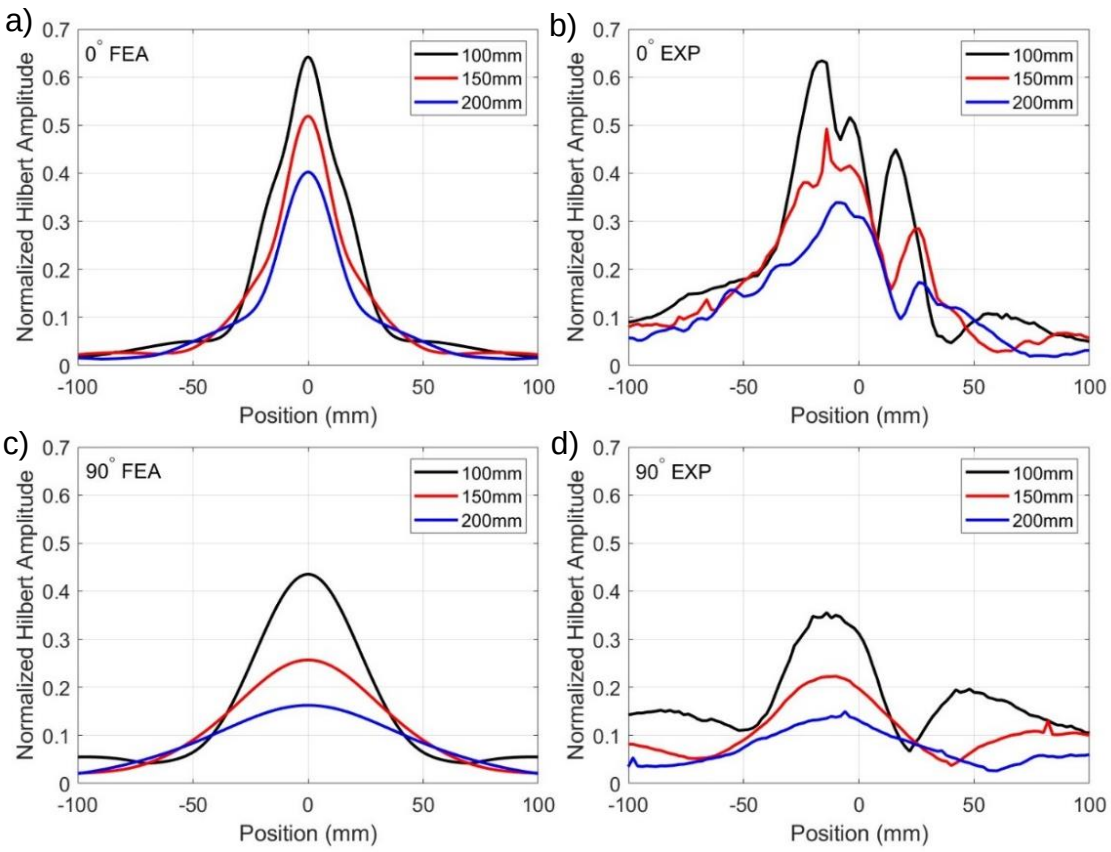

Figure 5-11 Normalized maximum wave pulse envelope (Hilbert transform) amplitude along lines of measurement points located 100mm, 150mm and 200mm from line source for a) 0° direction FEA; b) 0° direction experiment; c) 90° direction FEA; d) 90° direction experiment.

The measured and simulated amplitudes along the 30° and 60° wave launching directions are presented in Figure 5-12a/b and Figure 5-12c/d respectively. Wave skewing can be observed in each of the cases as the main amplitude peaks shift to the left with increasing distance from the source. In the 30° direction some beam spreading is observed in the FE results, but this is more difficult to observe in the experiments due to the double amplitude peak. The double peak is not present in the FE results, although as the wave pulse propagates a secondary peak starts to develop to the right of the main pulse. The double peak in the experiments is likely due to the imperfect line excitation, but in this case could be caused by destructive interference at the centre of the transducer, whose length is approximately twice the wavelength at 75kHz. For the 60° wave launching direction beam skewing again is observed in both the experiment and simulation. Beam spreading in the 60° direction is more severe than in the 30° direction as expected, however, slightly counterintuitively, appears to also be greater than the spreading observed in the 90° direction.

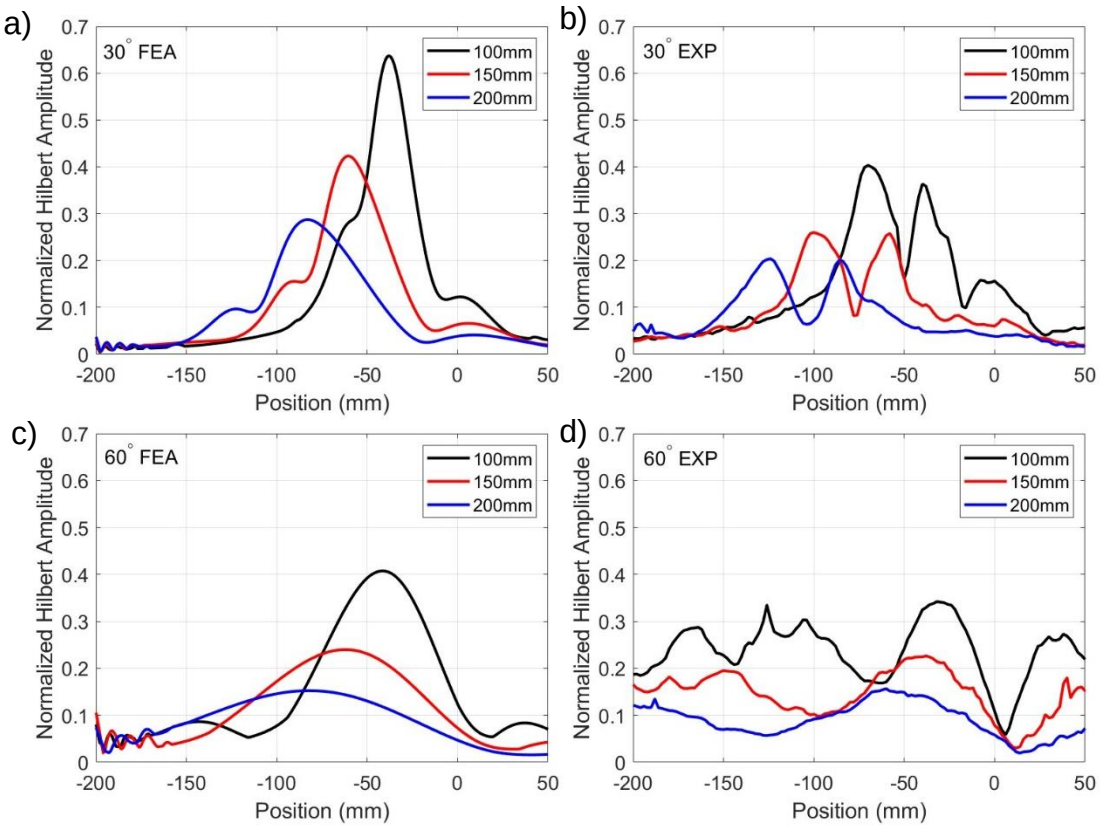

Figure 5-12 Normalized wave pulse envelope (Hilbert transform) amplitude along lines of measurement points located 100 mm, 150 mm, and 200 mm from line source for a) 30° direction FEA; b) 30° direction experiment; c) 60° direction FEA; d) 60°direction experiment.

5.6 Calculation of Wave Skew Angles and Beam Spreading

The results in section 5.5 show that the position of the wave pulse changes with propagation direction in the non-principal directions for non-zero skew angles. To quantify the wave skew angle, the aim is to track the position of the wave pulse y over distance d, which should vary linearly. The position of the wave pulse is then plotted against distance from the source and a linear fit performed. The gradient of the fit can then be extracted, and the skew angle calculated as follows:

$$\theta_{skew} = \tan^{-1}\left(\frac{\Delta y}{\Delta d}\right) \tag{5.10}$$

One way to estimate the position of the wave pulse is to simply take the location of the maximum amplitude along the wave pulse [153]. To estimate the beam spread we can take the calculated the 6dB drop in amplitude from the peak maximum and obtain the locations where the wave pulse has this amplitude drop in order to estimate the width of the pulse. We can then track the widening

over propagation distance and perform a linear fit on the beam widths. A beam spreading angle can then be expressed by taking the inverse tangent of the gradient of this line. Whilst this method works reasonably well for a uniform excitation with a single, symmetrical peak, this method becomes less accurate when the peak is not uniform and is not possible to use when the excitation consists of multiple peaks as shown in Figure 5-12. Therefore, a curve fitting method, as described in the following section, was used to account for the multiple peaks when calculating skew angles.

5.6.1 Curve Fitting Method

A variety of Gaussian and Lorentzian functions were fitted to the amplitude curves for each wave launching direction. For smooth amplitude curves such as in the 0° direction (Figure 5-11a) a Gaussian function already provided a good fit, however in directions with multiple amplitude peaks a more complex fitting function was required to match the features. Figure 5-13 shows the fitted FE and experimental curves for the 30° wave launching direction for a Gaussian (Figure 5-13 a/b), Lorentzian (Figure 5-13 c/d), and a three term Gaussian curve (Figure 5-13 e/f). The sum of two Gaussian and two Lorentzian functions were also investigated respectively; however, it was not possible to fit these functions to either the experimental or FE data. The 30° wave launching direction is considered as this was the worst case in terms of pulse uniformity for both the measurement and simulation. The starting points for the MATLAB fitting algorithm were optimised for each propagation angle. As seen in Figure 5-13a, fitting a Gaussian function to the FE data provides a reasonable fit ($R^2 > 0.94$), but does not capture the full peak amplitude or adequately account for the side peaks either side of the main peak. A Gaussian can be fitted to the dual peak in the experimental data (Figure 5-13a) but the fit curve represents an average between the two peaks. Whilst the fitting was poor ($R^2 > 0.3$), taking the maximum of the Gaussian provided a surprisingly accurate wave skew angle. The Lorentzian fit in Figure 5-13c visually provides a better match to the FE data than the Gaussian fit ($R^2 > 0.97$), however this function provides an extremely poor fit for the experimental data in Figure 5-13d. The three term Gaussian fit shown in Figure 5-13e provides a very good match for the FE curves, accounting for the side peaks as well as fitting the main peak very

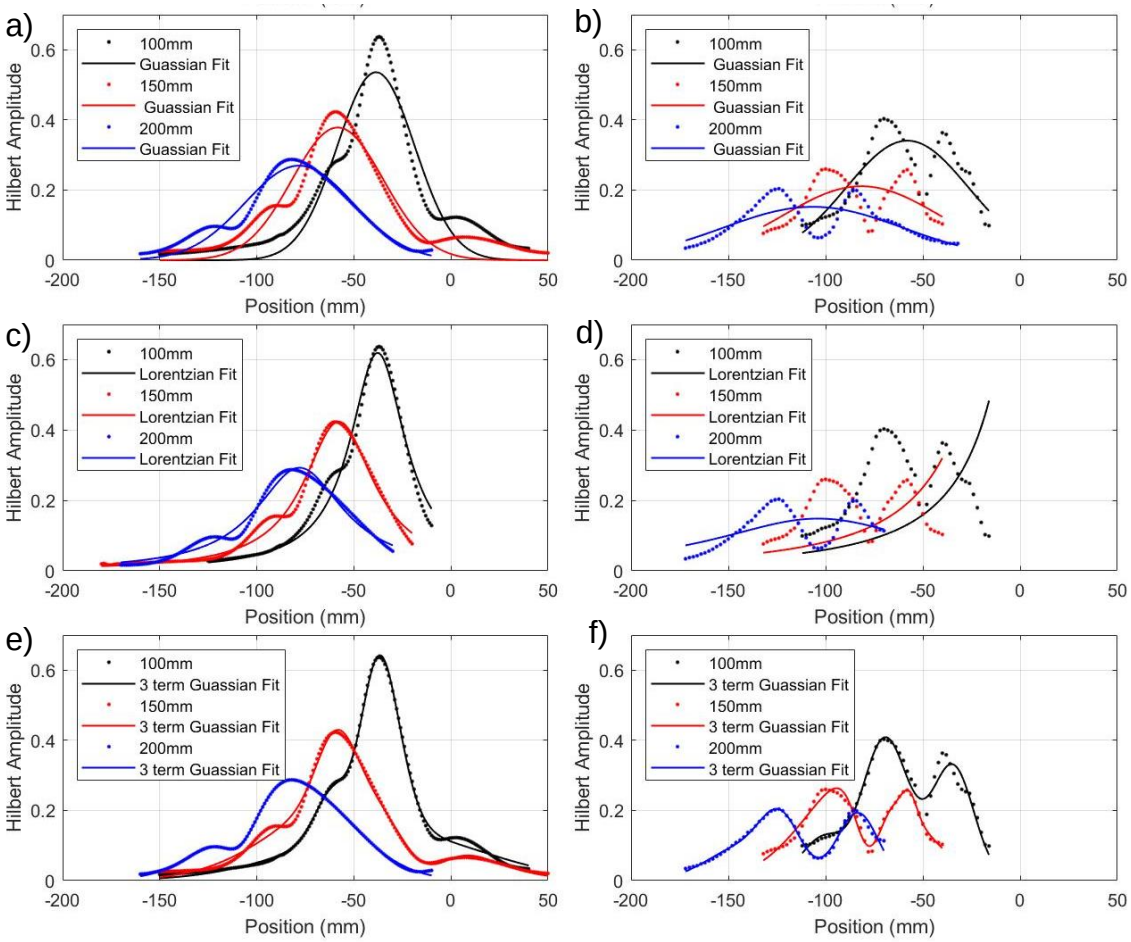

Figure 5-13 Measured and simulated amplitude curves with various curve fitting functions, 30° wave launching direction. a) Gaussian fit FE data; b) Gaussian fit experiment c) Lorentzian fit FE; d) Lorentzian fit experiment; e) three term Gaussian fit FE; f) three term Gaussian fit experiment.

well ($R^2 > 0.99$). Additionally, the three term Gaussian fits the dual peak in the experimental measurements well and provided the best fit ($R^2 > 0.98$) among the tested functions across each of the propagation directions. The sum of three Gaussian functions was therefore selected for the wave skew and beam spread analysis.

5.6.2 Wave Skew Calculation

In order to estimate the position of the wave pulse the weighted sum of three standard Gaussian functions was fitted to each amplitude curve:

$$f(x) = a_1 \exp\left[-\left(\frac{x-b_1}{c_1}\right)^2\right] + a_2 \exp\left[-\left(\frac{x-b_2}{c_2}\right)^2\right] + a_3 \exp\left[-\left(\frac{x-b_3}{c_3}\right)^2\right] \qquad (5.11)$$

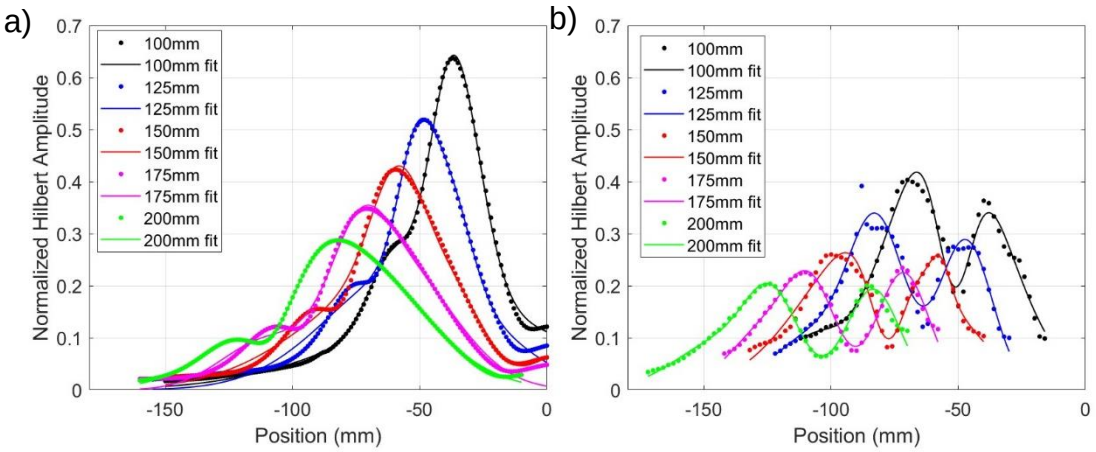

Figure 5-14 Normalized maximum Hilbert amplitude for 30° wave launching direction with triple Gaussian curve fitting for a) FEA and b) experiment.

Where the coefficients a_n represent the amplitude of each Gaussian peak, the coefficients b_n represent the centroid of each peak and coefficients c_n are related to the width of each peak. To estimate the true centre of the wave pulse, a weighted average of the peak centroids was performed (i.e., b_n weighted with respect to a_n).

The fitting procedure was performed on both the simulated and experimental curves for each of the wave launching directions and is shown for the 30° direction in Figure 5-14. The skew angles were calculated by plotting the averaged centre location of each amplitude curve against distance from the source. A linear fit was then performed, and the wave skew angle calculated from the inverse tangent of the line gradient. This process was repeated for each wave launching direction and skew angles from the fitted curves were compared with the theoretical values obtained from the phase slowness curve and shown in Figure 5-15a. The measured skew angles follow the overall pattern of the theoretical values and show good agreement with theory in the directions with lower skew angles, consistent with measurements for the 20° direction reported in literature [48]. In the principal directions almost zero skew angle (Experiment: 0.6°, FE: $0.1° \times 10^{-19}$) is observed as expected. The maximum skew angle of 28.3° is measured for the 45° wave launching direction with almost symmetric skew angles either side of this. The skew angles are slightly higher for the 0°-45° directions than for the 45°-90° directions, likely due to the effect of energy focusing causing greater beam steering in these

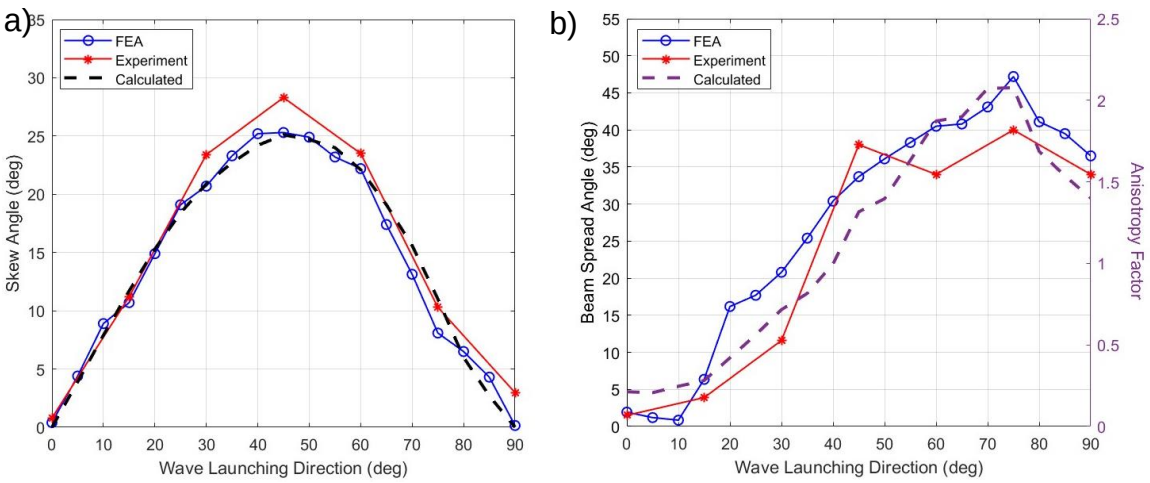

Figure 5-15 a) Measured, simulated, and theoretical skew angles for wave launching directions between 0° and 90°; b) estimated beam spread angle with wave launching direction from FE and experimental measurement, overlaid with anisotropy factor.

directions. Overall, there is good agreement (2%) between theory and FE, however the experimentally measured skew angles are slightly higher than expected (10% variation) in the high skew directions (30° to 60°).

As the experimentally measured point source velocities showed good agreement with theory, it is unlikely that the error in skew angle is due to incorrect material properties. The experimental error in the wave skew angles could be caused by the quality of the line source excitation. Therefore, if measured skew angles are required for the phase velocity correction (Eq. 5.8 and 5.9), care should be taken to ensure the line source excitation is of high quality. Previous work achieved good agreement between measured and theoretical skew angles in composites for a single wave propagation direction [61,74]. For example, Lowe et al. [48] experimentally measured the wave skew angle in a single direction using a line source consisting of multiple PZT disks bonded to the surface of the CFRP specimen described in section 3.1. In contrast, these results use a repositionable line source and consider multiple wave directions, in addition to performing numerical simulations of the wave skewing behaviour, extending the previous study.

5.6.3 Beam Spread Calculation

Previous studies on guided wave propagation in monocrystalline silicon have qualitatively observed beam spreading behaviour [58]. Qualitative measurement of beam spreading behaviour and, subsequently, comparison to theoretical

predictions had not been previously investigated. In order to estimate the beam spreading, the full width at half maximum (FWHM) of the wave pulse was tracked over distance. The FWHM of a three term Gaussian function can be calculated as

$$FWHM = 2c_{av}\sqrt{2\ln 2} \tag{5.12}$$

Where c_{av} is an average of the c_n coefficients in Eq. 5.11 weighted with respect to the corresponding amplitude coefficients a_n. Whilst fitting the data is not strictly required to calculate the FWHM of the energy distribution of the line excitation, this method allows for excitations consisting of multiple peaks (e.g., Figure 5-14) to be accounted for. The FWHM was calculated for each of the five amplitude curves shown in Figure 5-14 plotted against distance from the source and a linear fit was performed. The gradient was extracted from the fit and the beam spreading angle was estimated by taking the inverse tangent of this gradient.

The measured and simulated beam spread angles were calculated for each wave launching direction and are shown in Figure 5-15b. The theoretical anisotropy factor A (Eq. 2.2) was calculated for each of the wave launching directions and is also plotted. The additional factor of $(\cos(\theta_{skew}))^{-2}$ in A compared to the divergence D (Eq. 2.1) gave a slightly better match to the FE and experimental results. It should be noted that the anisotropy factor is a dimensionless quantity and thus cannot directly be compared to the calculated beam spread angle. Linking the spread angle to the anisotropy factor would require measuring the spread angle for an isotropic material with similar characteristics to CFRP, in order to provide a reference angle for A=1. This would be difficult to achieve as such a material is hypothetical and the beam spread is highly dependent on the source characteristics. However, the overall physical behaviour described by the anisotropy coefficient is similar. For example, A reaches a maximum in the 75° wave launching direction. This indicates that the beam will be widening most rapidly at 75° (A>1), matching the measured maximum beam spread angles calculated from the FE and experimental evaluation. The anisotropy factor is dependent on the curvature of the slowness curve and so accurate knowledge of the variation of phase velocities with propagation direction in anisotropic materials is required. It

should be noted that the Maris factor, which can be used to predict energy focusing [81], is distinct from the anisotropy factor, but also related to the curvature of the slowness curve.

Low beam spreading is observed for the FE results at 0° and 15°, as there is a large degree of energy focusing along the fibre direction at these wave launching angles. The spreading angle then steadily increases as the wave launching direction increases away from the fibre orientation. The highest beam spreading, slightly counterintuitively, is observed at 75°. This is likely due to a combination of energy focusing along the almost perpendicular fibre directions stretching the beam, as seen in the 90° direction, in addition to wave skewing effects enhancing the degree of spreading. The beam spreading behaviour observed here is qualitatively consistent with experimental results performed on monocrystalline silicon [43].

Severe beam spreading, as observed in Figure 5-15b, could lead to significantly lower detected signal amplitudes in certain directions, which could indicate regions where damage could be difficult to detect. The measured beam spread angles generally follow a similar pattern to the FE results, however the FE model predicts slightly higher beam spreading for most propagation directions. The accuracy of the experimentally measured beam spread angles is limited by the quality of the line excitation, which did not match the assumed uniform amplitude distribution. It should be noted that the anisotropic wave propagation effects in a unidirectional laminate will be larger than that of a cross-ply or quasi-isotropic CFRP layup. The beam steering and spreading behaviour in these laminates will be smaller but could be significant enough to reduce the accuracy of guided wave based SHM.

5.7 Summary and Conclusions

Anisotropic guided wave propagation effects were investigated for the A_0 mode in a unidirectional CFRP laminate. The directional dependence of phase and group velocity from a point and a linear source was investigated through experimental measurements and finite element modelling. Good agreement between measurements and FE simulations with theoretical velocity values was

observed. Especially for a point source, a velocity correction is required to incorporate anisotropic wave skewing effects and to obtain agreement with the theoretical assumptions of a planar wavefront. Whilst such a correction has been previously proposed for group velocities, this effect has not been demonstrated experimentally for phase and group velocities, with comparison to theoretical predictions. A line source, of sufficient length for the energy of the pulse to be captured by the measurement line despite skewing, gives good agreement with theoretical velocities, without the need for a skew correction.

Numerical and experimental studies of the wave skewing behaviour in multiple incident wave directions were performed. Zero skew angle was observed in the principal (0°, 90° relative to fibre orientation) directions with maximum skewing occurring at 45° for the experimental, FE, and theoretical values. The skew angles calculated from the FEA showed good agreement with theoretical values calculated from the phase slowness curve. The measured skew angles were slightly higher than predicted in directions with the largest degree of skewing (30°, 45°, 60°). Beam spreading was estimated from the experimental and simulation results. Limited spreading occurs in the 0° and 15° directions due to high energy focusing along the fibres occurring in these directions. As the wave launching direction moves away from the fibre directions, beam spreading generally increases. The beam spreading angle was compared with the anisotropy factor, calculated from the theoretical slowness curve. Whilst a direct comparison cannot be drawn between the anisotropy factor and beam spread angle, the physical behaviour observed in the experiments and simulations matched that of the theory. The unidirectional laminate in this study displays the most extreme example of wave propagation behaviour. However, the effects studied here will also occur to some degree in specimens with cross-ply and quasi-isotropic layups. Anisotropic effects such as severe skew angles and beam spreading, as observed for this specimen, could lead to reduced accuracy in damage location or regions where little to no guided wave amplitude can propagate in the plate. Therefore, anisotropic effects should be considered when designing SHM systems.

6 Modelling Guided Wave Scattering at Delaminations

This chapter focuses on modelling guided wave scattering around a delamination in a quasi-isotropic CFRP laminate containing an artificial insert delamination, incorporating work that has already been published in two journal articles [57,169]. Specific experimental and model geometries are introduced, building on the details given in Chapters 3 and 4. The measured scattering on top of the delamination is discussed and the wave trapping and forward scattering phenomena are introduced. Preliminary studies for the finite element model are presented, such as choice of attenuation values, and model convergence. The FE model is then validated against the experimental measurements. The results of parameter studies, such as delamination size, shape, depth will then be presented in Chapter 7.

6.1 Experimental and FE Model Geometry

Laser measurements were carried out on the 8-ply quasi-isotropic laminate (section 3.2) with layup $[-45/45/90/0]_s$ and an artificial insert delamination located at the centre of the plate between the second and third ply layers (0.4mm depth). PZT discs (PIC-255) with wraparound electrodes were used to generate the A_0 guided wave mode. The discs were bonded by cyanoacrylate glue to the surface of the composite plate 100mm from the centre of the delamination location along the 0°, +45°, -45°, and 90° incident wave directions as shown in Figure 6-1. The excitation signal was a 5-cycle sine wave modulated by a Hanning window and was generated at 50kHz centre frequency. This frequency was selected as it produced the highest signal amplitude from the wraparound transducer.

Initially a circle of points, 80mm radius, and centred on a single transducer was scanned in 2° increments to determine the amplitude of the excited wave in all directions for an undamaged region of the plate. A single transducer was excited at a time and three different scanning patterns were performed on the sample for each direction, as shown schematically in Figure 6-1. A square area 40mm x 40mm centred on the delamination was scanned in 1mm steps. A linear scan 70mm in length was performed horizontally, and vertically, in 1mm

steps with each line crossing through the central point of the delamination. A circular scan centred on the delamination with radius 30mm was performed in steps of 2°.

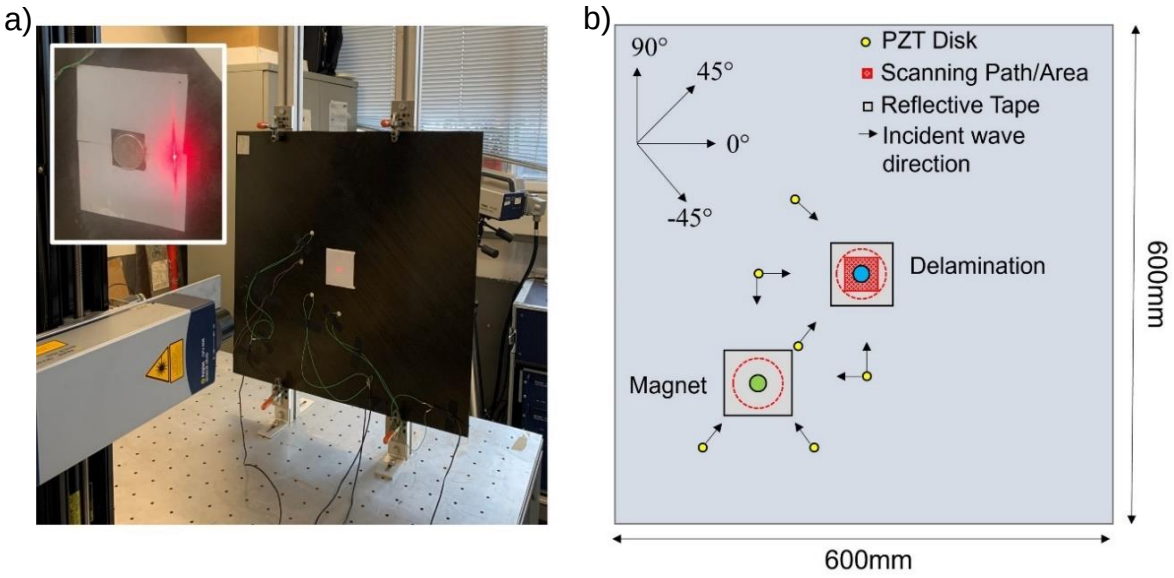

Figure 6-1 a) Photograph of CFRP panel with PZT sensors in multiple directions. Inset shows permanent magnets mounted on plate surface; b) schematic of damage and measurement locations.

To estimate the attenuation within the sample, additional line scans on an undamaged region of the plate were performed. The scans were performed along a 130mm line in 1mm steps along the 0° fibre direction. The first measurement point was at 10mm distance from the transducer. The reduction in amplitude along this line of points was used to estimate material damping.

Permanent neodymium magnets (NdFeB, Type N42, diameter 20mm, thickness 2mm) were placed on each side of the plate, in an undamaged region, shown schematically in Figure 6-1b. Set honey was applied to the magnets to couple them to the plate surface [152] and the reflective tape under the magnets removed to improve coupling (Figure 6-1a inset). PZT transducers were bonded 100mm from the magnet centre in the 0°, 45°, -45°, 90° directions. Again, a single transducer was excited and a 30mm circular scan was performed in 2° increments centred on the magnet. A baseline scan was performed before the magnets were applied and was repeated after the magnets were removed. Measurements were repeated for each incident wave propagation direction.

A full 3D layered FE model of a quasi-isotropic laminate with dimensions 600mm x 600mm x 1.6mm was developed. Each ply layer was modelled as a unidirectional layer of elements, initially with a single element through the thickness (0.2mm). Initially, a 20mm x 20mm circular delamination was incorporated into the model at depth 0.4mm and is used as the standard case throughout. This delamination size was selected to approximately match the dimensions of the delamination in the physical specimen, obtained from ultrasonic C-scan [151]. Further details of the delamination modelling procedure are given in section 4.5.

An out-of-plane force was applied to a single node located 100mm from the delamination centre to simulate generation of the A_0 mode. The excitation node was defined 100mm from the delamination centre, initially in the 0° direction and then varied to 90°, -45°, and 45° to match experiments. A separate simulation was performed for each incident wave direction. The excitation signal was a 5-cycle sine wave modulated by Hanning window with a centre frequency of 50kHz. Stiffness proportional damping was included into the model. The (Rayleigh) damping coefficient was set to β = 30ns. The rationale for this choice is discussed in section 6.4. An element size of 0.5mm x 0.5mm x 0.2mm was selected with a stable time increment of 50ns and a simulation time of 0.3ms. The choice of element size is further discussed in section 6.5. A 60mm x 60mm grid of monitoring points centred on the delamination was defined in 1mm steps. History output requests for the out-of-plane displacements were recorded at each measurement point. A 40mm x 40mm grid, bilinear interpolation onto a 30mm circle, and horizontal and vertical lines can be selected from this data during analysis for comparison to the experiments. A baseline model containing no damage was also created for each incident wave direction. Magnets were modelled as bonded masses attached to the baseline plate model to match experimental measurements as described in section 4.5.

6.2 Measured Scattering at Delamination

Three different analysis methods of the time traces were performed on the 40mm x 40mm grid measurements on top of the delamination and are presented in Figure 6-2. A Fast Fourier Transform (FFT) was performed, and

the magnitude at the centre frequency of the excitation (50kHz) was extracted for each measurement point (Figure 6-2a). This analysis measures the amplitude of the A_0 mode at a specific frequency. The maximum amplitude of the Hilbert envelope of the signal was extracted for each measurement point (Figure 6-2b). The total energy of the signal at each measurement point was estimated by taking the square of the sum of the magnitude of the signal at each point along the time trace (Figure 6-2c). Both the Hilbert and energy sum analyses measure the amplitude of the A_0 mode, averaged over the full frequency bandwidth of the signal.

Figure 6-2a shows the measured FFT magnitude over a 40mm x 40mm grid of measurement points. The incident wave propagates from left to right. It can be seen that the magnitude significantly increases in a circular region with the approximate area of the delamination. The high magnitude over this region indicates that energy trapping is occurring within the delamination, which has been reported previously [94,95,107,108]. The regions of high and low amplitude suggest that there are multiple reflections of guided wave modes within the delamination. This high amplitude region also indicates that we are measuring on top of the thin (2 ply thickness) sub-laminate, rather than on the opposite side of the plate. A strong forward scattered wave can be observed at the right of the delamination, with two ‘shadow’ regions of low magnitude either side indicating destructive interference leading to lower wave amplitude. The small spots of high amplitude at the top of Figure 6-2c are either due to experimental noise or an imperfection in the retroreflective tape. A crescent shape can be observed at the delamination entrance, at the left of Figure 6-2a. This is likely caused by interference between the incident wave, and backscattered waves from the delamination entrance.

The Hilbert amplitude and energy of the signal provide similar relative amplitudes to the FFT analysis. As seen in Figure 6-2, a region of high amplitude on top of the delamination and a forward scattered wave at the delamination exit is observed for both the Hilbert amplitude and the total energy of the signal. The shadow regions of interference at either side of the forward scattered tail, and the crescent shape backscattered interference are present in all three images, but they are much fainter in Figure 6-2c. Overall, similar

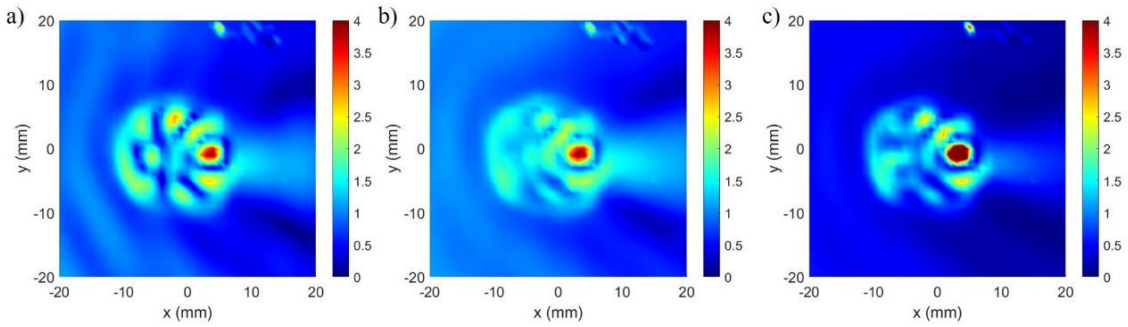

Figure 6-2 Measured scattered wavefield of A_0 mode at 50 kHz in 40 mm x 40 mm area centred on circular delamination (diameter: 20 mm); a) Normalized magnitude of FFT at 50 kHz; b) Normalized maximum amplitude of signal envelope; c) Normalized total energy of wave.

scattering patterns can be observed for each of the three analyses presented in Figure 6-2, however to isolate the scattered wave using a baseline subtraction method which preserves both amplitude and phase information (described in section 6.3) the FFT analysis is required. Therefore, the FFT magnitude will be considered for the rest of this chapter unless otherwise stated.

6.3 Baseline Subtraction Analysis

In addition to the interference pattern on top of the delamination, understanding the scattered wave propagating in the undamaged laminate away from the damage is important for SHM. However, it is difficult to observe scattering behaviour by simply taking the amplitudes as shown in Figure 6-2 as these amplitudes contain both the incident and scattered components of a signal. A baseline subtraction analysis can be used to isolate the scattered component, by removing the incident wave. The complex difference between baseline and damage FFT magnitude was calculated to obtain the scattered wave. This method is advantageous as it allows for both amplitude and phase information to be preserved [170].

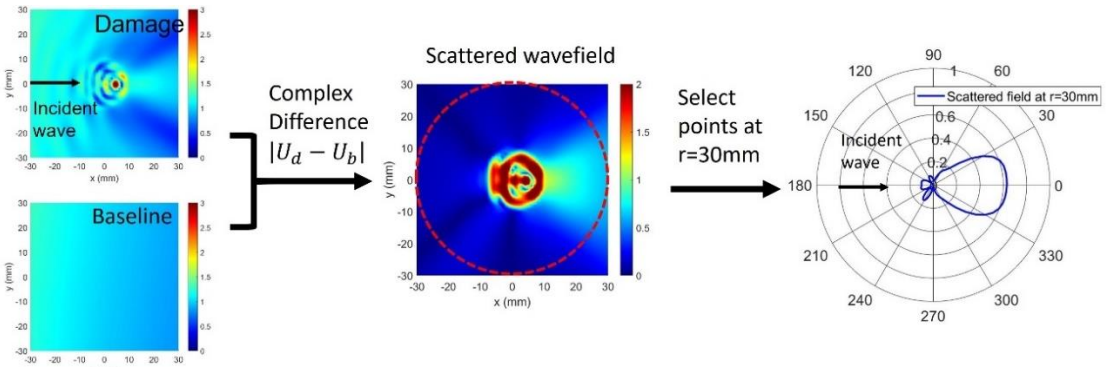

Figure 6-3 Schematic of baseline subtraction analysis used to isolate scattered portion of guided wave amplitude.

The complex FFT magnitude (which includes both phase and amplitude information) for the damage simulation, U_d , and the baseline simulation, U_b, was calculated. These magnitudes can be written in terms of incident wave U_i and scattered wave U_s as follows:

$$U_d = U_s + U_i \tag{6.1}$$

$$U_b = U_i \tag{6.2}$$

Taking the complex difference gives

$$|U_d - U_b| = |U_s + U_i - U_i| = |U_s| \tag{6.3}$$

Where the scattered magnitude U_s is now isolated. This procedure is illustrated schematically in Figure 6-3.

It should be noted that baseline subtraction methods are challenging to implement practically as part of in situ SHM techniques. This is due to requiring good baseline data from the healthy structure, which may not always be available. Variations in environmental conditions (e.g., temperature) can also affect baseline and scattered signals, adding further complexity to the problem. Nevertheless, baseline subtraction methods are a valuable tool for understanding the underlying wave scattering behaviour in a structure and as such are employed throughout this chapter.

6.4 Modelling Attenuation

As mentioned in section 6.1, stiffness proportional (Rayleigh) damping was included in the model to simulate wave attenuation in the composite plate. This section describes how the damping value of β = 30ns was selected. Undamaged plate simulations were created at a range of beta values between 0ns and 90ns. The excitation location was kept the same as in previous simulations. However, a 120mm horizontal line of measurement points was defined along the 0° direction, starting 10mm from the excitation location in 1mm steps.

History outputs of the out-of-plane displacement were recorded and the Hilbert amplitude at each measurement point was plotted for each damping value. The results were compared with experimental line measurements performed on an undamaged region of the plate as described in section 6.1 The fitting procedure described in section 5.2 was used to obtain the values of the attenuation coefficient η and the β values calculated using equation 5.5. Figure 6-4a shows the fitted amplitude curve for experimental measurements and undamaged plate simulations at a range of damping values. The red line indicates the distance of two wavelengths from the transducer, which gives sufficient distance from the source to no longer be in the near field regime and so wave propagation should be fully developed. As an out-of-plane force on a single node was used to generate A_0 mode for the simulations, the near field effects of the transducer will not be accurately modelled in the region before the vertical red line. The fit was performed on the more distant data points (from 30 mm) to obtain a more accurate estimate as shown in Figure 6-4b. Equation 5.5 provided a good fit to both the experimental and simulated data ($R^2 > 0.99$). The β values obtained from fitting the simulation data were within 3% of the expected values, indicating that the fitting procedure was appropriate. A large experimental error was found for the measured attenuation coefficient, which meant that an accurate β value could not be calculated. A visual approach was instead adopted in order to estimate β. One possible explanation for the large error in the attenuation coefficient could be due to variations in the material properties of the plate in the undamaged region causing amplitude data to not be as smooth. Visual inspection of Figure 6-4b indicates that the $\beta = 30$ns simulation provides the closest match to the experimental measurements in the undamaged plate. The simulated values are within 3% of the fitted experimental curve.

Models containing a 20mm circular delamination (depth 0.4mm) with a 60mm grid of measurement points were run for β =10ns, 20ns, 30ns, respectively. The total energy of the signal at each measurement point was plotted along a 60mm horizontal line passing through the delamination, and a circle of points (r = 30mm) centred on the delamination and is shown in Figure 6-5. As shown in Figure 6-5a, good agreement with the experimental results is observed outside

of the delamination region for β=30ns. There is a small variation in amplitude for the other beta values outside of the delamination region (up to 2%) with a greater variation in amplitude (5-20%) on top of the delamination. This indicates that whilst a variation in amplitude is observed at different β values, the precise value of the damping coefficient does not significantly affect the scattering pattern outside of the delamination. Varying the beta value by 10ns produces a 3% change in amplitude outside of the delamination region. Figure 6-5b shows the total energy of the signal around a circle of measurement points (r=30mm) centred on the delamination. Good agreement with experimental results is observed in both the 0° and 180° directions for β=30ns.

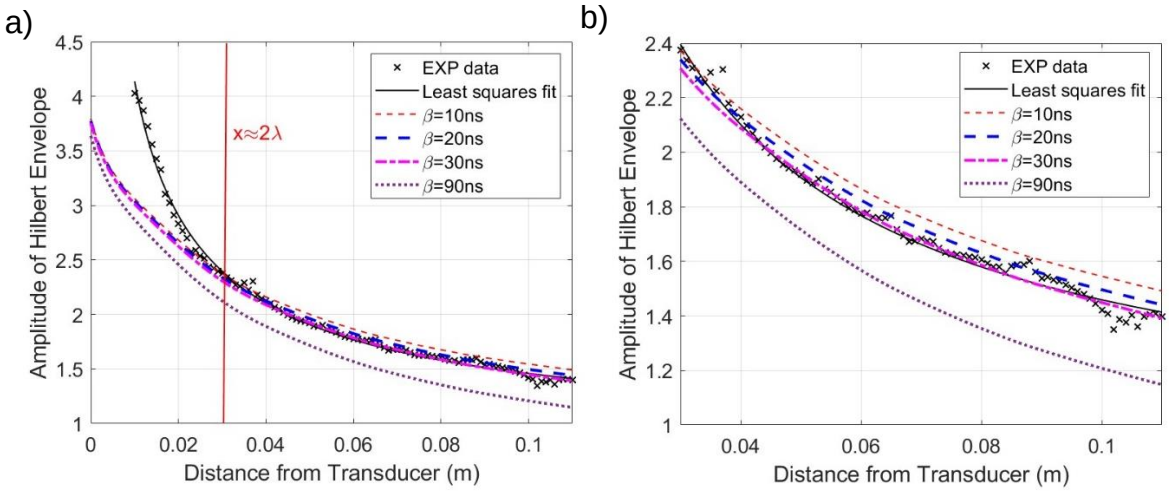

Figure 6-4 Attenuation of Hilbert amplitude with distance from transducer at various damping values. Weighted least squares fit of experimental data is also plotted. a) Full distance range b) Far field region.

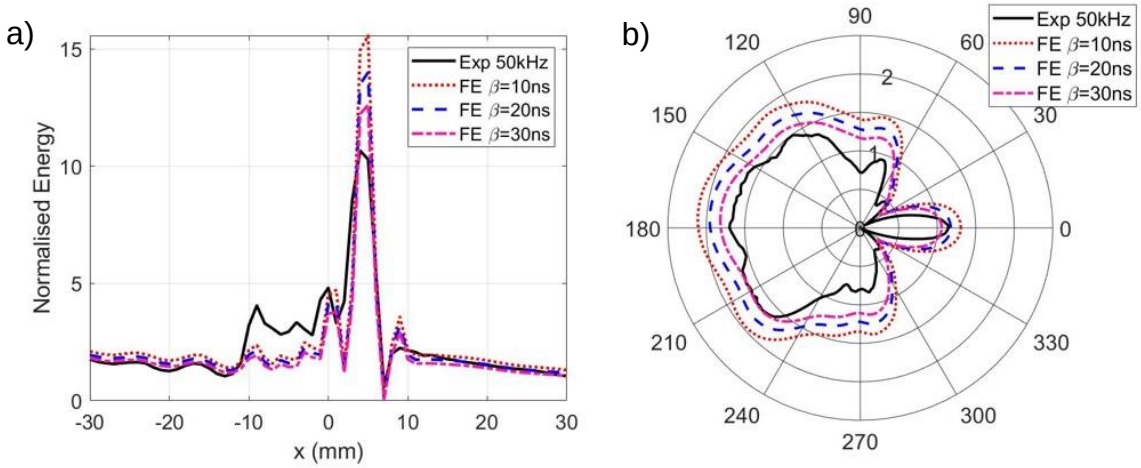

Figure 6-5 Simulated normalised energy at a range of damping values. Experimental measurements plotted: a) horizontal line of points passing through delamination centre (Δx = 1mm); b) circle of measurement points (r = 30mm, Δφ = 2°).

The forward scattered (0°) amplitude shows the best agreement (1%) when β=20ns. However, the amplitudes at β=30ns in all directions are overall closer than for 20ns. Forward and backscattered amplitudes at β=30ns are within 3% of the measured values. As β=30ns shows the closest match for both the undamaged and damaged simulations, it was selected as the best estimate of the attenuation value for further simulations in this study. This value differs from the value β=70ns selected for the unidirectional plate discussed in Chapter 5. Possible causes of this could be due to the different layup of this specimen, different material properties, or could potentially be due to the lower excitation frequency used in Chapter 6.

6.5 Model Convergence

The element size was varied to determine the model convergence. An element size of 0.5mm × 0.5mm × 0.2mm was chosen initially. The thickness of the elements was kept constant at 0.2mm (one element per ply through the thickness), whilst the in-plane dimensions were varied to 0.4mm, 0.3mm, and 0.2 mm respectively. The parameters for the convergence simulations are given in Table 6-1. The delamination was placed at two different depths: between the second and third plies (depth 0.4mm) to match the experimental specimen, and between the fourth and fifth plies (midplane of the plate, depth 0.8mm). A baseline simulation was run for each element size. The simulation time was 0.3ms for all element sizes. Additionally, monitoring points at each node along a 60mm horizontal line passing through the centre of the delamination were implemented.

The magnitude of the FFT at the centre frequency of the signal was extracted for each measurement point. Signals were time gated to remove any edge reflections. The magnitude was then normalised relative to the baseline FFT magnitude at the centre of the defect location (x = 0, y = 0). Figure 6-6 shows the full field of a 40mm × 40mm area centred on the delamination at depth 0.4 mm for each element size. The incident wave propagates from left to right. Similar interference patterns were observed for each element size, but the amplitude of the guided wavefield on top of the delamination showed some variation. The FFT magnitude at 50kHz along a horizontal line (y = 0) of

measurement points for each element size is shown in Figure 6-7a/b. For a delamination located at the midplane of the plate (Figure 6-7a, 0.8 mm depth) the magnitude of the scattered wave is in good agreement to within 5% in front of, and inside, the delamination region for all element sizes, indicating that the model has converged. At delamination depth of 0.4mm (Figure 6-7), the magnitudes of the wavefield outside the delamination area agree to within 5% for all element sizes, indicating that the model has converged for waves propagating outside of the delamination region. However, for the delamination region (x = -10mm to +10mm), whilst the overall scattering pattern and alignment of the peaks is similar between element sizes, the amplitudes of the individual peaks vary in magnitude by up to 45% as the element size is reduced, indicating that the solution has not fully converged in this region. This is likely due to the waves propagating in the thin upper sub-laminate having a shorter wavelength (λ=7mm) than those propagating through the full plate thickness (λ=16mm), and so a smaller element size would be required to achieve full convergence on top of the delamination.

In addition to the interference pattern on top of the delamination, the scattered wave propagating in the undamaged region outside of the delamination area must be considered. Baseline subtraction was performed for a 30mm circle of measurement points in 2° increments.

Table 6-1 Model parameters for convergence simulations.

Element size	Time increment (ns)	No. of elements (million)	Running time (hours)
0.5mm	50	12	4.5
0.4mm	25	18	9
0.3mm	25	32	15
0.2mm	20	32*	20

*0.2mm element size required plate size to be reduced to 400mm x 400mm x 1.6mm due to memory constraints.

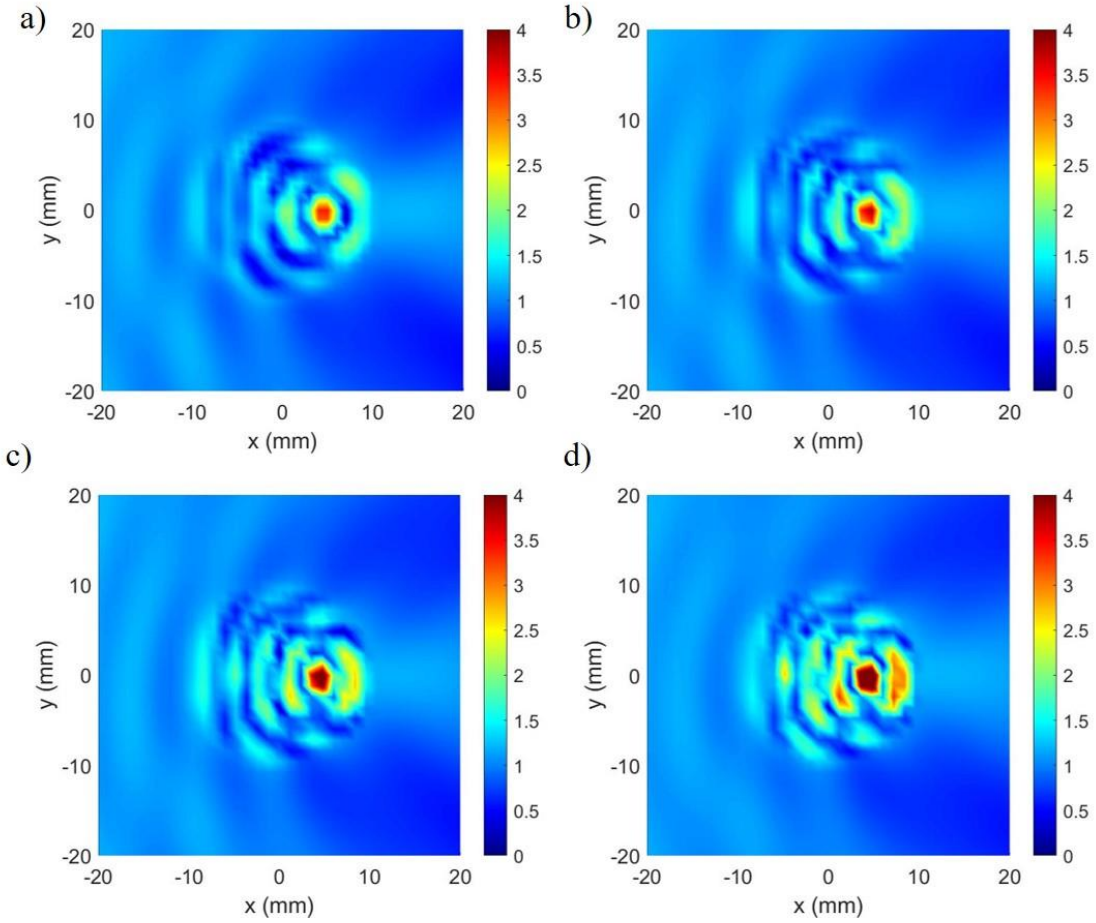

Figure 6-6 Magnitude of FFT at 50kHz for a 40mm x 40mm grid of measurement points centred on a 20mm x 20mm circular delamination; depth 0.4mm. In-plane element size: a) 0.5mm, b) 0.4mm, c) 0.3mm, d) 0.2mm.

The 30mm radius is approximately twice the wavelength of the A_0 mode for the full plate thickness, sufficiently far from the defect to avoid the influence of nearfield scattering effects. Figure 6-7c/d show the angular magnitude of the scattered wave at delamination depths 0.8mm and 0.4mm respectively. At both delamination depths there is a large lobe around the 0° direction (+/-30°), indicating significant forward scattered amplitude. The amplitude is highest in the 0° direction and reduces towards the 30° direction, consistent with results in literature [95,113,120]. The magnitudes are in agreement to within 5% for all element sizes at each depth, indicating that the model has converged in the undamaged region outside of the delamination. Despite significant variation in peak magnitude, the qualitative features of the scattering on top (e.g., location of the peaks) of the delamination at 0.5mm element size reasonably match that of the smaller element sizes.

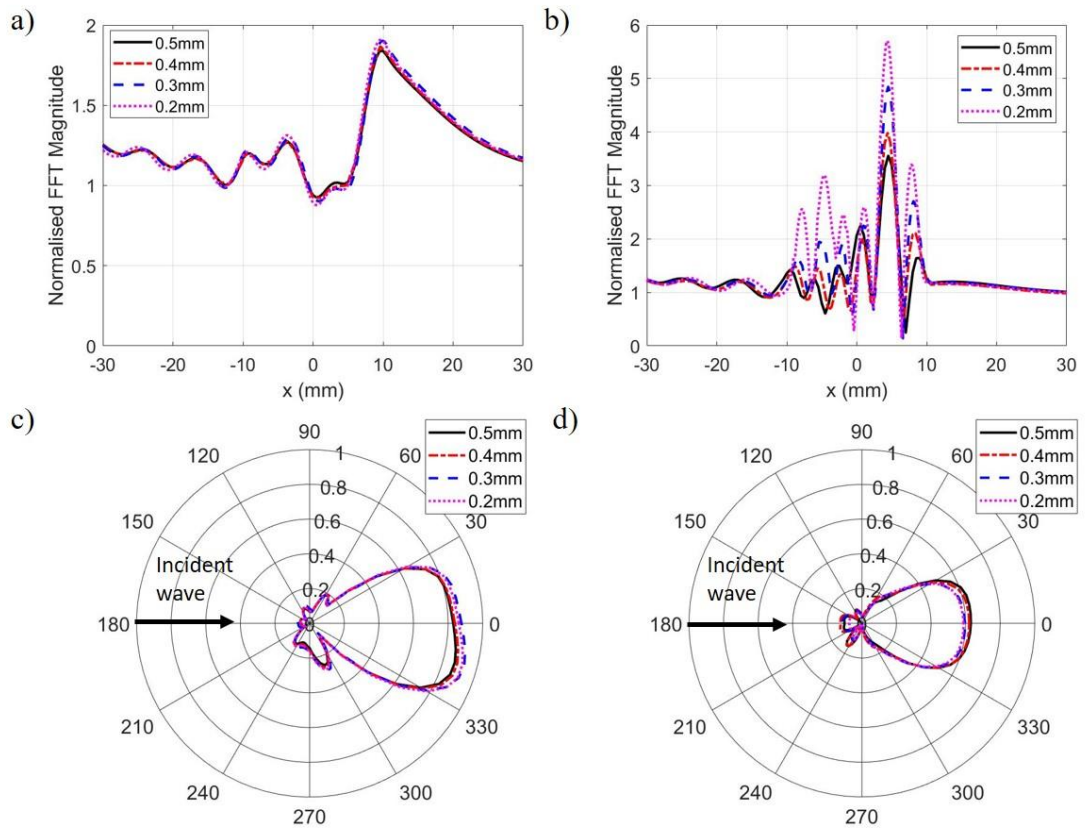

Figure 6-7 Normalised FFT magnitude (50 kHz) for different element sizes along a 60mm horizontal line of monitoring points for delamination depths: a) 0.8mm, b) 0.4mm. Magnitude of baseline subtracted scattered wave for different element sizes for delamination depths: c) 0.8mm, d) 0.4mm.

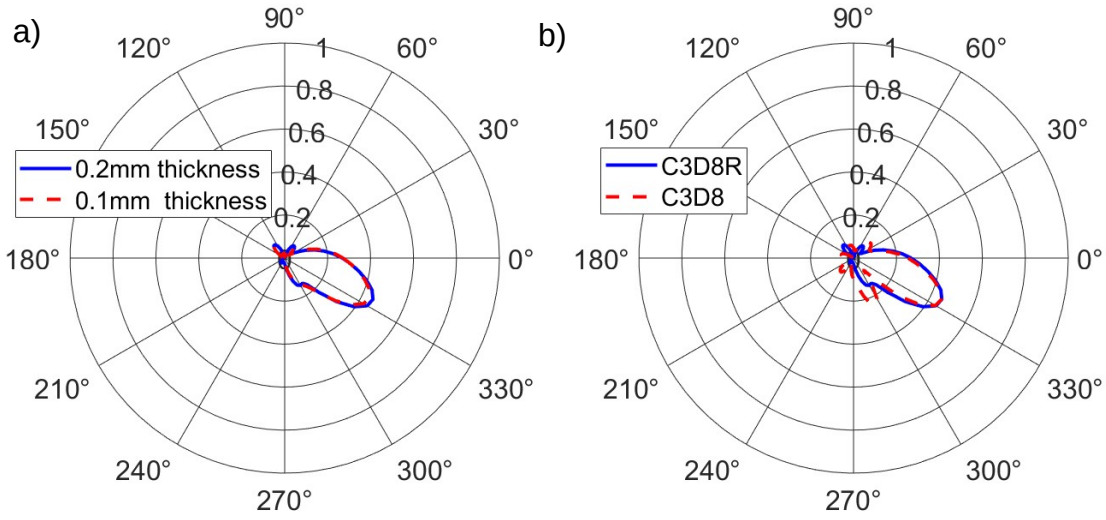

Figure 6-8 Isolated scattered wave at 50kHz (baseline subtraction) for a 0.2mm depth delamination: a) comparison between element thicknesses; b) comparison between element types.

In addition to the in-plane dimensions of the elements, the number of elements through the thickness per ply layer and the element type can also affect the numerical accuracy and hence the model convergence. To ensure that these parameters did not have a significant effect on the scattered wave, a model with a 0.2mm depth delamination was created with one element (0.2mm thickness) and 2 elements (0.1mm thickness) per ply layer respectively. Additionally, a 0.2mm depth delamination was modelled with C3D8 elements (1 element thickness per ply layer). In this case, the delamination was placed at a depth of 0.2mm as this gives the thinnest sub-laminate, and hence models the smallest possible wavelengths occurring in the plate. The baseline subtracted amplitudes are shown in Figure 6-8. It can be observed that employing a thinner element thickness (Figure 6-8a) or different element type (Figure 6-8b) has limited effect on the pattern of scattered waves propagating away from the delamination, hence an element thickness 0.2mm was employed for subsequent simulations in this study. It should be noted that employing a smaller element size in the thickness direction or changing the element type was found to affect the interference pattern on top of the delamination. However, in the context of SHM of composite structures, modelling the precise scattering behaviour on top of the delamination is of less interest, as usually the aim of guided wave testing is to detect and quantify the scattered wave at some distance from the damage, so that damage can be localized. Therefore, in this study the focus was placed on accurately modelling scattered waves. For an element size of 0.5mm the model has sufficiently converged (within 1% and 3% of 0.4mm and 0.2mm amplitudes respectively) to model scattered waves propagating away from the damage in the undamaged (full thickness) region of the plate. Therefore, an element size of 0.5mm x 0.5mm x 0.2mm was selected for the further simulations presented in this study.

6.6 FE Model Validation

The ultrasonic C-scan results in [151] indicated that the artificial delamination has a slightly oval shape with a best estimate of 20mm length in the x-direction and 16mm width in the y-direction. The magnitude of the FFT at 50 kHz over a 40mm x 40mm grid, horizontal line, and 30mm circle for an oval 20mm x 16mm shape and a circular 20mm x 20mm case were compared with the experimental measurements.

An increase in FFT magnitude within the delamination region can be observed in both the 20mm x 16mm and 20mm x 20mm models (Figure 6-9b/c respectively). The delamination shape affects the shape of the high magnitude region. This effect could potentially be used to estimate delamination size from noncontact laser measurements. The predicted increase in magnitude relative to the surrounding regions is slightly lower for the numerical results than observed in the experiment. The forward scattered component can be observed in each of the simulations, but the drop in amplitude in the shadow regions either side of the forward lobe is lower than for the measurements. The scattering pattern on top of the 20mm x 16mm delamination matches the experimentally measured pattern more closely than the 20mm x 20mm circular defect, indicating that the delamination width affects the interference pattern on top of the defect.

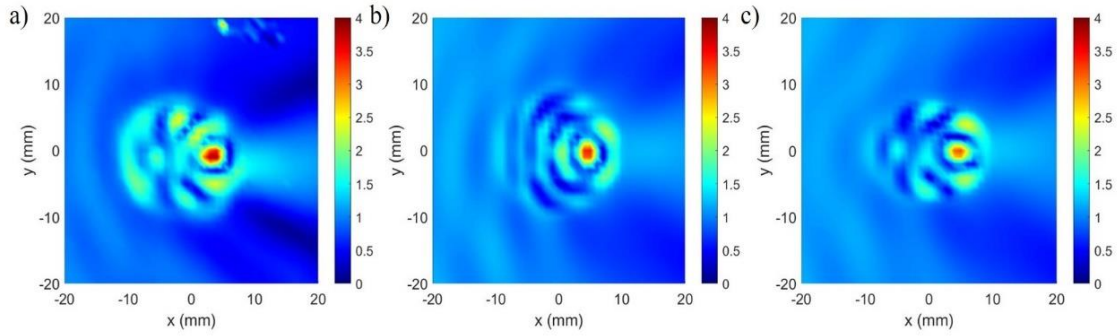

Figure 6-9 Normalised magnitude of FFT at 50kHz over a 40mm x 40mm grid of measurement points for a) experimental measurements; b) FEA 20mm x 20mm delamination; c) FEA 20mm x 16mm delamination.

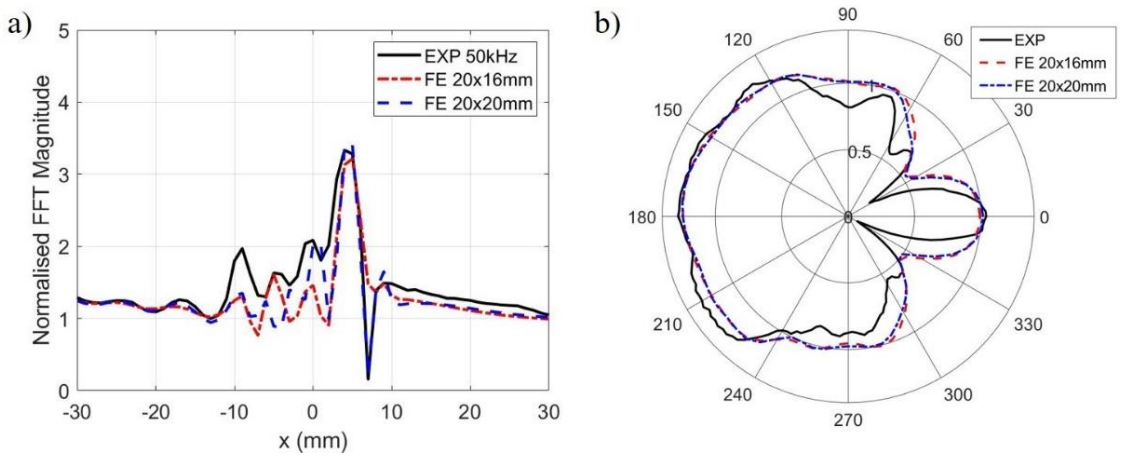

Figure 6-10 Measured and simulated magnitude of FFT at 50kHz for a) 60mm line of measurement points in 1mm steps, passing through the centre of the delamination; b) circle of measurement points with radius 30mm (2° steps) centred on the delamination.

The measured FFT magnitude along a horizontal line of measurement points is denoted by the black line in Figure 6-10a. The magnitude decreases along the propagation direction until a sharp increase in magnitude is observed at the front edge of the delamination (x = -10mm), consistent with the full field scan in Figure 6-9a. The decrease in magnitude with propagation distance is expected due to wave spreading and attenuation. The variation in magnitude in front of the delamination occurs due to constructive and destructive interference with the backscattered wave. On top of the delamination, there are several amplitude peaks, with the highest peak at +4mm and a trough at +7mm. The forward scattered amplitude beyond 10mm is larger than that of the incident wave.

The wave amplitude for the FE simulation of the circular 20mm x 20mm delamination is denoted by the blue line in Figure 6-10a. The incident wave, the peak at +4mm and trough at +7mm show good agreement with the measured values, to within 3%. However, the overall magnitude on top of the delamination and the forward scattered wave is lower than in the experiment. The incident wave for the 20mm × 16mm delamination model (red line Figure 6-10a) has reasonable agreement within 9% of the measured values. The location of the major peak is in good agreement, however the trough at the edge of the delamination is not visible. Again, the magnitude on top of the delamination, and of the forward scattered wave, are lower than the measurements. In contrast to the 20mm x 20mm delamination, the location of the peaks within the

delamination region of the 20mm x 16mm model matches the experiment reasonably well. These results suggest that the interference pattern on top of the delamination is strongly influenced by the size and shape of the delamination, but that the forward and backward scattered waves are less sensitive to the exact defect shape.

The angular FFT amplitude of the scattered wave outside the damage area for the experiment (black), 20mm x 20mm delamination model (blue), and 20mm x 16mm delamination model (red) around a circle of measurement points with radius 30mm is shown in Figure 6-10b. The measurements show a strong lobe in the 0° direction, consistent with the forward scattered wave observed in the full field measurement in Figure 6-9a. A steep drop in amplitude is observed at 30° and 330°, corresponding to the location of the regions of destructive interference in the measured full wavefield. The forward scattered amplitude is generally lower than the amplitude in the backscattered direction. The scattering pattern is reasonably symmetric.

The scattering patterns for the modelled delamination shapes agree with each other to within 3%, which suggests that delamination shape does not significantly influence the scattering pattern outside of the delamination. The magnitude of the scattered wave in the 0° and 180° directions agrees with the measurements to within 3% for the 20mm x 20mm delamination, and 5% for the 20mm x 16mm delamination. The forward scattered lobe is observed in the models, but the overall shape differs from the measurements. Two regions of lower amplitude are observed at 35° and 325° for both delamination sizes. However, the reduction in amplitude is not as strong as observed in the experiments, consistent with the full field results in Figure 6-9. Overall, the FE results show good agreement with the experimental measurements, although certain features, such as the forward scattered lobe, were less distinct. It has been demonstrated that the interference pattern on top of the defect is strongly influenced by delamination shape and size, whereas the scattered wave around the delamination is similar for the considered cases.

6.7 Summary and Conclusions

Guided wave propagation and scattering at an ellipse or circular shaped delamination in a quasi-isotropic composite laminate has been investigated through experiments and FE simulation. The artificial delamination was located asymmetrically through the full thickness of the plate. Full field non-contact laser measurements verified the wave trapping phenomena with increased amplitude on top of the delamination and visualised the forward scattered wave and shadow regions behind the defect. A full 3D layered FE model containing a zero-volume delamination was developed and showed good agreement with the experimental results. The attenuation of the specimen was estimated through comparison of experimental and simulated amplitudes with different damping coefficients. The convergence of the model was investigated by varying element size and good convergence was observed in the undamaged laminate outside of the delamination region. Inside the delamination significant amplitude variation was observed between element sizes, however the qualitative location of the peaks showed good agreement. This was adequate to accurately model scattered waves propagating away from the damage in the undamaged part of the composite specimen, which is of more interest in a SHM context.

7 Anisotropy Influence on Guided Wave Scattering in a Quasi-isotropic Laminate

Many SHM techniques, such as sparse array imaging, rely on prior information of the scattering characteristics at different damage types. However, anisotropic wave propagation effects add a layer of complexity to the guided wave scattering, which has not been studied widely. This Chapter presents the results of parameter studies using the model developed in Chapter 6, which have already been published in two journal articles [57,169]. The influence of delamination shape, size, and depth on scattering is determined through numerical simulations. Building on the work on wave propagation in anisotropic materials presented in Chapter 5, the influence of anisotropy on guided wave scattering at a delamination is investigated by varying the incident wave propagation direction in both the experiments and FE models. Scattering behaviour around a delamination is compared to that of a permanent magnet target. 2D scattering matrices are calculated for both the delamination and the permanent magnet and implications for structural health monitoring are discussed.

7.1 Influence of Delamination Size/Shape

Delamination shape and size were varied systematically for the FE simulations. Circular delaminations with diameters 16mm-22mm in 2mm steps were modelled. Several ellipse-shaped delaminations were also modelled with dimension in the range of 16mm-22mm. Figure 7-1 shows the 2D wavefield images for four selected size cases: 16mm circle, 18mm circle, 22mm x 16mm ellipse, and 22mm x 18mm ellipse. For the circular delaminations in Figure 7-1a/b the area of increased amplitude changes with delamination size. The same can be observed for the ellipse-shaped delaminations in Figure 7-1c/d. A 2mm change in one dimension of the ellipse-shaped delaminations has a significant effect on the scattering pattern on top of the delamination. The horizontal line and circular scans for each damage case are shown in Figure 7-2. The horizontal scans show significant variation in peak location between the different delamination sizes, which is consistent with the wave trapping

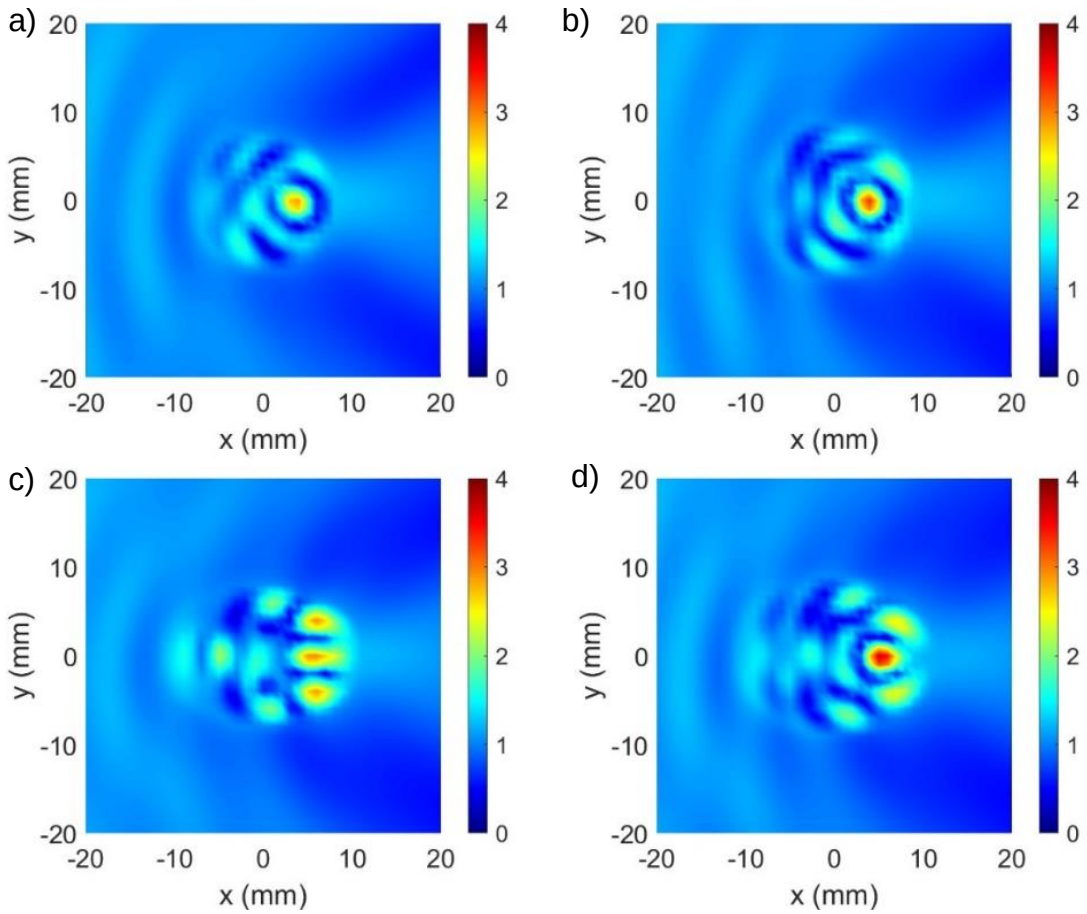

Figure 7-1 Normalised magnitude of FFT at 50kHz over a 40mm x 40mm grid of measurement points for a) 16mm circular delamination; b) 18mm circular delamination; c) 22mm x 16mm delamination; d) 22mm x 18mm delamination. Obtained from FE model.

patterns shown in Figure 7-2. Additionally, there appears to be no clear correlation of maximum trapped amplitude and delamination size. In contrast, the circular scans are almost identical between each shape. These results indicate that energy trapping on top of the delamination could be used to estimate the size and shape of the delamination. However, the scattered wave around the delamination is not significantly affected by small changes in delamination size.

Previous work has indicated that the scattered wave shows sensitivity to larger variations in delamination size [95,113]. Murat et al. considered the scattered amplitude around delaminations of different sizes. The size changes were of the order of 10mm rather than the 2-4mm presented here. Backscattered amplitudes were found to be similar across delamination sizes, similar to the

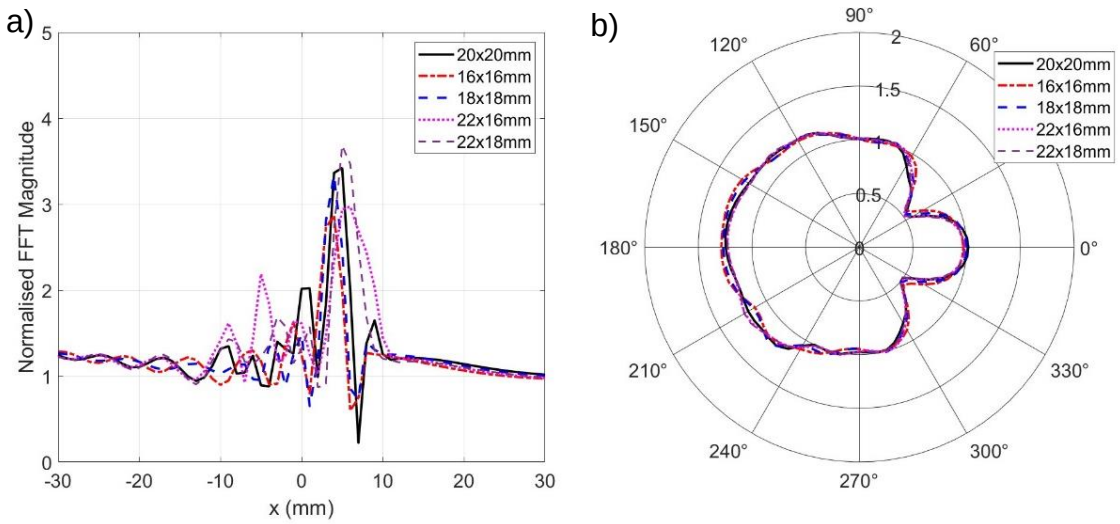

Figure 7-2 Delamination shape and size variation. Normalized FFT magnitude along a) horizontal line across delamination, b) 30mm circle of measurement points. Obtained from FE model.

results presented in Figure 7-2, which is expected as backscattered waves will not have entered the delamination region and so will not be influenced by delamination size. However significant variation in forward scattered amplitudes was observed for the delaminations of different sizes [156]. This is because a larger change in delamination length will cause a greater change in the interference between the waves in the sub-laminates as they recombine, resulting in a larger variation in amplitude than observed for the smaller size changes in Figure 7-2.

7.2 Influence of Delamination Depth

The depth of a 20mm x 20mm circular delamination was systematically varied in 0.2mm increments (between each ply layer) and the scattering of the A_0 mode was simulated. The full field amplitudes over a 40mm × 40mm grid are shown for each delamination depth in Figure 7-3. For a delamination at depth 0.2mm (Figure 7-3a) a low amplitude region is observed over the delamination location, in contrast to most reports in literature [115]. A thin sub-laminate has a lower bending stress, so the amplitude of trapped waves on top of the delamination was expected to be high at 0.2mm delamination depth. At delamination depth 0.4mm (Figure 7-3b), the amplitude of the scattering pattern on top of the delamination is higher, as observed previously and in line with literature [115].

When the delamination is located at 0.6mm depth (Figure 7-3c) some wave trapping on top of the delamination can be observed, although the scattering pattern is not as symmetrical as observed at 0.4mm depth. The forward scattered component can be observed between the 0° and +45° directions. The ply layup of the top sub-laminate at 0.6 mm depth is asymmetric (−45°/+45°/90°) which could contribute to the steering of the forward scattered wave. At the mid-plane of the plate (0.8mm depth, Figure 7-3d) almost no wave trapping on top of the delamination, but the highest 0° forward scattered component, are observed. A scattered component either side of the 0° wave can be observed (approximately +/−45° directions), although the amplitudes of the additional components are much lower. At the remaining delamination depths (Figure 7-3e/f/g) only very limited wave trapping on top of the delamination is observed. This is likely due to the monitoring points being located on the opposite side of the plate to the thinner sub-laminate, where the higher amplitude reflections are observed. The amplitude outside of the delamination region at these depths indicate that the scattering outside of the delamination is similar at symmetric delamination depths.

The low amplitude observed on top of the 0.2mm depth delamination indicates that the elements in this region are behaving too stiffly. As the upper sublaminate is very thin for this delamination depth, this means that the A_0 mode has an even shorter wavelength in this region, so it was initially thought that this problem was due to poor model convergence on top of the delamination. The in-plane element size was reduced in 0.1mm increments to 0.2mm and was investigated for 0.2mm and 0.1mm element thickness (1 or 2 elements per ply layer), however the same low amplitude phenomena was observed for each case. C3D8 elements were then investigated, as it was thought that the reduced number of integration points of the C3D8R element could be causing increasing the numerical error, resulting in the low amplitude on top of the delamination. The 0.2mm and 0.4mm delamination depth models were rerun with C3D8 elements. The 2D wavefield plots for each element type and depth are shown in Figure 7-4.

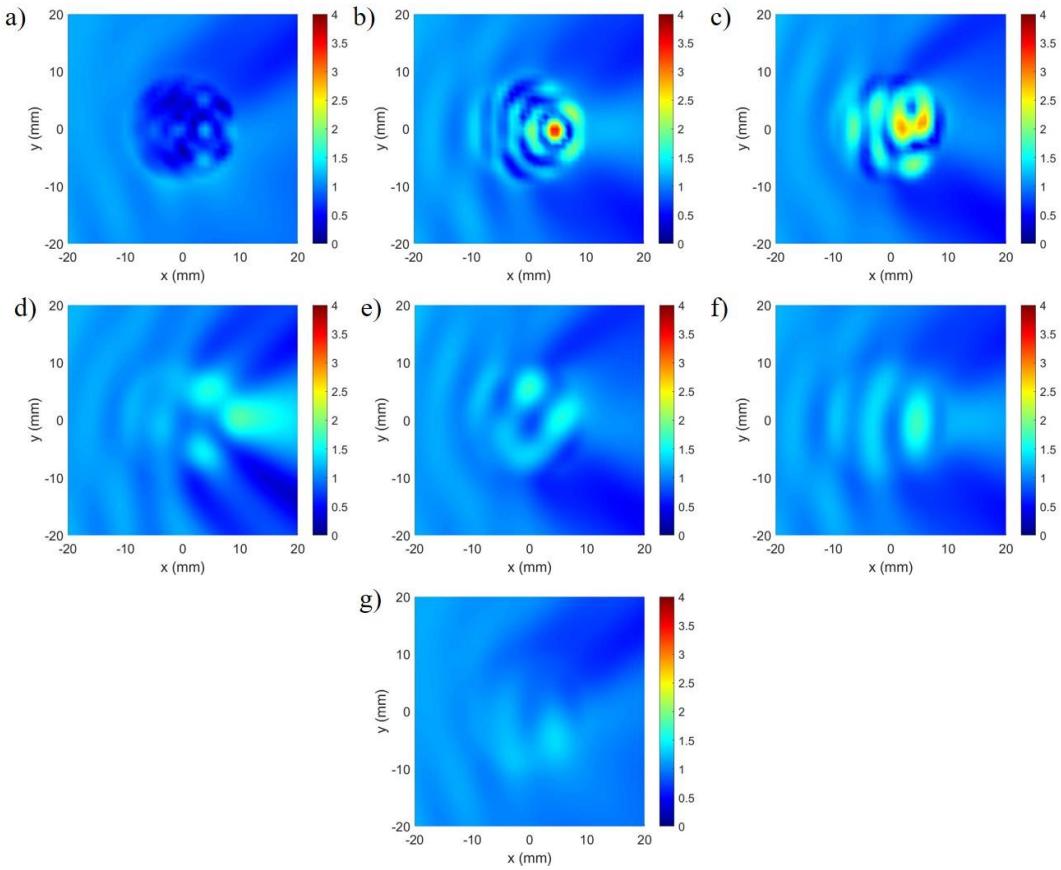

Figure 7-3 Normalised scattered wave amplitude (FFT at 50 kHz) for 20mm x 20mm circular delamination at range of delamination depths: a) 0.2mm; b) 0.4mm; c) 0.6mm; d) 0.8mm; e) 1.0mm; f) 1.2mm; g) 1.4mm. Obtained from FE model.

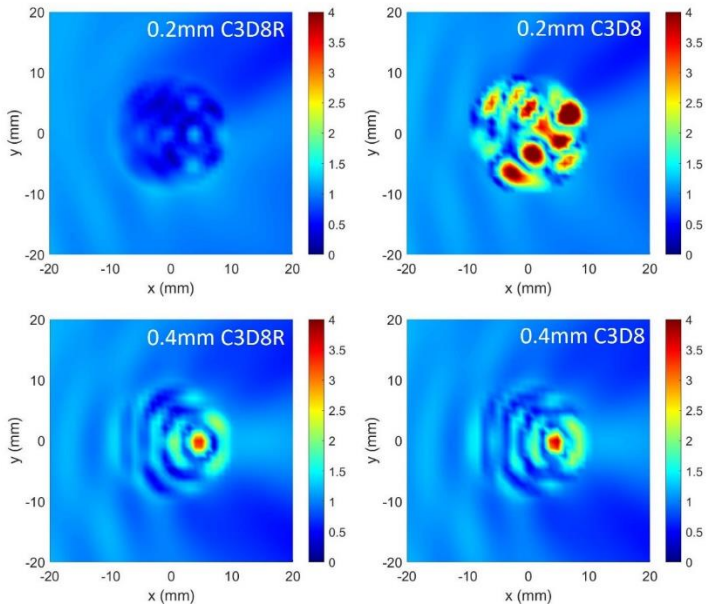

Figure 7-4 Normalised wave amplitude (FFT at 50kHz) for 20mm circular delamination for different depths and element types; a) 0.2mm delamination depth C3D8R, b) 0.2mm depth C3D8; c) 0.4mm depth C3D8R; d) 0.4mm depth C3D8.

As seen in Figure 7-4b a region of high trapped amplitude can be observed for the 0.2mm depth delamination which is more representative of the expected wave behaviour in literature [115]. As discussed in section 6.5 changing the element type had limited effect on the directivity and amplitude scattered wave propagating away from the damage. For the 0.4mm depth delamination, changing the element type had limited effect on the wave trapping pattern in the upper sublaminate. As the rest of the simulations in this study are performed for an 0.4mm depth delamination, C3D8R elements were implemented for these cases.

In order to determine the influence of delamination depth on the scattering outside of the delamination, a baseline subtraction analysis was performed to determine the magnitude of the scattered wave on a 30mm circle centred on the delamination. Figure 7-5 compares the scattered wave for delaminations located at symmetric depths. Each pair of symmetric delamination depths has

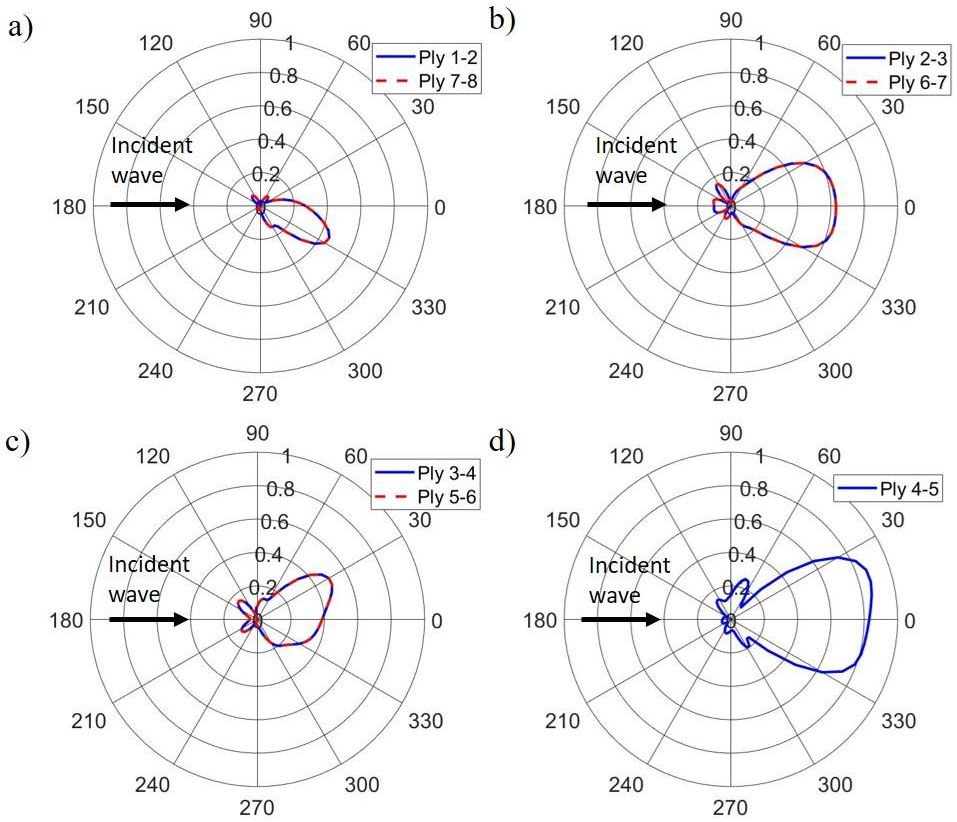

Figure 7-5 Scattered wave around a 30mm circle of measurement points, obtained via baseline subtraction. Symmetric delamination depths plotted together: a) ply 1-2 (0.2mm) and ply 7-8 (1.4mm) b) ply 2-3 (0.4mm) and ply 6-7 (1.2mm) c) ply 3-4 (0.6mm) and ply 5-6 (1.0mm) d) ply 4-5 (0.8mm – midplane).

an identical scattered wave pattern outside the delamination area, as expected. This is because the scattering pattern depends on the thickness of the sub laminates. Figure 7-5a shows a narrow lobe (approximately 0.4 of the amplitude of incident wave) directed towards the 330° direction for delamination depths 0.2mm and 1.4mm, likely due to energy focusing along the fibres of the outer −45° direction plies. At delamination depths 0.4mm and 1.2mm (Figure 7-5b) a symmetric lobe in the 0° direction is observed, with a higher amplitude than the 0.2mm and 0.6mm cases, which could be due to the symmetric layup of the top sub-laminate (+/−45° direction). Increasing the delamination depth to 0.6mm or 1.0mm generates a lobe with the highest amplitude in the 30° direction. The highest amplitude of the scattered wave occurs for a delamination at the midplane of the plate (Figure 7-5d). Constructive interference due to the symmetric sub-laminae could contribute to the higher amplitude.

The results presented in Figure 7-5 indicate that the delamination depth and ply lay-up of the sub-lamina influence the direction of scattered waves outside of the delamination. The scattered wave can therefore be used to determine two possible through thickness locations of the delamination. At all delamination depths the backscattered amplitude is small, which suggests that a pulse-echo detection approach for SHM of the composite plate would have limited sensitivity. For a pitch-catch approach, the forward scattered wave shows a counterintuitive increase in amplitude behind the delamination rather than the often-expected decreased amplitude behind the damage. The pitch-catch approach could be more reliable for detecting delaminations, but care must be taken, as the direction of the forward scattered lobe may differ from the incident wave propagation direction.

7.3 Influence of Excitation Frequency

Full field measurements, line scans, and circle scans were obtained at the higher excitation frequency of 75kHz ($\lambda = 18\text{mm}$). FEA was performed at this frequency for the standard 20mm x 20mm delamination in addition to the 20mm x 16mm delamination. All other parameters were kept the same as for the 50kHz ($\lambda = 26\text{mm}$) models. The measured magnitude of the FFT at 75kHz is presented in Figure 7-6a. As for the 50kHz results, a region of

increased amplitude can be observed over the delamination region. More regions of high and low amplitude can be observed in the interference pattern on top of the delamination, in comparison to the 50kHz scan (Figure 6-9a). The scattering patterns on top of the delamination are related to the ratio between the wavelength of the A_0 mode and the length of the delamination. At 75kHz the A_0 mode wavelength is 30% shorter than at 50kHz this creates the additional regions of high and low amplitude on top of the delamination.

The 'tail' produced by the forward scattered wave (0° direction) is present at 75kHz, although it is narrower and lower in amplitude than that observed at 50kHz. Two shadow regions can be observed either side of the forward scattered wave. Additional scattering and shadow regions can be observed either side of the forward scattered wave, although these lobes have much lower amplitude. The additional scattering is approximately in the -45° and +45° directions, which correspond to the fibre orientation present in the top sub-laminate. The scattering pattern on top of the delamination is reasonably symmetric, but the scattered wave outside of the delamination is not perfectly symmetric.

Figure 7-6b/c show the modelled full field FFT for the 20mm x 16mm delamination, and 20mm x 20mm delamination, respectively. Increased amplitude is again observed in the delamination region, and the scattering pattern on top of the delamination contains more regions of high and low

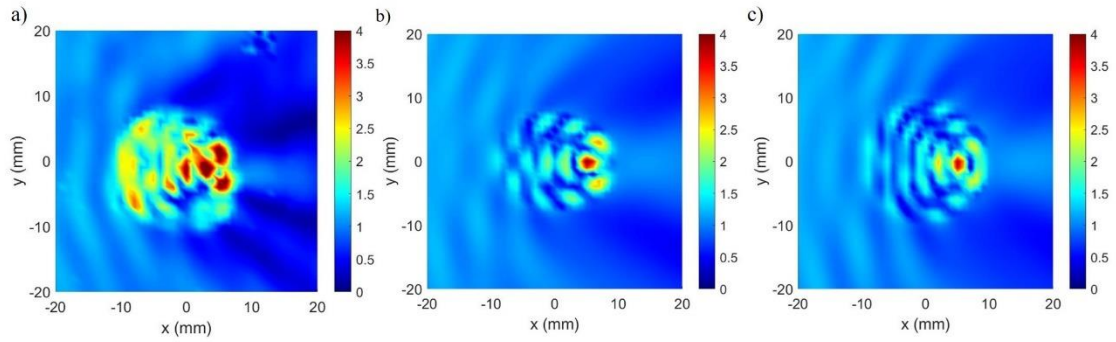

Figure 7-6 Normalised magnitude of FFT at 75kHz over a 40mm x 40mm grid of measurement points for a) experimental measurements b) FEA 20mm x 16mm delamination c) FEA 20mm x 20mm delamination.

amplitude, spaced closer together than observed at 50kHz. The width of the delamination influences the scattering pattern on top of the delamination. The modelled amplitude at the entrance of the delamination is much lower than observed in the experimental measurements. A forward scattered wave is present; however, the shadow regions are not as pronounced as in the measurements and the additional shadow regions are not present in the FE results for either delamination shape. At 75kHz there is a greater difference between experiment and simulation than observed at 50kHz. This is because, even though the wavelength is shorter at 75kHz, the results in Figure 7-6 were produced with the same element size at 50kHz. Therefore, a greater numerical error is expected for the 75kHz results.

The magnitude of the FFT along a horizontal line is shown in Figure 7-7 for the experimental measurements, 20mm x 20mm delamination and 20mm x 16mm delamination respectively. Increased amplitude is observed within the delamination region, consistent with the scanning results in Figure 7-6a. The amplitude of the forward scattered wave is overestimated by the FE model; however, each delamination shape produces a similar forward scattered amplitude. The interference between the incident and backscattered wave for the 20mm x 20mm delamination matches the experiment more closely than the 20mm x 16mm delamination, as seen at 50kHz. This interference is also more visible at 75kHz than at 50kHz.

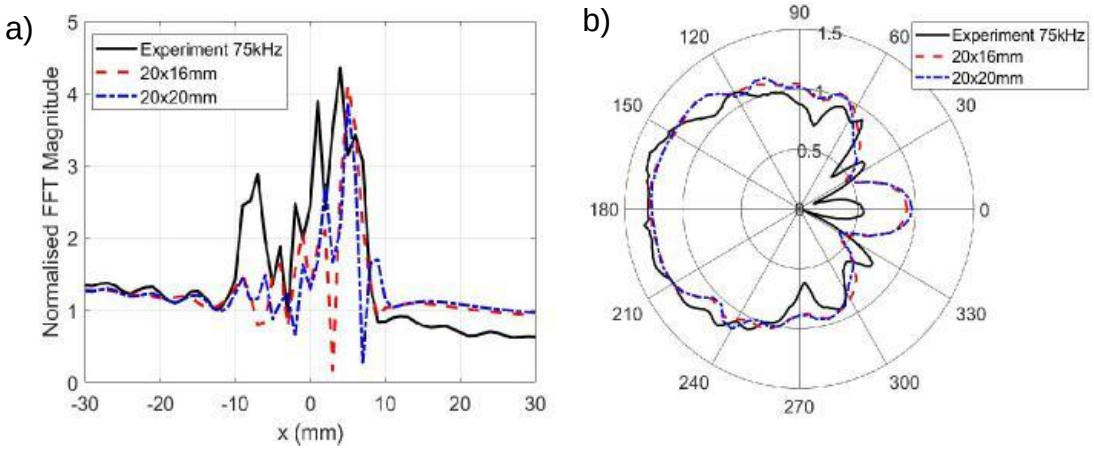

Figure 7-7 Measured and simulated magnitude of FFT at 75kHz for a) 60mm line of measurement points in 1mm steps, passing through the centre of the delamination; b) circle of measurement points with radius 30mm centred on the delamination (2° steps).

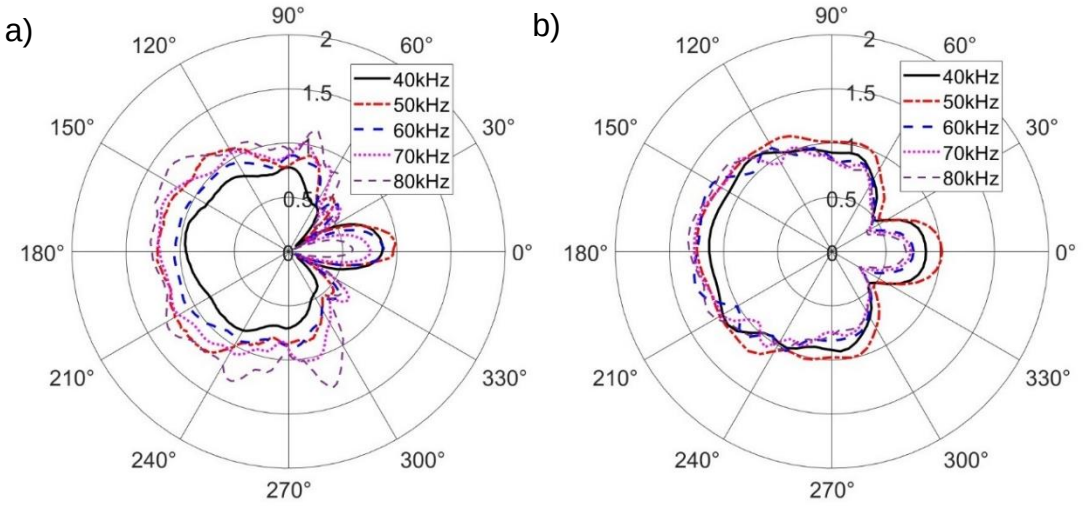

Figure 7-8 a) Measured and b) simulated guided wave amplitude at various frequencies for a 20mm circular delamination at depth 0.4mm.

Whilst some of the peaks in the delamination region are aligned with the experimental measurements, the majority do not and the amplitude on top of the delamination is generally lower for the FE results than observed in experiment.

Considering the circular scans, presented in Figure 7-7b, the measured forward scattered lobe is narrower and has a much lower amplitude at 75kHz than at 50kHz, as expected from the 2D scans in Figure 7-6. This change in magnitude is due to superposition of the waves in the upper and lower sub-laminates recombining to form the forward scattered component. The frequency has changed the A_0 mode wavelength and subsequently phase difference of the waves travelling in each sub-laminate has also changed, resulting in the difference in forward scattered amplitude. The forward scattered lobe in the simulated results overpredicts the forward scattered amplitude, consistent with the horizontal line results in Figure 7-7. Again, the two delamination cases produce almost identical wave amplitudes outside of the delamination, further indicating that scattering of the A_0 mode is not significantly influenced by small changes in delamination size and shape.

To investigate the effect of different excitation frequencies on the magnitude of the forward scattered wave, circular measurements were performed around the delamination at frequencies between 40 - 80kHz in 10kHz increments and are shown in Figure 7-8a. FE models of a 20mm circular delamination were also

created for each excitation frequency and the amplitude around a 30mm circle of points are presented in Figure 7-8b. All other model parameters were kept the same as for the 50kHz case. The excitation frequency has a significant effect on the experimentally measured forward and back scattered amplitudes. The normalized forward scattered amplitude initially increases with amplitude but then decreases with increasing frequency from 60kHz onwards. This is again due to the waves in each of the sub-laminates changing relative phase as the wavelength of the incident wave is varied with wavelengths ranging from 17-30mm. The FE forward scattered amplitude amplitudes in Figure 7-8 also vary with excitation frequency; however, the backscattered amplitudes are more consistent than observed in the experiments. In the experimental scans there is much more variation with frequency of the forward scattered wave at 60-80kHz than observed for the FE results. As seen in Figure 6-10 (50kHz) and Figure 7-7 (75kHz) a steep drop in amplitude either side of the forward scattered lobe is observed for the experimental results at each excitation frequency, however this is again much less pronounced in the simulation results.

7.4 Influence of Anisotropy/Incident Wave Direction

The results of the parameter studies in sections 7.1, 7.2, and 7.3 have focused on guided wave scattering for a single incident wave direction. The influence of anisotropy on the amplitude and direction of guided wave scattering was considered for a 20mm circular delamination at depth 0.4mm and 0.8mm. The delamination scattering results was compared to that of a magnet target and 2D scattering matrices were calculated for each damage case.

The variation of incident wave amplitude with propagation direction around one of the transducers was investigated first. The wave amplitude (magnitude of FFT at centre frequency 50kHz) was calculated on a circle for both experiment and simulation and is shown in Figure 7-9. Increased amplitude can be observed in the +/-45° directions, corresponding to the fibre directions of the outer ply layers of the laminate. This indicates that wave energy is focused along the outer ply layers, where there is more energy concentration of the A_0 mode due to the higher bending stress, consistent with results reported in literature [105,113]. Despite the quasi-isotropic stacking sequence, the strong

directivity in the +/-45° directions means that the incident wave propagation for this particular layup (8 plies) is more similar to that of a cross-ply plate. The experimental measurements show similar increased amplitude in the +/-45° directions (approximately factor 2), however the pattern is not as symmetric as the FE results and there is approximately 10% variation between measured and predicted amplitudes in the 225° and 315° directions. This could be influenced by the lack of uniformity of the coupling of the PZT to the plate, or potential local variations in the material properties, while the FEA results are idealized and therefore perfectly symmetric. An additional peak in the 90° direction can be observed in the experiments, which is likely due to the connection between the wire and wrap-around electrode at this orientation. Overall, the undamaged plate FE simulation shows reasonable agreement with the experimental measurements. The incident (excited) wave for this composite layup is directionally dependent and therefore anisotropy needs to be considered when studying scattering around damage.

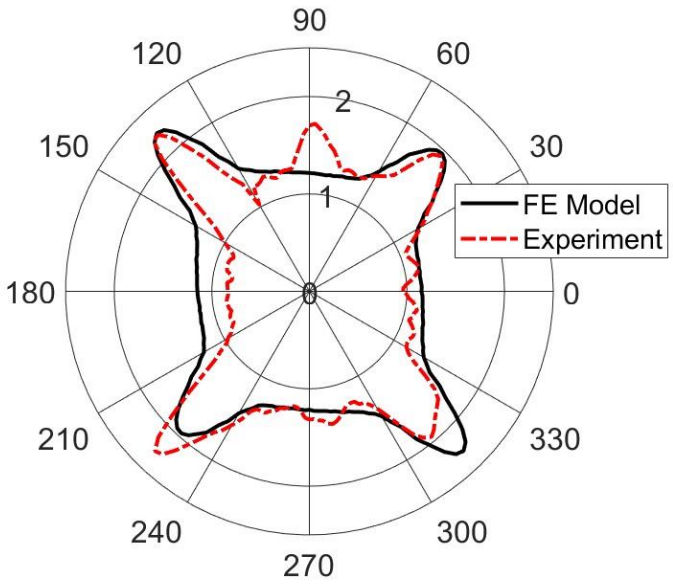

Figure 7-9 Measured and FE simulated normalized FFT magnitude at 50kHz around excitation (80mm radius circle, 2° increments), undamaged composite laminate.

7.5 Scattering Around a Delamination

The guided wave scattering at a delamination for multiple incident wave directions was investigated. The 2D wavefield images in Figure 7-10 show the FFT magnitude at 50kHz for a 40mm x 40mm grid centred on top of the circular delamination region (approx. 20mm diameter) for incident wave directions 0°, 90°, -45°, and +45°, respectively. All simulation amplitudes were normalized with respect to the amplitude of the incident wave in the 0° direction at the plate centre (0mm, 0mm) obtained from the baseline simulation. Experimental amplitudes were normalized with the same factor for three of the PZTs, as an estimate of the incident wave amplitude in the 0° direction. For one incident wave direction (+45°) the measured amplitude was approximately 20% lower, likely due to the coupling of that PZT disc to the plate, and therefore was normalized with a different factor. The normalization factors were applied to the amplitudes for both the 2D scattering images (Figure 7-10), and the polar plots (subsequent figures).

Each of the experimental scans shows trapped amplitude on top of the delamination and a forward scattered component with shadow regions either side. However, as seen in section 6.6, the shadow regions are not observed that clearly in the FE results, and no forward scattered component is visible in the 90° direction FE simulation (Figure 7-10b). Higher trapped and forward scattered amplitudes are observed for the diagonal incident wave directions (-45° direction (Figure 7-10c/g), +45° direction (Figure 7-10d/h)), compared to the 0° and 90° incident directions. The highest amplitude observed for the -45° incident wave direction corresponds to the fibre orientation of the outermost ply layer of the laminate, with +45° corresponding to the second plies. This indicates that energy is being focused along the outer ply layers.

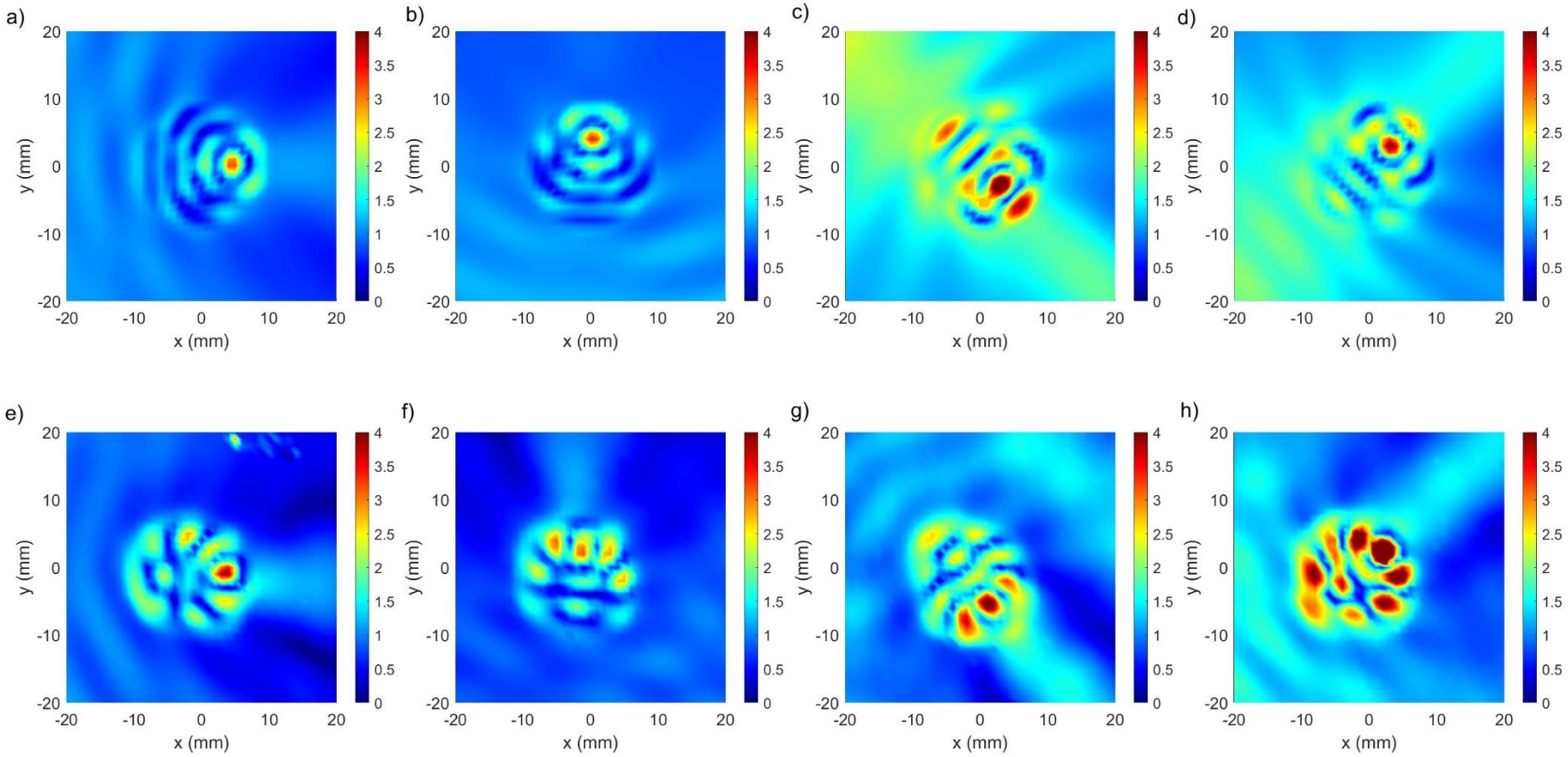

Figure 7-10 2D wavefield images (Normalized FFT magnitude, 50kHz); 40mm grid centred on delamination. Top row: FE simulation: a) 0°, b) 90°, c) -45°, d) +45° incident wave directions. Bottom row: Experiments: e) 0°, f) 90°, g) -45°, h) +45° incident wave directions

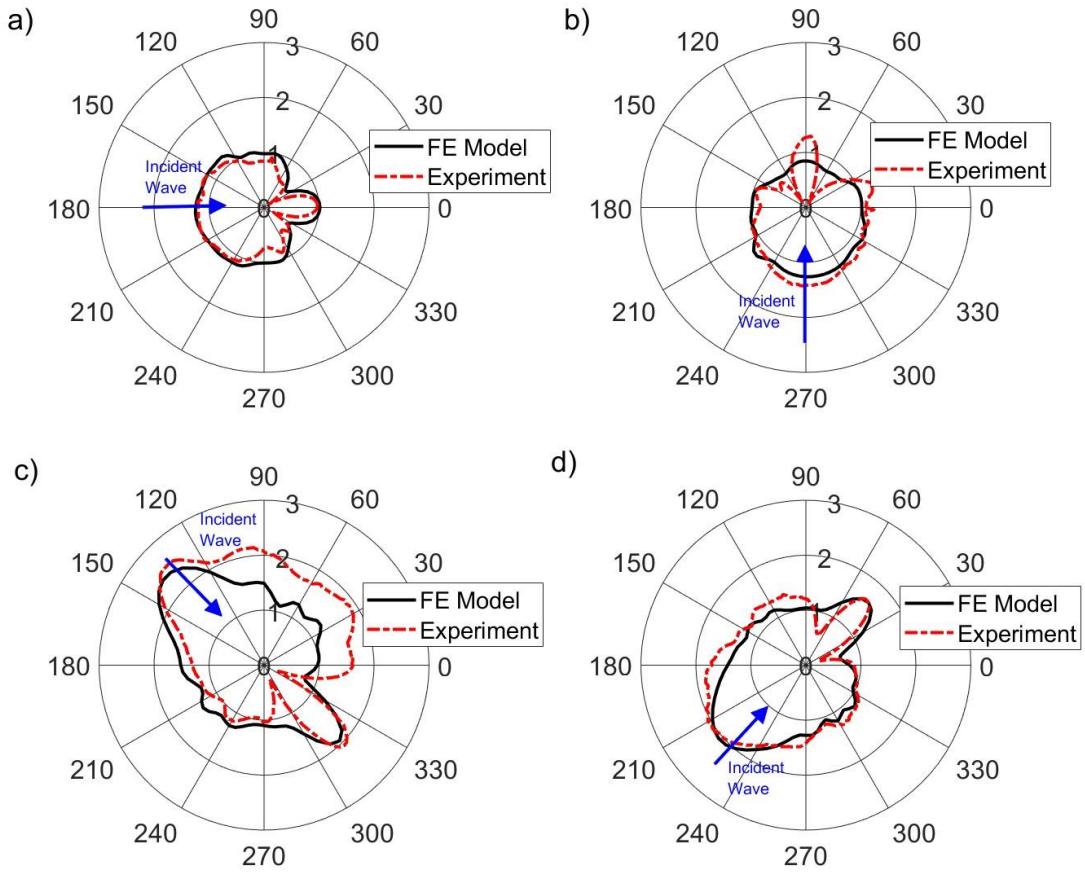

Figure 7-11 Measured and FE simulated guided wave amplitude (Normalized FFT magnitude, 50 kHz) around a circle of points (radius 30mm) centred on the delamination. Incident wave directions: a) 0°, b) 90°, c) -45°, d) +45°.

Figure 7-11 shows the amplitude comparison on a circle (radius 30mm) around the delamination for the different incident wave directions. Overall, good agreement between experiments and FE simulations can be observed. As observed in the 2D images, the directions with low amplitude next to the large forward scattered lobe are more distinct in the experimental measurements than in the FE predictions, and for the 90° incident wave the FE model underpredicts the forward scattered wave amplitude. An ideal circular delamination is modelled, whereas the shape of the delamination in the specimen is not perfectly uniform (as observed from an ultrasonic C-scan [151]), which could be the reason for this discrepancy. The scattering patterns in the 0° (Figure 7-11 a) and 90° (Figure 7-11b) directions are reasonably symmetric, consistent with the symmetry observed in the 2D scans in Figure 7-10. In the diagonal directions the simulated scattering patterns are elongated and slightly asymmetric. This asymmetry could be due to the layup of the sub-laminates in the diagonal

directions causing more focused scattering on one side of the delamination. Significant asymmetry is observed in the experimental pattern for the -45° incident wave direction (Figure 7-11 c), inconsistent with the FE results. This asymmetry is also observed as a region of higher amplitude in the top right corner of the experimental 2D scan (Figure 7-10g), which could be due to a local variation of the composite material properties in this region. Overall forward and backscattered amplitudes are higher in the diagonal directions with the highest amplitude in the -45° direction (Figure 7-11c/g), as expected from the 2D scans. This again indicates that energy focusing is occurring along the outer ply layers. Overall good agreement between experiment and FE simulation is observed.

The amplitude patterns shown in Figure 7-10 and Figure 7-11 include both the incident and scattered components of the wave. In order to isolate the scattered wave, a baseline subtraction analysis was performed on the FE results as described in section 6.3 (Figure 7-12). For each of the four incident wave directions there is a large forward scattered lobe with only very small back-scattered amplitude. For the 0° and 90° directions (Figure 7-12a/b) a small forward scattered lobe is observed, with low amplitude for the 90° direction as expected from the 2D scan (Figure 7-10b). A significant increase in forward scattered amplitude can be observed in the diagonal directions, with the highest amplitude again observed in the -45° direction. The above results (Figure 7-10 Figure 7-11 Figure 7-12) indicate that incident wave direction has a significant influence on the scattering around a circular delamination, due to the anisotropic layup of the composite laminate. It should be noted that layup alone cannot be used to predict forward scattered amplitudes, as it depends on the respective wavenumber and phase of the modes in each sub-laminate. The forward scattered wave at the delamination exit is generated by the recombination of the guided wave modes in the sub-laminates on top and bottom of the delamination [104]. For delaminations, in general scattering is dominated by a large forward scattered wave lobe with increased amplitude in addition to a significant reduction in back and sideways scattered amplitude. Previous studies [95,113,120,169], in addition to the results presented in section 7.2, indicate that a strong forward lobe, with low backscattered amplitude, occurs for delaminations at all depths. This would indicate that a

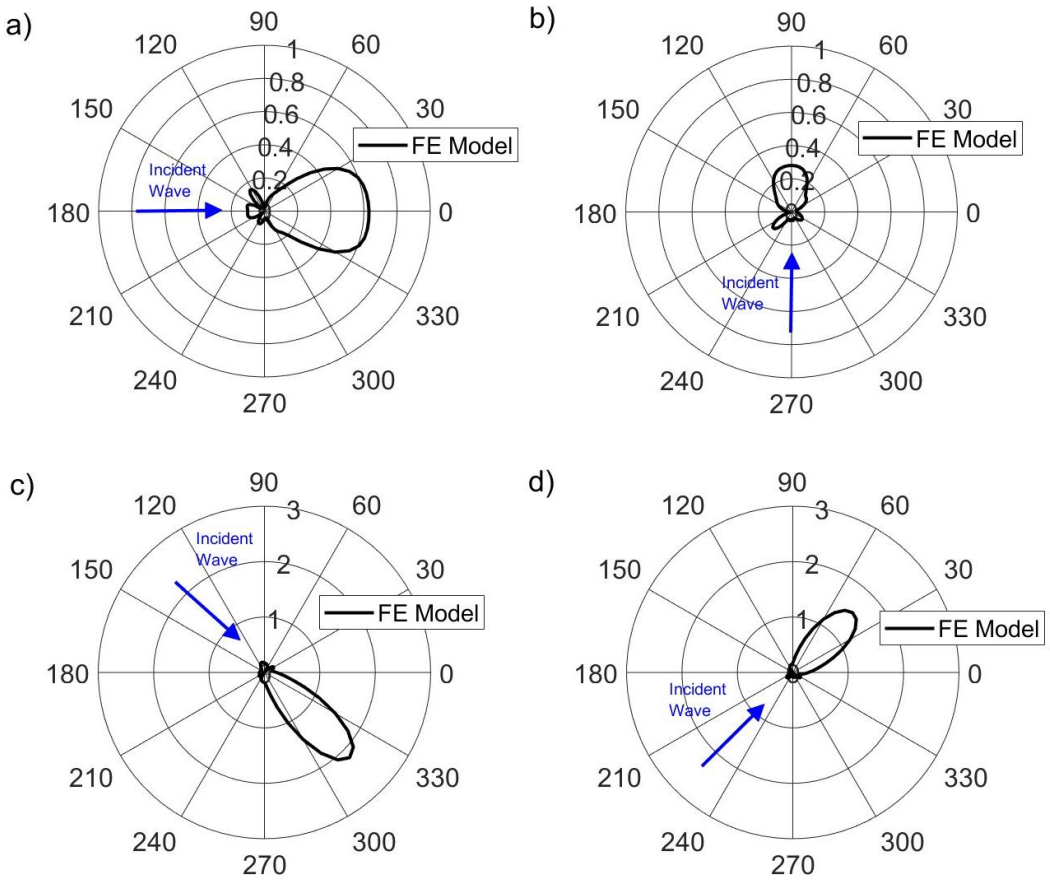

Figure 7-12 FE simulated scattered wave (Normalized FFT magnitude, complex baseline subtraction) around a circle of points (radius 30mm) centred on delamination for: a) 0°, b) 90°, c) -45°, d) +45° incident wave directions.

pulse-echo detection approach may not be suitable to detect this type of damage.

7.6 Scattering Around a Permanent Magnet Target

Experimental and numerical results for scattering at circular magnets, often used as a detection target to validate SHM approaches, were investigated. Figure 7-13 shows normalized displacement contour plots at three time snapshots for both the delamination (Figure 7-13a/b/c) and magnet FE simulations (Figure 7-13d/e/f). The contours are shown for the 0° incident wave direction. At 120ns (Figure 7-13a/d) the incident wavefront is not circular due to the anisotropy of the laminate, resulting in slightly higher wave velocities in the diagonal directions. Energy focusing of the incident wave can be observed in the diagonal directions, indicated by higher amplitude in these directions. As the wave pulse passes the delamination (Figure 7-13b/c) the forward scattered wave at the delamination exit can be seen, and almost no backscattered wave

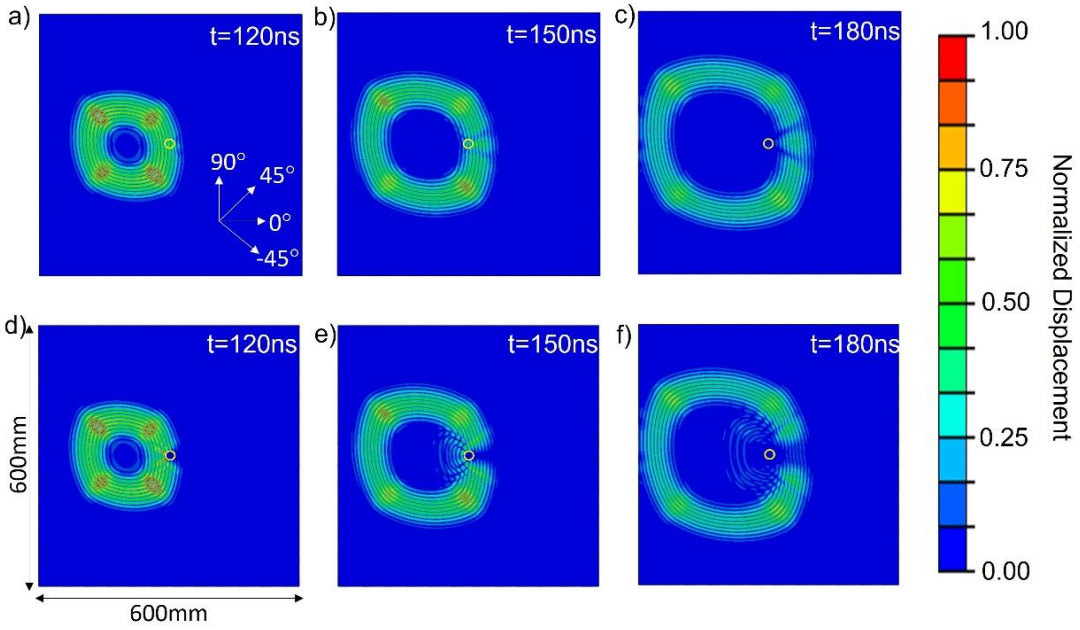

Figure 7-13 Normalized displacement magnitude contour plots for 0° incident wave direction. Obtained from FE model at time snapshots 120ns, 150ns, 180ns respectively. Top Row: Delamination located at centre of plate. Bottom row: magnet model located at centre of plate.

is observed, as expected from the FFT amplitude plots. On the other hand, the permanent magnet blocks the propagation of the guided wave, resulting in a large back-scattered amplitude. Interference between incident and sideways scattered waves can be observed in Figure 7-13e/f.

The measured and simulated FFT amplitudes around a circle of points (radius 30mm) centred on the magnet are presented in Figure 7-14 for the four incident wave directions. No forward scattered lobe is present, indicating blocking of the incident wave. A large, backscattered amplitude is observed for each incident wave direction, consistent with Figure 7-13 (0° incident wave direction). The FE scattering patterns in Figure 7-14 are symmetric with additional lobes, approximately perpendicular to the respective incident wave direction, present. Overall, this gives a distinctly different scattering pattern compared to the delamination case. The experimentally measured scattering patterns for the 0° and 90° incident wave directions are reasonably symmetric and show good agreement with the numerical results. The overall number and position of lobes are similar, although there is some variation in amplitude. The experimental measurements used honey to couple the magnet to the plate, whereas the FE model used an idealized tied contact condition, and nominal material properties, which could be causing the discrepancies. Higher scattered amplitudes can be

observed for the diagonal cases as expected, again indicating energy focusing is occurring along the outer plies. Excellent agreement between measurement and simulation was observed for the +45° direction. However, there is significant discrepancy between the -45° measurements and simulation, as also seen for the -45° delamination case (Figure 7-11c), and the -45° measured scattering pattern around the magnet is not symmetric (possibly due to manufacturing inconsistencies of the composite ply layup). There is good agreement between the FE model and experiment for the other directions and the magnet model captures the key scattering behaviour of blocking forward wave transmission. It should be noted that especially the backscattered amplitudes depend on the respective phase of the incident and scattered waves leading to destructive or constructive interference, e.g., the backscattered FE amplitude in the -45° direction (Figure 7-11c) is smaller than for +45° (Figure 7-11d), in contrast to the previous scattering results. Depending on the exact measurement location (e.g., a different radius of 25mm), a higher backscattered amplitude in the -45° direction, in comparison to the +45° direction, could be observed.

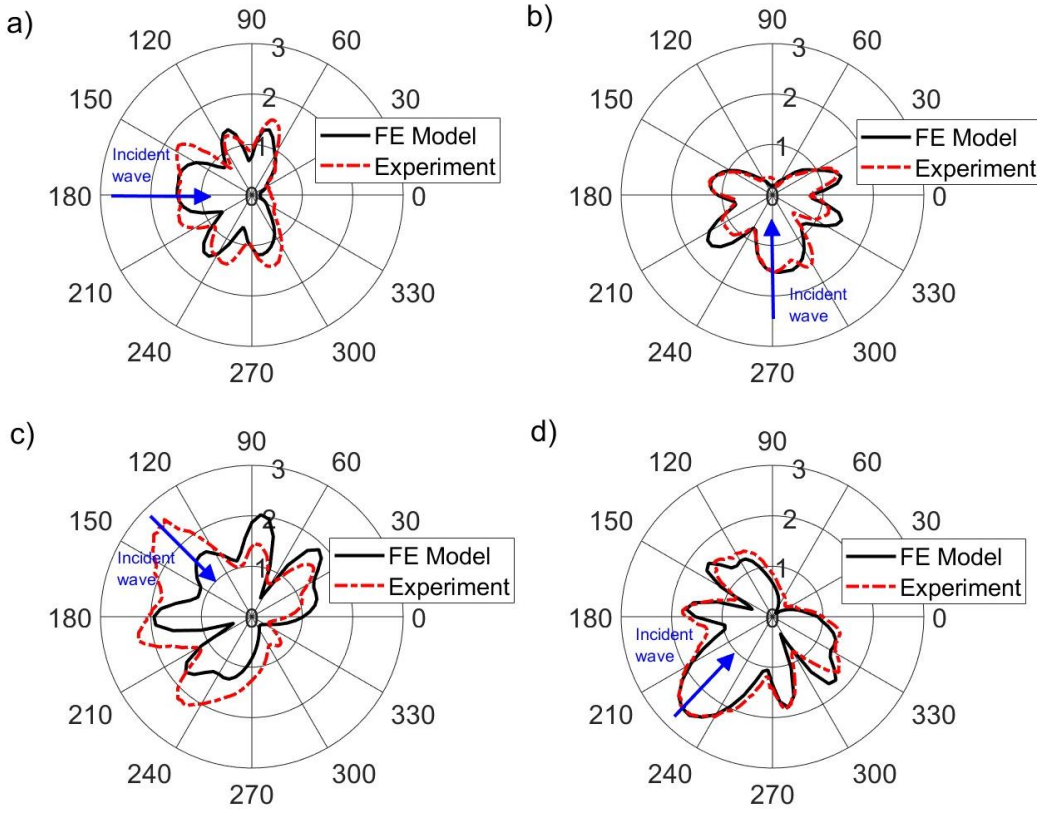

Figure 7-14 Measured and FE simulated guided wave amplitude (Normalized FFT magnitude, 50 kHz) around a circle of point (radius 30mm) centred on two magnets. Incident wave directions: a) 0°, b) 90°, c) -45°, d) +45°.

The scattered waves were isolated by performing a baseline subtraction to remove the incident wave for the experimental and simulation data (Figure 7-15). Here, the forward scattered wave represents blocking of wave transmission caused by the magnet. Backscattered amplitudes are significantly higher for all incident wave directions than observed for the delamination case, consistent with results presented in Figure 7-13 and Figure 7-14. Figure 7-15a/b shows the scattered wave for the 0° and 90° directions, respectively. Both directions show similar shaped scattering patterns with scattered amplitude in all directions and comparable, higher forward and backscattered amplitudes. There is reasonably good agreement between experiment and simulation, although the experimental baseline subtraction data is noisier than the FE model. This could be due to small errors in scanning position between baseline and magnet scans, resulting in a phase difference.

In the diagonal directions more distinct lobes are present, producing a cross-like pattern. These lobes are perpendicular to the incident wave direction (i.e., in +/45° respectively), which correspond to the orientations of the two outer plies, indicating scattering is focused along these directions. It should be emphasized that the amplitude and direction of lobes of the combined scattered wave field (Figure 7-14) can vary significantly with measurement radius due to the phase difference between incident and scattered waves leading to constructive and destructive interference. However, the baseline subtracted scattering patterns (isolated scattered wave, Figure 7-15) remain essentially the same at all radii, with a systematic drop in amplitude with radius, as the complex difference takes the respective phase of the incident and scattered waves into account [170]. Therefore, the baseline subtraction analysis is a more reliable measure of the relative scattered amplitudes in the different directions. For each incident direction the amplitude in the forward direction is approximately twice that of the backscattered direction, but mainly represents a blocking of the forward wave. Again, reasonably good agreement with experiments is observed in the forward direction. However, a lower backscattered component was measured experimentally for the diagonal incident wave cases. The side lobes are present in the experiments but not as well defined as for the simulations. Williams et al. [122] considered A_0 mode scattering around magnets for multiple incident wave directions in a 26-ply quasi-isotropic CFRP panel. Scattered amplitudes

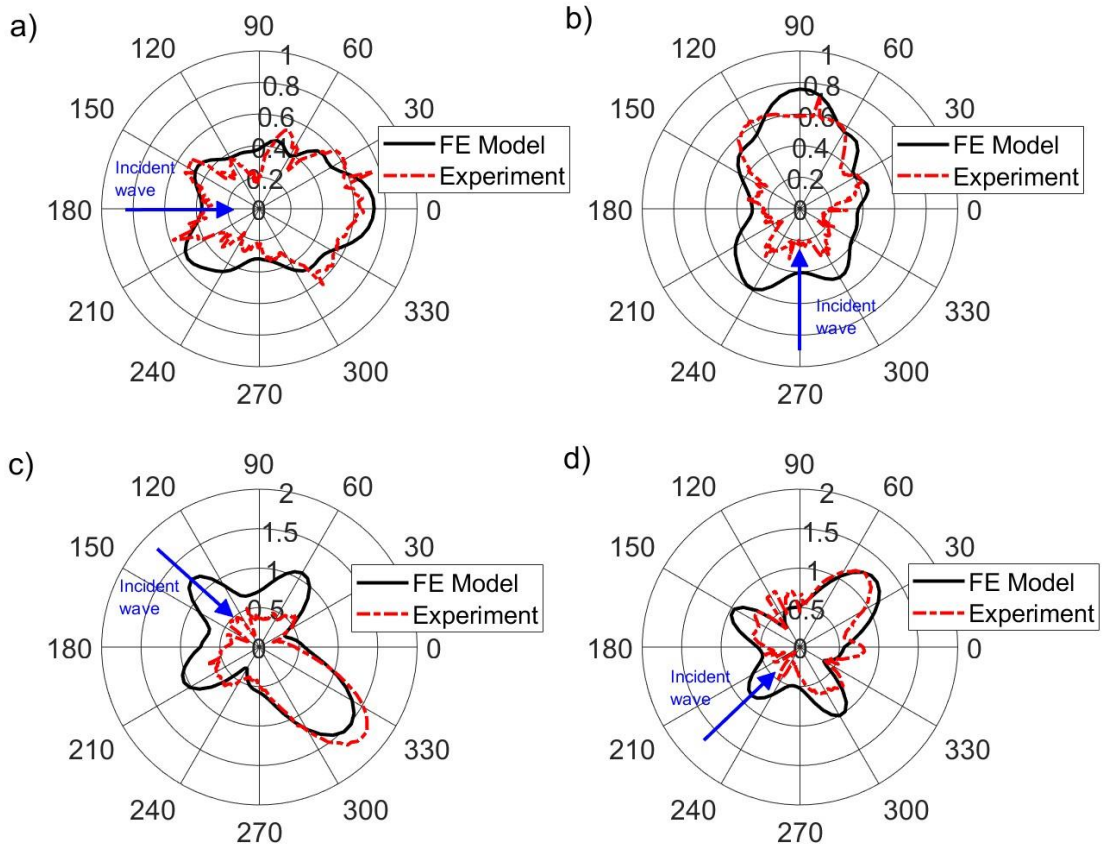

Figure 7-15 Measured and FE simulated scattered wave (Normalized FFT magnitude, complex baseline subtraction) around permanent magnets. Circle of measurement points (radius 30mm). Incident wave directions: a) 0°, b) 90°, c) -45°, d) +45°.

were found to vary with incident wave direction, however the significant change in shape between the horizontal/vertical and diagonal patterns as seen in Figure 7-15 was not observed. A greater number of ply layers with quasi-isotropic stacking sequence results in more uniform material properties, compared to the 8-ply laminate studied here, as energy focusing effects are layup dependent.

The scattering behaviour of the magnet, like the delamination, is directionally dependent due to the material anisotropy, and can be used to experimentally test the robustness of sparse array imaging algorithms for composite structures. However, the results presented in Figure 7-14 and Figure 7-15 indicate that a circular permanent magnet shows significantly different scattering behaviour compared to a delamination of similar size, with a blocking of the forward wave and higher back and sideways scattered wave amplitude, which should be considered for sparse array imaging algorithms, e.g., from additional numerical simulations.

7.7 2D Scattering Matrices

Scattering matrices allow the visualization of full scattering characteristics of a defect [171,172]. and are shown in Figure 7-16 for the 0.4mm depth delamination, 0.8mm depth delamination, and permanent magnet cases. To obtain the scattering matrices, simulations were run for incident wave directions between -90° and +90° degrees in 5° increments for each damage case. Baseline data was also obtained. The isolated scattered wave was calculated for each direction around a circle of measurement points in 5° increments, as shown for the principal directions in Figure 7-12 and Figure 7-15. As the simulated damage cases presented here are symmetric, the scattering is reversible. Scattering data for the remaining angles could be therefore obtained from existing cases rotated by 180°. The 2D scattering matrices shown in Figure 7-16 were plotted for each incident direction against respective scattered directions. Each column of the matrix corresponds to the amplitudes of a single polar plot (e.g., Figure 7-12, Figure 7-15).

The scattering matrix for the 0.4mm depth delamination case is shown in Figure 7-16a on a 20dB scale. The scattering is dominated by a strong forward scattered wave, as represented by the lobes in Figure 7-12, observed for all incident wave directions (high amplitude diagonal band). The forward scattered amplitude increases around the +/- 45° and +/- 135° incident wave directions. This indicates energy focusing is occurring in these directions, consistent with the polar plots in Figure 7-12, and further indicates energy focusing along the fibre directions of the outer ply layers. Generally, there is approximately a 10dB drop in amplitude between forward and backscattered amplitudes either side of the diagonal band. Regions of low scattered amplitude are observed in most directions, which could result in delaminations being missed from distributed sensors depending on their location. Strong forward scattering and low backscattered amplitude has been observed for delaminations at different depths [80, 98, 106], thus qualitatively the scattering matrices would be expected to resemble Figure 7-16a, although the relative amplitudes, e.g., of the diagonal band, will vary with delamination depth.

The scattering matrix for a delamination located at the midplane is shown in Figure 7-16b. As for the 0.4mm depth case (ply 2-3, Figure 7-16a) the scattering is dominated by a large forward scattered wave, generating the

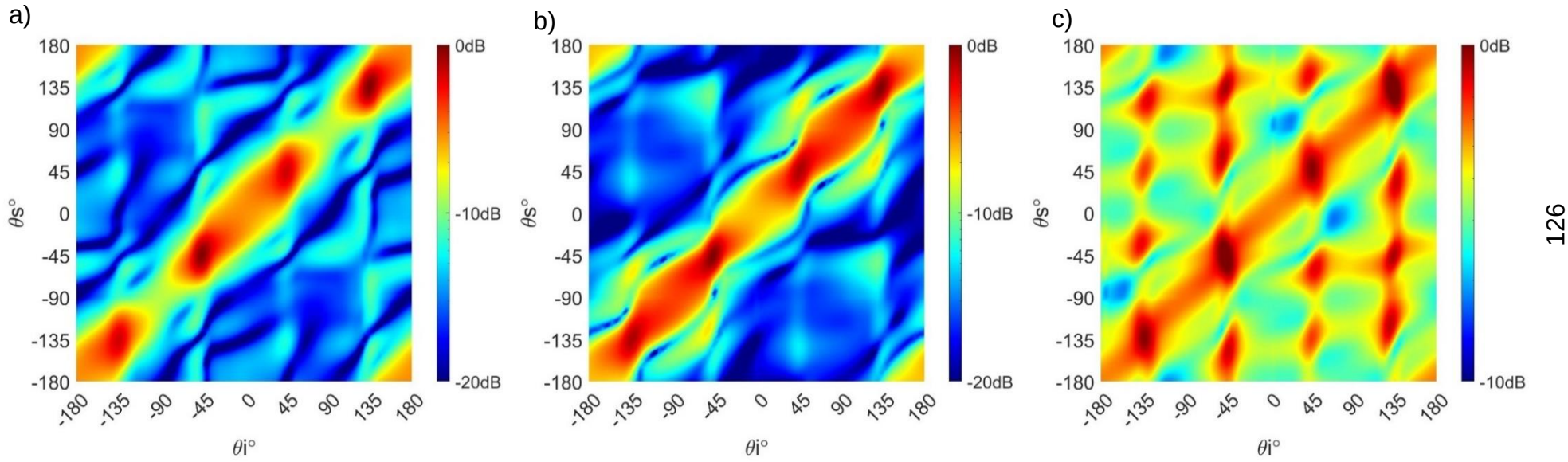

Figure 7-16 Simulated scattering matrices for: a) circular delamination 20mm radius 0.4mm depth, b) circular delamination 20mm radius 0.8mm depth (midplane), c) magnet.

diagonal band of high amplitude observed in Figure 7-16b. The structure of back and sideways scattered lobes in Figure 7-16b is somewhat different to those observed for the 0.4mm depth delamination, however an amplitude drop of approximately 10dB is again present for these lobes. The forward scattered amplitudes for the mid-plane delamination are generally higher than those of the shallower 0.4mm depth delamination. For delaminations located close to the mid-plane, less energy trapping occurs within the delamination. Strong directional dependency on the scattering is observed, with higher amplitudes in the +/- 45° and +/- 135° incident wave directions, as seen for the 0.4mm depth delamination and magnet cases. The low backscattered amplitudes (up to 20dB lower in some cases) for some combinations of incident and scattered angles further indicate that care should be taken when using SHM approaches relying on the backscattered wave, as delaminations could easily be missed.

The scattering matrix for the permanent magnet is shown in Figure 7-16c (10dB scale) which shows a significantly different scattering pattern compared to the delamination. Again, a diagonal band with higher forward scattered amplitude is observed, but here the forward scattered amplitude results in a drop in amplitude, caused by wave transmission being blocked by the magnet. Higher scattered amplitude can be observed towards the +/-45° and +/-135° directions as for the delamination. This indicates that the anisotropic layup of the plate influences scattering behaviour, regardless of defect type. However, the increase in amplitude is not as significant for the magnet as it is for the delamination, scattered amplitudes are overall more uniform, with scattering occurring in all directions. Additional directions of higher scattered wave amplitude can be observed for incident wave directions +/-45° and +/-135°. This is due to the cross shaped scattering patterns (e.g., Figure 7-15c) that occur in these directions, likely caused by scattered waves being focused along the outer ply layers oriented in these directions. For some directions low amplitude is observed, however this effect is much less pronounced than for the delamination. Overall, for the magnets, the ratio of forward to backscattered amplitudes is lower than for the delamination. This is due to scattered amplitude observed in multiple directions in the magnet cases, whereas the delamination cases were dominated by a distinct forward scattered lobe.

7.8 Implications for Structural Health Monitoring and NDE

7.8.1 NDE vs SHM

The wave trapping phenomena observed in Chapters 6 and 7 could be exploited for localised NDE inspection of aircraft structures. The region of increased amplitude observed in the delamination region can not only be used to locate damage, but to characterise the size and shape of a delamination. However, significant wave trapping is only observed for shallow delaminations, proving problematic for deeper damage. One possible way to overcome this would be to inspect both sides of the structure, however this may not be practical for components with limited access. Whilst damage detection using wave trapping has its limitations, the scattered waves propagating away from the delamination can be detected at all delamination depths. Somewhat counterintuitively, delaminations produce a strong forward scattered wave amplitude but experience limited backscattering. Transducer placement should therefore be carefully considered for NDE of delamination damage. For example a pulse echo setup may not detect scattering, whereas a pitch catch arrangement would. The amplitude of forward scattered waves is dependent of the phase difference between propagating waves in the upper and lower sublaminates, which in turn related to the ratio of the wavelength of the delamination. In principle this could be used to characterise delamination length. However, as seen in section 7.2, additional factors, such as the thickness and ply layup of sub laminates also affect the forward scattered amplitude, adding further complexity to the problem. It was also demonstrated in sections 6.6 and 7.1 that the forward scattered amplitudes have limited sensitivity to small changes in delamination size reducing the accuracy of characterisation. However, previous studies have demonstrated that larger variations in delamination size can be detected from the forward scattered amplitudes.

As discussed above, using guided waves for NDE composite components has some limitations in terms of damage characterisation in comparison to conventional ultrasonic techniques. However, the long-range propagation of guided waves makes this technique suitable for SHM of aircraft structures. The scattered amplitudes, propagating away from the delamination can be used to

triangulate damage using a distributed sensor array which is discussed further in section 7.8.3. Such a detection method would be able to locate damage, but not fully characterise it and so follow up inspection with a localised method would be required to determine the extent of damage. As seen in the results in section 7.2 the scattered wave is present for delaminations at all depths and so this approach is suitable for detecting deep damage where wave trapping cannot be observed or for inspecting and monitoring inaccessible regions of the structure.

7.8.2 Modelling Realistic Damage

This investigation has focused on guided wave interaction with simple circular and ellipse shaped delaminations. Whilst these damage shapes can occur as part of multilayer damage, wave scattering around real BVID will likely differ from that of the idealised shapes presented here. The procedure for incorporating damage into the FE model presented in this work could potentially be extended to incorporate more complex damage if separate damage data is available, for example X-ray CT data [10]. Some studies have focused on detection and sizing of the major (largest) delamination at real BVID [80] and wave trapping has been demonstrated to be sensitive to multi-layered delaminations [38]. This indicates that the methodology presented in this work could be applied to more realistic damage types.

7.8.3 Sparse Array Imaging

The anisotropy results indicate that guided wave scattering around a delamination in composite structures can be strongly influenced by incident wave direction due to the anisotropy of the laminate. Therefore, imaging algorithms should take the anisotropic effects into account. Large variation of incident and scattered amplitudes with propagation direction were observed due to energy being focused along fibre directions of the outer ply layers. However, as the group velocity of the A_0 mode is less directionally dependent than, for example, the S_0 mode, accounting for the variation in group velocity for an anisotropic laminate may not be as critical as considering the significant changes in amplitude due to energy focusing.

Algorithms such as MVDR may be better suited for damage localization in anisotropic structures as the signals are adaptively weighted based on prior knowledge of expected damage scattering patterns. The amplitudes obtained from the scattering matrices in (Figure 7-16) could be used to adaptively weight signals in different wave propagation directions. For delaminations a significant variation in the amplitude of the forward scattered lobe was found, with very limited scattered wave amplitude observed in other directions. Slightly counterintuitively, increased rather than decreased amplitude in the forward direction was observed for the artificial delamination damage. Scattering patterns around magnets were also demonstrated to vary with incident wave propagation direction, although scattered amplitudes were more uniform for different incident wave directions. As scattering occurs in all directions for the magnet, this could indicate that magnets simulating damage are easier to detect with sparse array imaging and that realistic damage types might be missed if imaging algorithms are only tested on magnet targets. This is particularly the case if the selected SHM method relies on the backscattered wave (e.g., phased array imaging). Additionally, delamination damage with limited scattering except in the forward direction, located outside of the area covered by a distributed sensor array could be missed unless edge reflections are considered. Whilst magnets are an effective tool for the experimental development and testing of SHM imaging algorithms due to their low cost and ability to be easily re-positioned without damaging the structure, they cannot accurately represent scattering at a delamination. The robustness of imaging algorithms scattering patterns at realistic damage should also be ascertained.

7.9 Conclusions

In this chapter the influence of delamination shape and depth on scattering of the A_0 mode were investigated numerically. Small changes in delamination shape were found to have a significant effect on the interference pattern on top of the delamination, but limited effect on the scattered wave directivity some distance from the defect. The region of high amplitude on top of the delamination could be used to estimate delamination size and shape. Delamination depth significantly influenced both the interference pattern on top of the delamination, and the scattering pattern outside of the delamination, due

to the different ply layups of the sub-laminate. Generally, both wave trapping and forward scattered components were observed for delaminations located between the outer plies of the laminate. The largest forward scattered amplitude occurred at the mid-plane delamination, likely due to the symmetrical layup of the sub-laminates. For further analysis the incident wave was removed, and the scattered wave was isolated by performing a complex difference baseline subtraction to obtain the angular energy distribution. At all delamination depths negligible backscattered amplitude was observed, indicating that delaminations may be difficult to detect using a pulse-echo SHM approach. The strong forward scattered amplitude indicates that a pitch-catch approach could be more appropriate, although care must be taken as the forward scattered component is not always directed along the incident wave propagation direction. The delamination shapes investigated in this study are idealised compared to real BVID, however, as discussed in section 7.8.2, the methodology presented could be extended to incorporate more complex damage types.

The influence of anisotropy and incident wave directionality on guided wave propagation and scattering in a quasi-isotropic CFRP laminate was investigated through experiments and FE simulation. Guided waves propagating in the undamaged laminate were found to have increased amplitude in directions corresponding to the fibre orientations of the outer ply layers, due to energy focusing. Scattering around a circular delamination and magnet target was studied for multiple incident wave directions. Isolating the scattered wave from a complex difference baseline subtraction analysis provides a good measure of the respective scattering patterns. Distinct scattering patterns were observed for the delamination and magnet cases, with significant directional dependency for both damage types. For the delamination, a strong forward scattered lobe with small, backscattered amplitude was observed for each incident direction. The magnet was observed to block transmission of forward scattered waves and higher backscattered amplitude was present. As scattering around a magnet is directionally dependent, magnets can be a practical experimental tool for developing distributed guided wave sensor monitoring of anisotropic structures. However, as scattering at a magnet is significantly different to that of a delamination the different scattering patterns for realistic damage should be considered when developing SHM systems to ensure that damage is not

misinterpreted due to, e.g., low backscattered amplitudes. It should be ensured and tested, e.g., from FE simulations, that the employed imaging algorithms are reliable by considering the variations in guided wave scattering for different damage types. Pulse-echo detection approaches and distributed sensors could have limited sensitivity for delamination detection outside the area covered by the guided wave sensors due to the low backscattered amplitude. Overall, the results demonstrate that guided wave scattering at different damage types is influenced by the incident wave direction, and material anisotropy should be considered when designing SHM imaging methods for composite laminates.

8 Conclusions and Future Work

Composites are ever more widely used for the manufacture of lightweight aircraft parts. However, composite laminates are prone to delamination damage which can cause significant strength reduction of components. Guided waves are a promising SHM techniques, but the high material anisotropy of composites influences wave propagation, potentially reducing the accuracy of damage detection. During this PhD research project guided wave propagation in composite laminates with and without delaminations have been studied experimentally through laser Doppler vibrometer measurements and FE modelling.

8.1 Summary of Findings

Low frequency ultrasonic guided waves are ideal for in-situ SHM of composites as they are able to propagate long distances with low attenuation, allowing for rapid long-range inspection of large structures. Fibre reinforced composite laminates have strong material anisotropy due to the high stiffness fibres, which can lead to severe anisotropic wave propagation effects. Directional dependency of phase and group velocity, wave skewing and beam spreading can all occur, which can significantly reduce the accuracy of damage detection if not considered. Whilst the theoretical principles of these effects are well known and established, experimental demonstration of these effects is limited. Composite laminates are vulnerable to BVID from low velocity impacts. Damage is multi modal with delamination causing the most significant strength reduction. The interaction of guided waves with delamination damage is influenced by delamination shape size and depth, however the guided wave interaction with delaminations is not yet fully understood. Additionally, the effects of material anisotropy on scattered waves have not yet been ascertained. The present study aims to improve the understanding of the effects of anisotropy on guided wave propagation and scattering at damage in composite laminates. The main findings of this work are discussed below.

Anisotropic guided wave propagation effects of the A_0 mode were investigated for an undamaged unidirectional CFRP laminate. The directional dependency of guided wave phase and group velocities was studied for both point and line

sources through finite element models and validated by experimental measurements from a point transducer. Previous studies have only considered the group velocity variation, with limited comparison to theoretical predictions. In this work, simulated and measured values were compared with theoretical values obtained from dispersion curves. Care should be taken when measuring velocities in an anisotropic material, particularly if using a point source such as a piezoelectric disc, often selected for guided wave measurements, as velocities can be significantly underpredicted in wave launching directions with high skew angles. It has been demonstrated that measured velocities can accurately match theoretical predictions either by using a line source of sufficient length to match the planar wavefront assumed in theory, allowing for measurement on the full energy of the pulse despite wave skewing effects or, alternatively, by using a point/short line source but correcting for skew angle when calculating velocities. The form of the correction required depends on the geometry of the excitation source. The skew angle correction in CFRP has been previously reported for group velocity measurement from a point source excitation, however illustration of the correction for both group and phase velocity, and for a line excitation has not been considered before.

Numerical and experimental studies of wave skewing behaviour of a line source on various incident wave directions were performed in order to provide a full comparison to theoretical values calculated from phase slowness curves. Whilst the principle of the wave skew angle is well known, previous studies of guided wave propagation in CFRP have only measured a steering in a single wave propagation direction. In this work, zero skew angle was observed in principal directions (0°, 90° relative to fibre orientation) directions, with maximum skew angle of 25° occurring at 45° for the experimental, FE, and theoretical values. Overall, good agreement was found between experiment, simulation, and theory. Beam spreading due to material anisotropy was estimated from the experimental and FE results. Limited spreading occurred in the 0° and 15° directions due to the high energy focusing towards the fibres. Beam spreading increased as the wave launching direction moved away from the fibre directions with the greatest spreading occurring at 75° from the fibre orientation. Whilst beam spreading has been treated theoretically, it has not been studied experimentally in CFRP. The measured beam spread angles were compared

with the anisotropy factor, which is calculated from the phase slowness curve. While a direct comparison could not be drawn between the anisotropy factor and beam spreading angle, the physical behaviour observed in the experiments and simulations matched that of the theory. Quantitative experimental measurement of beam spreading in CFRP, and comparison of the spreading to theoretical predictions has not been previously studied.

Guided wave scattering around circular and ellipse shaped delaminations in a quasi-isotropic laminate has been investigated experimentally and through FE simulations. The artificial delamination in the physical specimen was located asymmetrically through the full thickness of the plate, a damage case for which guided wave scattering has not previously been considered experimentally. Wavefield measurements on top of the delamination showed increased amplitude in the delamination, indicating that wave trapping was occurring. A forward scattered wave and shadow regions were observed behind the defect. A full 3D layered model containing a zero-volume delamination was developed and showed good agreement for scattered waves propagating away from the damage in the undamaged part of the plate. Wave trapping phenomena were observed in the FE results. The influence of delamination shape and depth were investigated numerically. The interference pattern on top of the delamination was found to be very sensitive to changes in delamination shape. As such, a high amplitude region on top of the delamination could be used to estimate delamination size and shape. However, the scattered wave propagating away from the delamination was found to have limited sensitivity to small changes (2-4mm) in delamination shape. This is because the forward scattered wave depends on the phase difference of waves propagating in each sublaminate, which in turn is related to the ratio of wavelength to delamination length. Generally, both wave trapping and forward scattered components were observed for shallower delaminations. The largest forward scattered amplitude occurred at the mid-plane delamination, likely due to the symmetrical layup of the sub-laminates. Wave trapping was not observed for deep delaminations, however forward scattering was still detected. Scattering patterns were identical for delaminations located at symmetric depths.

The effect of anisotropy on scattered guided waves has not previously been considered. The influence of material anisotropy on guided wave scattering at a

delamination was investigated by varying the incident wave launching direction. Higher incident wave amplitudes were observed in directions corresponding to the fibre orientations of the outer ply layers, due to energy focusing. Permanent magnets provide a cheap and practical method for simulating damage experimentally, as they can easily be repositioned on a structure. However, the extent to which magnets can be used to simulate delaminations has not yet been ascertained, experimentally or numerically. The isolated scattered wave around both delamination and magnet targets were obtained using a complex difference baseline subtraction. Distinct, scattering behaviour was observed for each damage case, with significant directional dependency for each type. For the delamination a strong forward scattered lobe with small, backscattered amplitude was observed for each incident direction and delamination depth. In contrast, the magnet blocked forward transmission of the wave and high back and side scattered amplitudes were present. 2D scattering matrices, which represent the full scattering characteristics of a particular damage type, were calculated for two delamination depths and the magnet target. These further demonstrated the distinct scattering behaviour for each damage type. The different scattering patterns for different damage types should be considered when developing SHM systems to ensure that damage is not misinterpreted due to, e.g., low backscattered amplitudes. It should be ensured and tested, e.g., from FE simulations, that the employed imaging algorithms are reliable by considering the variations in guided wave scattering for different damage types. Pulse-echo detection approaches and distributed sensors could have limited sensitivity for delamination detection outside the area covered by the guided wave sensors due to the low backscattered amplitude.

The work presented in this thesis has demonstrated that anisotropic guided wave propagation effects such as severe skew angles and beam spreading could lead to reduced accuracy in damage location or regions where little to no guided wave amplitude can propagate in composite panels. The highly focused scattering at a delamination and significant variation in scattered amplitudes due to material anisotropy could also lead to delaminations being missed. Therefore, anisotropic wave propagation effects should be considered when designing SHM systems for composite components.

8.2 Recommendation for Future Work

Anisotropic wave propagation in other composite layups

The unidirectional laminate considered in Chapter 5 displays the most severe anisotropic wave propagation behaviour, however, it would be of interest to investigate wave skewing and beam spreading in other composite layups (e.g., a cross-ply laminate) in order to determine the extent to which anisotropy influences the A_0 mode in other structures. As seen in Chapter 7, anisotropic effects such as amplitude variation can still be significant even for a quasi-isotropic layup, so further research into anisotropic wave propagation in other layups is required.

Guided wave scattering at realistic damage types

The scattering investigation in Chapters 6 and 7 considers a single delamination damage. It would therefore be interesting to consider A_0 mode sensitivity to other damage types. Scattering at multiple damages, and several delaminations stacked in the same region, as is the case for impact damage, should be studied. Whilst delamination damage is a critical failure mode in composites, they rarely occur in isolation. Guided wave interaction with impact damage therefore needs to be understood. The influence of impact energy on guided wave scattering directivity could be investigated by measuring guided wave interaction on top of and around the impacted area of a composite panel.

Complex composite geometries

This thesis has considered guided wave propagation in flat composite plates with artificial damage in a laboratory environment. It is therefore desirable to extend this work to improve the monitoring of more realistic structures such as components with more complicated geometries (e.g., T-joints and stiffeners). More fundamental studies such as the effect of panel curvature on guided wave propagation could be performed, leading to investigating wave propagation and scattering at damage in actual aircraft components. The additional complexity due to the geometry of the structure, in addition to the complexity of the material and damage mechanism, is likely to have significant effects on wave propagation. This will be essential to determine the extent to which guided wave SHM can be used to monitor aircraft.

Sparse array imaging for SHM of anisotropic composites

Guided wave based sparse array imaging, as part of a smart, instrumented structure, generates and detects guided waves using a network of permanently attached sensors. Subsurface damage can be triangulated and localized, generating a damage map of the structure. Several algorithms have been developed to reconstruct the guided wave signals and localize damage; however, these have mostly been demonstrated for simple metallic (isotropic) plate-like structures. Attempts to incorporate anisotropic effects have been limited to account for small variations in guided wave velocity. No efficient sparse array imaging techniques have been developed to incorporate the large variations in guided wave propagation in anisotropic composite structures. The 2D scattering matrices presented in Chapter 7 could be incorporated into sparse array imaging algorithms such as MVDR, which require prior knowledge of damage characteristics, to account for severe anisotropy. The MVDR algorithm adaptively weights signals prior knowledge of scattering, and so the scattering matrices in Chapter 7 could be used for such a weighting.

References

[1] W.J. Cantwell, J. Morton, Geometrical Effects in the Low Velocity Impact Response of CFRP, Compos Struct. 12 (1989) 39–59.

[2] B. Park, Y.K. An, H. Sohn, Visualization of hidden delamination and debonding in composites through noncontact laser ultrasonic scanning, Compos Sci Technol. 100 (2014) 10–18.

[3] I.G. Scott, C.M. Scala, A review of non-destructive testing of composite materials, NDT International. 15 (1982) 75–86.

[4] S. Thomas, K. Joseph, K. Malhotra, K. Goda, M.S. Sreekala, Polymer Composites: Volume 1, Wiley, 2012.

[5] W.J. Cantwell, J. Morton, The impact resistance of composite materials - a review, Composites. 22 (1991) 347–362.

[6] H. Yun Choi, F. Chang, A Model for Predicting Damage in Graphite/Epoxy Laminated Composites Resulting from Low-Velocity Point Impact, J Compos Mater. 26 (1992) 2134–2169.

[7] H.M. Hsiao, I.M. Daniel, Effect of fiber waviness on stiffness and strength reduction of unidirectional composites under compressive loading, Compos Sci Technol. 56 (1996) 581–593.

[8] H. Adams, M.W. Hyer, Effects of Layer Waviness on the Compression Strength of Thermoplastic Composite Laminates, J. Reinf. Plast. 12 (1993) 414–429.

[9] D.J. Bull, S.M. Spearing, I. Sinclair, L. Helfen, Three-dimensional assessment of low velocity impact damage in particle toughened composite laminates using micro-focus X-ray computed tomography and synchrotron radiation laminography, Compos Part A Appl Sci Manuf. 52 (2013) 62–69.

[10] T.W. Shyr, Y.H. Pan, Impact resistance and damage characteristics of composite laminates, Compos Struct. 62 (2003) 193–203.

[11] K. Hayat, S.K. Ha, Low-velocity impact-induced delamination detection by use of the S0 guided wave mode in cross-ply composite plates: A numerical study, J. Mech Sci and Tech. 28 (2014) 445–455.

[12] W.J. Cantwell, J. Morton, Detection of impact damage in CFRP laminates, Compos Struct. 3 (1985) 241–257.

[13] S. Abrate, Impact on Composite Structures, Cambridge University Press, Cambridge, 1998.

[14] C.A.C. Leckey, M.D. Rogge, F.R. Parker, Guided waves in anisotropic and quasi-isotropic aerospace composites: Three-dimensional simulation and experiment, Ultrasonics. 54 (2014) 385–394.

[15] J. Wertz, S. Wallentine, J. Welter, J. Dierken, J. Aldrin, Volumetric characterization of delamination fields via angle longitudinal wave ultrasound, AIP Conf Proc, 1806(2017) 090006.

[16] O. Mesnil, C.A.C. Leckey, M. Ruzzene, Instantaneous and local wavenumber estimations for damage quantification in composites, Struct Health Monit. 14 (2015) 193–204.

[17] M.R. Wisnom, The role of delamination in failure of fibre-reinforced composites, Philos Trans Royal Soc A. 370 (2012) 1850–1870.

[18] J.C. Prichard, P.J. Hogg, The role of impact damage in post-impact compression testing, Composites. 21 (1990) 503–511.

[19] Z. Su, L. Ye, Y. Lu, Guided Lamb waves for identification of damage in composite structures: A review, J Sound Vib. 295 (2006) 753–780.

[20] R.D. Adams, P. Cawley, A review of defect types and nondestructive testing techniques for composites and bonded joints, NDT International 21(4) (1988) 208-222.

[21] R.H. Bossi, V. Giurgiutiu, Nondestructive testing of damage in aerospace composites, Polymer Composites in the Aerospace Industry, Elsevier Inc., (2015) 413–448.

[22] L. Toubal, M. Karama, B. Lorrain, Damage evolution and infrared thermography in woven composite laminates under fatigue loading, Int J Fatigue. 28 (2006) 1867–1872.

[23] N. Akhter, H.C. Jung, H.S. Chang, K.S. Kim, Location of delamination in laminated composite plates by pulsed laser holography, Opt Lasers Eng. 47 (2009) 584–588.

[24] P.F. Liu, J.K. Chu, Y.L. Liu, J.Y. Zheng, A study on the failure mechanisms of carbon fiber/epoxy composite laminates using acoustic emission, Mater Des. 37 (2012) 228–235.

[25] J. Cheng, J. Qiu, X. Xu, H. Ji, T. Takagi, T. Uchimoto, Research advances in eddy current testing for maintenance of carbon fiber reinforced plastic composites, Int J Appl Electromagn. 51 (2016) 261–284.

[26] T.J. Swait, F.R. Jones, S.A. Hayes, A practical structural health monitoring system for carbon fibre reinforced composite based on electrical resistance, Compos Sci Technol. 72 (2012) 1515–1523.

[27] M. Zhong, B. Liu, C. Li, Z. Wang, D. Wei, B. Zhou, X. Dai, Y. Xu, Terahertz Spectroscopy and Imaging Detection of Defects in Civil Aircraft Composites, J Spectrosc. 2020 (2020).

[28] M.E. Ibrahim, Nondestructive evaluation of thick-section composites and sandwich structures: A review, Compos Part A Appl Sci Manuf. 64 (2014) 36–48.

[29] D. Shoukroun, L. Massimi, F. Iacoviello, M. Endrizzi, D. Bate, A. Olivo, P. Fromme, Enhanced composite plate impact damage detection and characterisation using X-Ray refraction and scattering contrast combined with ultrasonic imaging, Compos B Eng. 181 (2020) 107579.

[30] M. Endrizzi, B.I.S. Murat, P. Fromme, A. Olivo, Edge-illumination X-ray dark-field imaging for visualising defects in composite structures, Compos Struct. 134 (2015) 895–899.

[31] J.A. Ogilvy, Theoretical comparison of ultrasonic signal amplitudes from smooth and rough defects, NDT International. 19 (1986) 371–385.

[32] W.H.M. van Dreumel, Ultrasonic scanning for quality control of advanced fibre composites, NDT International. 11 (1978) 233–235.

[33] F. Aymerich, S. Meili, Ultrasonic evaluation of matrix damage in impacted composite laminates, Compos B Eng. 31 (2000) 1–6.

[34] V.K. Kinra, A.S. Ganpatye, K. Maslov, Ultrasonic Ply-by-Ply Detection of Matrix Cracks in Laminated Composites, J Nondestr Eval. 25 (2006) 37–49.

[35] M. Castaings, P. Cawley, R. Farlow, G. Hayward3, Single Sided Inspection of Composite Materials Using Air Coupled Ultrasound, J Nondestr Eval. 17(1) (1998) 37-45.

[36] A. Mahoon, The role of non-destructive testing in the airworthiness certification of civil aircraft composite structures, Composites. 19 (1988) 229–235.

[37] B. Drinkwater, P. Cawley, An ultrasonic wheel probe alternative to liquid coupling, AIP Conf Proc. 14 (1995) 983–989.

[38] J.L. Rose, Ultrasonic guided waves in solid media, Cambridge University Press, 2014.

[39] Z. Liu, C. He, B. Wu, X. Wang, S. Yang, Circumferential and longitudinal defect detection using T(0, 1) mode excited by thickness shear mode piezoelectric elements, Ultrasonics. 44 (2006) 1135–1138.

[40] P. Cawley, Structural health monitoring: Closing the gap between research and industrial deployment, Struct Health Monit. 17 (2018) 1225–1244.

[41] Y. Cho, Estimation of ultrasonic guided wave mode conversion in a plate with thickness variation, IEEE Trans Ultrason Ferroelectr Freq Control. 47 (2000) 591–603.

[42] D. Alleyne, P. Cawley, The Interaction of Lamb Waves with Defects, IEEE Trans Ultrason Ferroelectr Freq Control. 39 (1992) 381–397.

[43] H. Lamb, On waves in an elastic plate, Proc R Soc A. 93 (1917) 114–128.

[44] B. Pavlakovic, M. Lowe, D. Alleyne, P. Cawley, Disperse: A General Purpose Program for Creating Dispersion Curves, AIP Conf Proc 16 (1997) 185–187.

[45] H. Mei, M.F. Haider, R. James, V. Giurgiutiu, Pure S0 and SH0 detections of various damage types in aerospace composites, Compos B Eng. 189 (2020) 107906.

[46] A. Bernard, M.J.S. Lowe, M. Deschamps, Guided waves energy velocity in absorbing and non-absorbing plates, J Acoust Soc Am. 110 (2001) 186–196.

[47] G. Neau, M. Deschamps, M.J.S. Lowe, Group velocity of Lamb waves in anisotropic plates: Comparison between theory and experiments, AIP Conf Proc. 557 (2001) 81–88.

[48] M.J.S. Lowe, G. Neau, M. Deschamps, Properties of Guided Waves in Composite Plates, and Implications for NDE, AIP Conf Proc. 700 (2004) 214–221.

[49] W.H. Prosser, M.D. Seale, B.T. Smith, Time-frequency analysis of the dispersion of Lamb modes, J Acoust Soc Am. 105 (1999) 2669–2676.

[50] P. Wilcox, M. Lowe, P. Cawley, Effect of dispersion on long-range inspection using ultrasonic guided waves, NDT and E International. 34 (2001) 1–9.

[51] B. Pavlakovic, M. Lowe, Disperse User’s Manual, 2003.

[52] B.H. Crespo, C.R.P. Courtney, B. Engineer, Calculation of guidedwave dispersion characteristics using a three-transducer measurement system, Appl Sci. 8 (2018) 1253–1268.

[53] N. Guo, P. Cawley, The interaction of Lamb waves with delaminations in composite laminates, J Acoust Soc Am. 94 (1993) 2240–2246.

[54] H. Gao, Ultrasonic guided wave mechanics for composite material structural health monitoring, PhD Thesis, The Pennsylvania State University, 2007.

[55] O. Putkis, R.P. Dalton, A.J. Croxford, The anisotropic propagation of ultrasonic guided waves in composite materials and implications for practical applications, Ultrasonics. 65 (2016) 390–399.

[56] V. Memmolo, E. Monaco, N.D. Boffa, L. Maio, F. Ricci, Guided wave propagation and scattering for structural health monitoring of stiffened composites, Compos Struct. 184 (2018) 568–580.

[57] F. Hervin, P. Fromme, Anisotropy influence on guided wave scattering for composite structure monitoring, Struct Heal Monit . (2022).

[58] P. Fromme, M. Pizzolato, J. Robyr, B. Masserey, Lamb wave propagation in monocrystalline silicon wafers, J Acoust Soc Am. 143 (2018) 287–295.

[59] W.H. Prosser, R.D. Kriz, D.W. Fitting, Effect of stress on energy flux deviation of ultrasonic waves in GR/EP composites, Proc IEEE Ultrasonics Symposium, 1990: pp. 961–964.

[60] S.H. Rhee, J.K. Lee, J.J. Lee, The group velocity variation of Lamb wave in fiber reinforced composite plate, Ultrasonics. 47 (2007) 55–63.

[61] G. Neau, M.J.S. Lowe, M. Deschamps, Propagation of Lamb waves in anisotropic and absorbing plates: Theoretical derivation and experiments, AIP Conf Proc. 615 (2002) 1062–1069.

[62] E. Glushkov, N. Glushkova, A. Eremin, R. Lammering, Group velocity of cylindrical guided waves in anisotropic laminate composites, J Acoust Soc Am. 135 (2014) 148–154.

[63] L. Yu, Z. Tian, Guided wave phased array beamforming and imaging in composite plates, Ultrasonics. 68 (2016) 43–53.

[64] F. Yan, J.L. Rose, Guided wave phased array beam steering in composite plates, Proceedings of SPIE. 6532 (2007) 65320G.

[65] F. Yan, J.L. Rose, Time delay comb transducers for aircraft inspection, The Aeronaut J. 113 (2009) 417–427.

[66] F. Yan, J.L. Rose, Composite plate inspection using a novel guided wave skew effect method, AIP Conf Proc, 28 (2009) 1049–1056.

[67] J.A. Ogilvy, Ultrasonic beam profiles and beam propagation in an austenitic weld using a theoretical ray tracing model, Ultrasonics. 24 (1986) 337–347.

[68] B.P. Newberry, R.B. Thompson, A paraxial theory for the propagation of ultrasonic beams in anisotropic solids, J Acoust Soc Am. 85 (1989) 2290–2300.

[69] A. Karmazin, E. Kirillova, W. Seemann, P. Syromyatnikov, A study of time harmonic guided Lamb waves and their caustics in composite plates, Ultrasonics. 53 (2013) 283–293.

[70] H.J. Maris, Effect of finite phonon wavelength on phonon focusing, Phys Rev B. 28 (1983) 7033–7037.

[71] V.I. Balakshy, S.N. Mantsevich, Propagation of acoustic beams in a paratellurite crystal, Acoust Phys. 58 (2012) 549–557.

[72] S.N. Mantsevich, Thallium bromide iodide crystal acoustic anisotropy examination, Ultrasonics. 75 (2017) 91–97.

[73] B. Chapuis, N. Terrien, D. Royer, Excitation and focusing of Lamb waves in a multilayered anisotropic plate, J Acoust Soc Am. 127 (2010) 198–203.

[74] C. Potel, S. Baly, J. De Belleval, M. Lowe, P. Gatignol, Deviation of a Monochromatic Lamb Wave Beam in Anisotropic Multilayered Media: Asymptotic Analysis, Numerical and Experimental Results, IEEE Trans Ultrason Ferroelectr Freq Control. 52 (2005) 987–1001.

[75] D. Chronopoulos, Wave steering effects in anisotropic composite structures: Direct calculation of the energy skew angle through a finite element scheme, Ultrasonics. 73 (2017) 43–48.

[76] C. Hakoda, C.J. Lissenden, Application of a general expression for the group velocity vector of elastodynamic guided waves, J Sound Vib. 469 (2020) 115165.

[77] H. Cho, S. Choi, C.J. Lissenden, Effect of skew angle on second harmonic guided wave measurement in composite plates, AIP Conf Proc. 1806 (2017) 060002.

[78] L. Wang, F.G. Yuan, Group velocity and characteristic wave curves of Lamb waves in composites: Modeling and experiments, Compos Sci Technol. 67 (2007) 1370–1384.

[79] A. De Luca, D. Perfetto, A. Polverino, A. Aversano, F. Caputo, Finite Element Modeling Approaches, Experimentally Assessed, for the Simulation of Guided Wave Propagation in Composites, Sustainability . 14 (2022).

[80] J. Zhao, J. Qiu, H. Ji, Reconstruction of the nine stiffness coefficients of composites using a laser generation based imaging method, Compos Sci Technol. 126 (2016) 27–34.

[81] B. Chapuis, N. Terrien, D. Royer, Modeling and experimental investigations of Lamb waves focusing in anisotropic plates, J Phys Conf Ser. 269 (2011) 012020.

[82] K.I. Salas, C.E.S. Cesnik, Guided wave structural health monitoring using CLoVER transducers in composite materials, Smart Mater Struct. 19 (2010) 015014.

[83] C.S. Wang, F. Chang, Diagnosis of impact damage in composite structures with built-in piezoelectrics network, Proc SPIE. 3990 (2000) 13–19.

[84] X. Zhao, H. Gao, G. Zhang, B. Ayhan, F. Yan, C. Kwan, J.L. Rose, Active health monitoring of an aircraft wing with embedded piezoelectric sensor/actuator network: I. Defect detection, localization and growth monitoring, Smart Mater Struct. 16 (2007) 1208–1217.

[85] H. Gao, S. Ali, B. Lopez, Efficient detection of delamination in multilayered structures using ultrasonic guided wave EMATs, NDT and E International. 43 (2010) 316–322.

[86] M. Castaings, B. Hosten, Ultrasonic guided waves for health monitoring of high-pressure composite tanks, NDT and E International. 41 (2008) 648–655.

[87] R. Kažys, A. Demčenko, E. Žukauskas, L. Mažeika, Air-coupled ultrasonic investigation of multi-layered composite materials, Ultrasonics. 44 (2006) 819–822.

[88] Z. Ma, L. Yu, Ultrasonic Lamb wave inspection of composite defects, Proc. SPIE. (2020) 1138103.

[89] H. Mei, V. Giurgiutiu, Predictive 1D and 2D guided-wave propagation in composite plates using the SAFE approach, Proc SPIE 10600 (2018) 10600P

[90] C.A.C. Leckey, K.R. Wheeler, V.N. Hafiychuk, H. Hafiychuk, D.A. Timuçin, Simulation of guided-wave ultrasound propagation in composite laminates: Benchmark comparisons of numerical codes and experiment, Ultrasonics. 84 (2018) 187–200.

[91] T. Hayashi, K. Kawashima, Multiple reflections of Lamb waves at a delamination, Ultrasonics. 40 (2002) 193–197.

[92] S. Shoja, V. Berbyuk, A. Boström, Delamination detection in composite laminates using low frequency guided waves: Numerical simulations, Compos Struct. 203 (2018) 826–834.

[93] W.J. Cantwell, J. Morton, Comparison of the low and high velocity impact response of cfrp, Composites. 20 (1989) 545–551.

[94] Z. Tian, L. Yu, C. Leckey, Delamination detection and quantification on laminated composite structures with Lamb waves and wavenumber analysis, J Intell Mater Syst Struct. 26 (2015) 1723–1738.

[95] B. Murat, P. Khalili, P. Fromme, Scattering of guided waves at delaminations in composite plates, J Acoust Soc Am. 139 (2016) 3044–3052.

[96] R.A. Smith, L.J. Nelson, N. Xie, C. Fraij, S.R. Hallett, Progress in 3D characterisation and modelling of monolithic carbon-fibre composites, Insight, 57 (2015) 131–139.

[97] B. Zhang, X.C. Sun, M.J. Eaton, R. Marks, A. Clarke, C.A. Featherston, L.F. Kawashita, S.R. Hallett, An integrated numerical model for investigating guided waves in impact-damaged composite laminates, Compos Struct. 176 (2017) 945–960.

[98] A. De Luca, F. Caputo, Z. Sharif Khodaei, M.H. Aliabadi, Damage characterization of composite plates under low velocity impact using ultrasonic guided waves, Composites Part B. 138 (2018) 168–180.

[99] P. Kudela, M. Radzienski, W. Ostachowicz, Impact induced damage assessment by means of Lamb wave image processing, Mech Syst Signal Process. 102 (2018) 23–36.

[100] H. Kaczmarek, Lamb Wave Interaction with Impact-induced Damage in Aircraft Composite: Use of the A0 Mode Excited by Air-coupled Transducer, J Compos Mater. 37 (2003) 217–232.

[101] B.I.S. Murat, P. Fromme, Detection of impact damage in composite panels using guided ultrasonic waves, Proceedings of SPIE. 8695 (2013) 869506.

[102] K. Diamanti, J.M. Hodgkinson, C. Soutis, Detection of low-velocity impact damage in composite plates using lamb waves, Struct Health Monit. 3 (2004) 33–41.

[103] N. Toyama, J. Takatsubo, Lamb wave method for quick inspection of impact-induced delamination in composite laminates, Compos Sci Technol. 64 (2004) 1293–1300.

[104] M. Veidt, C.-T. Ng, Influence of stacking sequence on scattering characteristics of the fundamental anti-symmetric Lamb wave at through holes in composite laminates, J Acoust Soc Am. 129 (2011) 1280–1287.

[105] W.K. Chiu, L.R.F. Rose, N. Nadarajah, Scattering of the Fundamental Anti-symmetric Lamb Wave by a Mid-plane Edge Delamination in a Fiber-composite Laminate, Procedia Eng. 188 (2017) 317–324.

[106] B. Feng, A.L. Ribeiro, H.G. Ramos, Using guided ultrasonic wave inspection to quantify the length of delaminations in composite laminates, AIP Conf Proc. 1949 (2018) 230027.

[107] C. Ramadas, K. Balasubramaniam, M. Joshi, C. V. Krishnamurthy, Interaction of guided Lamb waves with an asymmetrically located delamination in a laminated composite plate, Smart Mater Struct. 19 (2010) 065009.

[108] H. Sohn, D. Dutta, J.Y. Yang, H.J. Park, M. DeSimio, S. Olson, E. Swenson, Delamination detection in composites through guided wave field image processing, Compos Sci Technol. 71 (2011) 1250–1256.

[109] N. Toyama, J. Noda, T. Okabe, Quantitative damage detection in cross-ply laminates using Lamb wave method, Compos Sci Technol. 63 (2003) 1473–1479.

[110] N. Testoni, L. De Marchi, A. Marzani, Detection and characterization of delaminations in composite plates via air-coupled probes and warped-domain filtering, Compos Struct. 153 (2016) 773–781.

[111] P. Kudela, T. Wandowski, P. Malinowski, W. Ostachowicz, Application of scanning laser Doppler vibrometry for delamination detection in composite structures, Opt Lasers Eng. 99 (2017) 46–57.

[112] C.A.C. Leckey, J.P. Seebo, Guided wave energy trapping to detect hidden multilayer delamination damage, in: AIP Conf Proc, American Institute of Physics Inc., 2015: pp. 1162–1169.

[113] C.T. Ng, M. Veidt, Scattering analysis of fundamental anti-symmetric lamb wave at delaminations in composite laminates, Journal of the Acoustical Society of America. 129 (2011) 1288–1296.

[114] V. Samaitis, L. Mažeika, R. Rekuviene, Assessment of the length and depth of delamination-type defects using ultrasonic guided waves, Applied Sciences (Switzerland). 10 (2020) 5236-.

[115] N.A. Ibrahim, M.A. Kamarudin, M.H.F.M. Jurimi, B.I.S. Murat, Parametric study of guided ultrasonic wave propagation in carbon-fiber composite plates, in: IOP Conf Ser Mater Sci Eng, Institute of Physics Publishing, 2018.

[116] S. Gupta, P. Rajagopal, Effect of ply orientation and through-thickness position of delamination on the reflection of fundamental symmetric S0 Lamb mode in GFRP composite plate structures, Ultrasonics. 90 (2018) 109–119.

[117] H. Mei, V. Giurgiutiu, Characterization of multilayer delaminations in composites using wavenumber analysis: numerical and experimental studies, Struct Health Monit. (2020).

[118] A. Migot, H. Mei, V. Giurgiutiu, Numerical and experimental investigation of delaminations in a unidirectional composite plate using NDT and SHM techniques, J Intell Mater Syst Struct. (2020).

[119] R.S. Panda, P. Rajagopal, K. Balasubramaniam, Characterization of delamination-type damages in composite laminates using guided wave visualization and air-coupled ultrasound, Struct Health Monit. 16 (2017) 142–152.

[120] G.T. Pudipeddi, C. Ng, A. Kotousov, Mode Conversion and Scattering of Lamb Waves at Delaminations in Composite Laminates, J Aero Engi. 32 (2019) 04019067-

[121] V. Serey, N. Quaegebeur, M. Renier, P. Micheau, P. Masson, M. Castaings, Selective generation of ultrasonic guided waves for damage detection in rectangular bars, Struct Health Monit. 20 (2021) 1156–1168.

[122] W.B. Williams, T.E. Michaels, J.E. Michaels, Estimation and application of 2-D scattering matrices for sparse array imaging of simulated damage in composite panels, AIP Conf Proc. 1806 (2017) 020014.

[123] A. Ebrahimkhanlou, B. Dubuc, S. Salamone, Damage localization in metallic plate structures using edge-reflected lamb waves, Smart Mater Struct. 25 (2016) 085035.

[124] Q. Bao, S. Yuan, Y. Wang, L. Qiu, Anisotropy compensated MUSIC algorithm based composite structure damage imaging method, Compos Struct. 214 (2019) 293–303.

[125] T. Clarke, P. Cawley, P.D. Wilcox, A.J. Croxford, Evaluation of the damage detection capability of a sparse-array guided-wave SHM system applied to a complex structure under varying thermal conditions, IEEE Trans Ultrason Ferroelectr Freq Control. 56 (2009) 2666–2678.

[126] C.H. Wang, J.T. Rose, F.K. Chang, A synthetic time-reversal imaging method for structural health monitoring, Smart Mater Struct. 13 (2004) 415–423.

[127] J.S. Hall, J.E. Michaels, Multipath ultrasonic guided wave imaging in complex structures, Struct Health Monit. 14 (2015) 345–358.

[128] J.S. Hall, P. McKeon, L. Satyanarayan, J.E. Michaels, N.F. Declercq, Y.H. Berthelot, Minimum variance guided wave imaging in a quasi-isotropic composite plate, Smart Mater Struct. 20 (2011) 020513.

[129] J. Zhang, P. Yu, T. Gang, Measurement of the ultrasonic scattering matrices of near-surface defects using ultrasonic arrays, Nondestr Test and Eval. 31 (2016) 303–318.

[130] P.C. Ostiguy, N. Quaegebeur, P. Masson, Comparison of model-based damage imaging techniques for transversely isotropic composites, Struct Health Monit. 16 (2017) 428–443.

[131] W.B. Williams, T.E. Michaels, J.E. Michaels, Application of wavefield imaging to characterize scattering from artificial and impact damage in composite laminate panels, AIP Conf Proc. 1949 (2018).

[132] J. Fong, M.J.S Lowe, Curvature Effect on the Properties of Guided Waves in Plates, AIP Conf Proc, 700 (2004) 126–133.

[133] F. Yan, J. Mu, J.L. Rose, Guided wave propagation in curved plate-like structures, in: AIP Conf Proc, 2008: pp. 92–98.

[134] A. Demma, P. Cawley, M. Lowe, B. Pavlakovic, The effect of bends on the propagation of guided waves in pipes, in: Journal of Pressure Vessel Technology, Transactions of the ASME, 2005: pp. 328–335.

[135] S. Heinlein, P. Cawley, T.K. Vogt, Reflection of torsional T(0,1) guided waves from defects in pipe bends, NDT and E International. 93 (2018) 57–63.

[136] I.F. Saxena, N. Guzman, L.U. Kempen, V. Dayal, Viability of guided-wave ultrasound diagnostics for sharply curved composite structures, Proc SPIE, 8026 (2011) 802603.

[137] C. Hakoda, G. Choi, C. Lissenden, Modeling guided wave propagation in curved thick composites with ply drops and marcelling, in: AIP Conf Proc, American Institute of Physics Inc., 2018.

[138] P. Huthwaite, Evaluation of inversion approaches for guided wave thickness mapping, Proc R Soc A: 470 (2014) 20140063.

[139] Nurmalia, N. Nakamura, H. Ogi, M. Hirao, K. Nakahata, Mode conversion behavior of SH guided wave in a tapered plate, NDT and E International. 45 (2012) 156–161.

[140] S. Sikdar, P. Fiborek, P. Malinowski, W. Ostachowicz, Ultrasonic guided wave propagation in a repaired stiffened composite panel, Proc SPIE, 10972 (2019) 1097201

[141] W. Hufenbach, A. Hornig, B. Zhou, A. Langkamp, M. Gude, Determination of strain rate dependent through-thickness tensile properties of textile reinforced thermoplastic composites using L-shaped beam specimens, Compos Sci Technol. 71 (2011) 1110–1116.

[142] K. Balasubramaniam, S. Sikdar, T. Wandowski, P.H. Malinowski, Ultrasonic guided wave-based debond identification in a GFRP plate with L-stiffener, Smart Mater Struct. 31 (2022) 015023.

[143] C. Ramadas, J. Padiyar, K. Balasubramaniam, M. Joshi, C. V. Krishnamurthy, Lamb wave based ultrasonic imaging of interface delamination in a composite T-joint, NDT and E International. 44 (2011) 523–530.

[144] G.K. Geetha, D. Roy Mahapatra, S. Gopalakrishnan, S. Hanagud, Laser Doppler imaging of delamination in a composite T-joint with remotely located ultrasonic actuators, Compos Struct. 147 (2016) 197–210.

[145] M. Philibert, C. Soutis, M. Gresil, K. Yao, Damage detection in a composite t-joint using guided lamb waves, Aerospace. 5 (2018) 5020040.

[146] H.Y. Chang, F.G. Yuan, Damage imaging in a stiffened curved composite sandwich panel with wavenumber index via Riesz transform, Struct Health Monit. 19 (2020) 902–916.

[147] J. Spytek, J. Mrowka, L. Pieczonka, L. Ambrozinski, Multi-resolution non-contact damage detection in complex-shaped composite laminates using ultrasound, NDT and E International. 116 (2020) 102366.

[148] X. Yu, M. Ratassepp, Z. Fan, Damage detection in quasi-isotropic composite bends using ultrasonic feature guided waves, Compos Sci Technol. 141 (2017) 120–129.

[149] P. Manogharan, P. Rajagopal, K. Balasubramaniam, Longitudinal guided waves confined in radius filler regions of composite joints, J Acoust Soc Am. 140 (2016) 334–343.

[150] L. Maio, F. Ricci, V. Memmolo, E. Monaco, N.D. Boffa, Application of laser Doppler vibrometry for ultrasonic velocity assessment in a composite panel with defect, Compos Struct. 184 (2018) 1030–1039.

[151] L. Maio, V. Memmolo, S. Boccardi, C. Meola, F. Ricci, N.D. Boffa, E. Monaco, Ultrasonic and IR Thermographic Detection of a Defect in a Multilayered Composite Plate, in: Procedia Eng, Elsevier Ltd, 2016: pp. 71–79.

[152] N. Netshidavhini, R.B. Mabuza, Effects of various couplants on carbon steel and aluminium materials using ultrasonic testing. Proc 18th WCNDT (2012)

[153] L. Maio, P. Fromme, On ultrasound propagation in composite laminates: advances in numerical simulation, Progress in Aerospace Sciences. 129 (2022) 100791.

[154] Dassault Systèmes Simulia, ABAQUS documentation, Abaqus 6.12. (2013).

[155] R. Watson, Modelling of Guided Ultrasonic Wave Scattering at Defects, MSc Thesis, University College London, 2007.

[156] B.I.S. Murat, Propagation and Scattering of Guided Waves in Composite Plates with Defects, PhD Thesis, University College London, 2015.

[157] Z. Celep, Z.P. Bazant, Spurious reflection of elastic waves due to gradually changing finite element size. J. Numer Methods Eng 19 (1983) 631-646

[158] P. Rajagopal, M. Drozdz, M.J.S. Lowe, Towards improved finite element modelling of the interaction of elastic waves with complex defect geometries, AIP Conf Proc, 1096 (2009) 49–56.

[159] F. Ihlenburg, Finite Element Analysis of Acoustic Scattering, Springer, New York, 1998.

[160] R. Mullen, T. Belytschko, Dispersion analysis of finite element semidiscretizations of the two-dimensional wave equation, Int J Numer Methods Eng. 18 (1982) 11–29.

[161] A.F. Bower, Applied Mechanics of Solids, CRC Press, 2009.

[162] A. Köllner, Predicting buckling-driven delamination propagation in composite laminates: An analytical modelling approach, Compos Struct. 266 (2021) 113776.

[163] B. Hosten, M. Deschamps, B.R. Tittmann, Inhomogeneous wave generation and propagation in lossy anisotropic solids. Application to the characterization of viscoelastic composite materials, Journal of the Acoustical Society of America. 82 (1987) 1763–1770.

[164] M. Gresil, V. Giurgiutiu, Prediction of attenuated guided waves propagation in carbon fiber composites using Rayleigh damping model, J Intell Mater Syst Struct. 26 (2015) 2151–2169.

[165] M. Staudenmann, Structural Waves in Nondestructive Testing, PhD Thesis, Swiss Federal Institute of Technology, 1995.

[166] F. Hervin, P. Fromme, Guided wave skew velocity correction in anisotropic laminates, Available Online Ultrasonics. (2023).

[167] M. Born, E. Wolf, Principles of Optics, Cambridge University Press, 1999.

[168] F. Hervin, P. Fromme, Anisotropy influence on guided wave propagation and steering in unidirectional CFRP, Proc ASME (2023).

[169] F. Hervin, L. Maio, P. Fromme, Guided wave scattering at a delamination in a quasi-isotropic composite laminate: Experiment and simulation, Compos Struct. 275 (2021) 114406.

[170] P. Fromme, Guided wave sensitivity prediction for part and through-thickness crack-like defects, Struct Health Monit. 19 (2020) 953–963.

[171] J. Zhang, B.W. Drinkwater, P.D. Wilcox, The use of ultrasonic arrays to characterize crack-like defects, J Nondestr Eval. 29 (2010) 222–232.

[172] L.W. Schmerr, Fundamentals of Ultrasonic Nondestructive Evaluation, Springer International Publishing, Cham, 2016.

[173] A. Srivastava, F. Lanza di Scalea, On the existence of antisymmetric Lamb waves at nonlinear higher harmonics, Ultrasonics, 323 (2009) 932-943.

UCL Research Paper Declaration Forms

1. For a research manuscript that has already been published (if not yet published, please skip to section 2)**:**		
a) Where was the work published? (e.g. journal name)	Composite Structures	
b) Who published the work? (e.g. Elsevier/Oxford University Press):	Elsevier	
c) When was the work published?	01/11/2021	
d) Was the work subject to academic peer review?	Yes	
e) Have you retained the copyright for the work?	Yes	
2. For a research manuscript prepared for publication but that has not yet been published (if already published, please skip to section 3)**:**		
a) Has the manuscript been uploaded to a preprint server? (e.g. medRxiv):		**If yes, which server?**
b) Where is the work intended to be published?		
c) List the manuscript's authors in the intended authorship order:		
d) Stage of publication		
3. For multi-authored work, please give a statement of contribution covering all authors (if single-author, please skip to section 4**):**		
Flora Hervin: Methodology, Formal analysis, Validation, Investigation, Data curation, Writing - original draft, Visualization. . **Leandro Maio:** Resources, Writing - review & editing. **Paul Fromme:** Conceptualization, Methodology, Validation, Resources, Writing - review & editing, Supervision		
4. In which chapter(s) of your thesis can this material be found?		
2, 3, 4, 6		
5. e-Signatures confirming that the information above is accurate (this form should be co-signed by the supervisor/ senior author unless this is not appropriate, e.g. if the paper was a single-author work):		
Candidate:	Flora Hervin	**Date:** 23/12/2022
Supervisor/ Senior Author	Paul Fromme	**Date:** 03/01/2023

1. For a research manuscript that has already been published (if not yet published, please skip to section 2)**:**			
a) Where was the work published? (e.g. journal name)	Structural Health Monitoring		
b) Who published the work? (e.g. Elsevier/Oxford University Press):	SAGE		
c) When was the work published?	11/11/2022 (Available online)		
d) Was the work subject to academic peer review?	Yes		
e) Have you retained the copyright for the work?	Yes		
2. For a research manuscript prepared for publication but that has not yet been published (if already published, please skip to section 3)**:**			
a) Has the manuscript been uploaded to a preprint server? (e.g. medRxiv):		**If yes, which server?**	
b) Where is the work intended to be published? (e.g. names of journals that you are planning to submit to)			
c) List the manuscript's authors in the intended authorship order:			
d) Stage of publication			
3. For multi-authored work, please give a statement of contribution covering all authors (if single-author, please skip to section 4**):**			
Flora Hervin: Conceptualization, Methodology, Formal analysis, Validation, Investigation, Data curation, Writing - original draft, Writing - review & editing, Visualization. **Paul Fromme:** Conceptualization, Methodology, Validation, Resources, Writing - review & editing, Supervision.			
4. In which chapter(s) of your thesis can this material be found?			
2, 3, 4, 6			
5. e-Signatures confirming that the information above is accurate (this form should be co-signed by the supervisor/ senior author unless this is not appropriate, e.g. if the paper was a single-author work):			
Candidate:	Flora Hervin	**Date:**	23/12/2022
Supervisor/ Senior Author	Paul Fromme	**Date:**	03/01/2023

2. **For a research manuscript prepared for publication but that has not yet been published** (if already published, please skip to section 3)**:**			
a) **Has the manuscript been uploaded to a preprint server?** (e.g. medRxiv):	No	**If yes, which server?**	
b) **Where is the work intended to be published?** (e.g. names of journals that you are planning to submit to)	The Journal of the Acoustical Society of America		
c) **List the manuscript's authors in the intended authorship order:**	Flora Hervin, Paul Fromme.		
d) **Stage of publication**	In Press		
3. **For multi-authored work, please give a statement of contribution covering all authors** (if single-author, please skip to section 4**):**			
Flora Hervin: Conceptualization, Methodology, Formal analysis, Validation, Investigation, Data curation, Writing - original draft, Writing - review & editing, Visualization. **Paul Fromme:** Conceptualization, Methodology, Validation, Resources, Writing - review & editing, Supervision.			
4. **In which chapter(s) of your thesis can this material be found?**			
2, 3, 4, 5			
5. **e-Signatures confirming that the information above is accurate** (this form should be co-signed by the supervisor/ senior author unless this is not appropriate, e.g. if the paper was a single-author work):			
Candidate:	Flora Hervin	**Date:**	23/12/2022
Supervisor/ Senior Author	Paul Fromme	**Date:**	03/01/2023

2. **For a research manuscript prepared for publication but that has not yet been published** (if already published, please skip to section 3)**:**			
a) **Has the manuscript been uploaded to a preprint server?** (e.g. medRxiv):	No	**If yes, which server?**	
b) **Where is the work intended to be published?** (e.g. names of journals that you are planning to submit to)	Ultrasonics		
c) **List the manuscript's authors in the intended authorship order:**	Flora Hervin, Paul Fromme		
d) **Stage of publication**	In Press		
3. **For multi-authored work, please give a statement of contribution covering all authors** (if single-author, please skip to section 4**):**			
Flora Hervin: Conceptualization, Methodology, Formal analysis, Validation, Investigation, Data curation, Writing - original draft, Writing - review & editing, Visualization. **Paul Fromme:** Conceptualization, Methodology, Validation, Resources, Writing - review & editing, Supervision.			
4. **In which chapter(s) of your thesis can this material be found?**			
5			
5. **e-Signatures confirming that the information above is accurate** (this form should be co-signed by the supervisor/ senior author unless this is not appropriate, e.g. if the paper was a single-author work):			
Candidate:	Flora Hervin	**Date:**	23/12/2022
Supervisor/ Senior Author	Flora Hervin	**Date:**	03/01/2023

1. For a research manuscript that has already been published (if not yet published, please skip to section 2)**:**			
a) Where was the work published? (e.g. journal name)	Proceedings of SPIE		
b) Who published the work? (e.g. Elsevier/Oxford University Press):	SPIE		
c) When was the work published?	23/04/2020		
d) Was the work subject to academic peer review?	No		
e) Have you retained the copyright for the work?	Yes		
2. For a research manuscript prepared for publication but that has not yet been published (if already published, please skip to section 3)**:**			
a) Has the manuscript been uploaded to a preprint server? (e.g. medRxiv):		**If yes, which server?**	
b) Where is the work intended to be published?			
c) List the manuscript's authors in the intended authorship order:			
d) Stage of publication			
3. For multi-authored work, please give a statement of contribution covering all authors (if single-author, please skip to section 4**):**			
Leandro Maio: Conceptualization, Resources, Writing – original draft. **Flora Hervin:** Formal analysis, Validation, Investigation, Data curation, Writing - original draft, Visualization. **Paul Fromme:** Conceptualization, Methodology, Validation, Resources, Writing - review & editing, Supervision.			
4. In which chapter(s) of your thesis can this material be found?			
6			
5. e-Signatures confirming that the information above is accurate (this form should be co-signed by the supervisor/ senior author unless this is not appropriate, e.g. if the paper was a single-author work):			
Candidate:	Flora Hervin	**Date:**	23/12/2022
Supervisor/ Senior Author	Paul Fromme	**Date:**	03/01/2023

1. For a research manuscript that has already been published (if not yet published, please skip to section 2)**:**			
a) Where was the work published? (e.g. journal name)	Proceedings of SPIE		
b) Who published the work? (e.g. Elsevier/Oxford University Press):	SPIE		
c) When was the work published?	22/03/2021		
d) Was the work subject to academic peer review?	No		
e) Have you retained the copyright for the work?	Yes		
2. For a research manuscript prepared for publication but that has not yet been published (if already published, please skip to section 3)**:**			
a) Has the manuscript been uploaded to a preprint server? (e.g. medRxiv):		**If yes, which server?**	
b) Where is the work intended to be published?			
c) List the manuscript's authors in the intended authorship order:			
d) Stage of publication			
3. For multi-authored work, please give a statement of contribution covering all authors (if single-author, please skip to section 4**):**			
Flora Hervin: Methodology, Formal analysis, Validation, Investigation, Data curation, Writing - original draft, Writing - review & editing, Visualization. **Paul Fromme:** Conceptualization, Methodology, Validation, Resources, Writing - review & editing, Supervision.			
4. In which chapter(s) of your thesis can this material be found?			
6			
5. e-Signatures confirming that the information above is accurate (this form should be co-signed by the supervisor/ senior author unless this is not appropriate, e.g. if the paper was a single-author work):			
Candidate:	Flora Hervin	**Date:**	23/12/2022
Supervisor/ Senior Author	Paul Fromme	**Date:**	03/01/2023

1. For a research manuscript that has already been published (if not yet published, please skip to section 2)**:**			
a) Where was the work published? (e.g. journal name)	Proceedings of SPIE		
b) Who published the work? (e.g. Elsevier/Oxford University Press):	SPIE		
c) When was the work published?	19/04/2022		
d) Was the work subject to academic peer review?	No		
e) Have you retained the copyright for the work?	Yes		
2. For a research manuscript prepared for publication but that has not yet been published (if already published, please skip to section 3)**:**			
a) Has the manuscript been uploaded to a preprint server? (e.g. medRxiv):		**If yes, which server?**	
b) Where is the work intended to be published?			
c) List the manuscript's authors in the intended authorship order:			
d) Stage of publication			
3. For multi-authored work, please give a statement of contribution covering all authors (if single-author, please skip to section 4**):**			
Flora Hervin: Conceptualization, Methodology, Formal analysis, Validation, Investigation, Data curation, Writing - original draft, Writing - review & editing, Visualization. **Paul Fromme:** Conceptualization, Methodology, Validation, Resources, Writing - review & editing, Supervision.			
4. In which chapter(s) of your thesis can this material be found?			
6			
5. e-Signatures confirming that the information above is accurate (this form should be co-signed by the supervisor/ senior author unless this is not appropriate, e.g. if the paper was a single-author work):			
Candidate:	Flora Hervin	**Date:**	23/12/2022
Supervisor/ Senior Author:	Paul Fromme	**Date:**	03/01/2023

1. For a research manuscript that has already been published (if not yet published, please skip to section 2)**:**			
a) Where was the work published? (e.g. journal name)	ASME Conference Proceedings		
b) Who published the work? (e.g. Elsevier/Oxford University Press):	ASME		
c) When was the work published?	28/07/2021		
d) Was the work subject to academic peer review?	No		
e) Have you retained the copyright for the work?	No		
[If no, please seek permission from the relevant publisher and check the box next to the below statement]: ☒ *I acknowledge permission of the publisher named under 1b to include in this thesis portions of the publication named as included in 1a.*			
2. For a research manuscript prepared for publication but that has not yet been published (if already published, please skip to section 3)**:**			
a) Has the manuscript been uploaded to a preprint server? (e.g. medRxiv):		**If yes, which server?**	
b) Where is the work intended to be published?			
c) List the manuscript's authors in the intended authorship order:			
d) Stage of publication			
3. For multi-authored work, please give a statement of contribution covering all authors (if single-author, please skip to section 4**):**			
Flora Hervin: Conceptualization, Methodology, Formal analysis, Validation, Investigation, Data curation, Writing - original draft, Writing - review & editing, Visualization. **Paul Fromme:** Conceptualization, Methodology, Validation, Resources, Writing - review & editing, Supervision.			
4. In which chapter(s) of your thesis can this material be found?			
6			
5. e-Signatures confirming that the information above is accurate (this form should be co-signed by the supervisor/ senior author unless this is not appropriate, e.g. if the paper was a single-author work):			
Candidate:	Flora Hervin	**Date:**	23/12/2022
Supervisor/ Senior Author	Paul Fromme	**Date:**	03/01/2023

2. **For a research manuscript prepared for publication but that has not yet been published** (if already published, please skip to section 3)**:**			
a) **Has the manuscript been uploaded to a preprint server?** (e.g. medRxiv):		No	**If yes, which server?**
b) **Where is the work intended to be published?** (e.g. names of journals that you are planning to submit to)		Proceedings of ASME	
c) **List the manuscript's authors in the intended authorship order:**		Flora Hervin, Paul Fromme	
d) **Stage of publication**		In press	
3. **For multi-authored work, please give a statement of contribution covering all authors** (if single-author, please skip to section 4**):**			
Flora Hervin: Conceptualization, Methodology, Formal analysis, Validation, Investigation, Data curation, Writing - original draft, Writing - review & editing, Visualization. **Paul Fromme:** Conceptualization, Methodology, Validation, Resources, Writing - review & editing, Supervision.			
4. **In which chapter(s) of your thesis can this material be found?**			
6			
5. **e-Signatures confirming that the information above is accurate** (this form should be co-signed by the supervisor/ senior author unless this is not appropriate, e.g. if the paper was a single-author work):			
Candidate:	Flora Hervin	**Date:**	23/12/2022
Supervisor/ Senior Author (where appropriate)**:**	Paul Fromme	**Date:**	03/01/2023

2. **For a research manuscript prepared for publication but that has not yet been published** (if already published, please skip to section 3)**:**			
a) **Has the manuscript been uploaded to a preprint server?** (e.g. medRxiv):	NoNo	**If yes, which server?**	
b) **Where is the work intended to be published?** (e.g. names of journals that you are planning to submit to)	Proceedings of ASME		
c) **List the manuscript's authors in the intended authorship order:**	Flora Hervin, Paul Fromme		
d) **Stage of publication**	In press		
3. **For multi-authored work, please give a statement of contribution covering all authors** (if single-author, please skip to section 4**):**			
Flora Hervin: Conceptualization, Methodology, Formal analysis, Validation, Investigation, Data curation, Writing - original draft, Writing - review & editing, Visualization. **Paul Fromme:** Conceptualization, Methodology, Validation, Resources, Writing - review & editing, Supervision.			
4. **In which chapter(s) of your thesis can this material be found?**			
5			
5. **e-Signatures confirming that the information above is accurate** (this form should be co-signed by the supervisor/ senior author unless this is not appropriate, e.g. if the paper was a single-author work):			
Candidate:	Flora Hervin	**Date:**	23/12/2022
Supervisor/ Senior Author:	Paul Fromme	**Date:**	03/01/2023